UNIVERSIDAD NACIONAL AUTÓNOMA DE MÉXICO

Programa de Posgrado en Astrofísica

Instituto de Radioastronomía y Astrofísica

Propiedades físicas de núcleos densos inmersos en nubes moleculares filamentarias. Simulaciones y comparación con observaciones.

TESIS
QUE PARA OPTAR POR EL GRADO DE
DOCTOR EN CIENCIAS
(ASTROFÍSICA)

PRESENTA
VIANEY EDALY CAMACHO PEREZ

Tutor
Dr. Enrique Cristian Vázquez Semadeni
Instituto de Radioastronomía y Astrofísica

MÉXICO, CD.MX. OCTUBRE 2019

Resumen

Los diversos escenarios propuestos en el campo de formación estelar difieren de acuerdo a la importancia relativa de los efectos de la turbulencia, la gravedad, los campos magnéticos y la retroalimentación estelar, en el proceso de formación de estrellas. Una idea común entre estas teorías, hasta hace algunos años, ha sido que las nubes moleculares y su subestructura son estacionarias y están en un estado de equilibrio. Sin embargo, las nubes moleculares en el medio interestelar evolucionan con el tiempo. El objetivo principal de esta tesis es comprender esta evolución por medio del estudio de las propiedades físicas de la subestructura en nubes moleculares simuladas y reales.

En esta tesis, adoptamos el escenario de colapso jerárquico global. Analizamos simulaciones numéricas que representan la formación y evolución de las nubes moleculares en contracción gravitacional y estudiamos nubes moleculares reales en diferentes etapas evolutivas. Calculamos, para las nubes y su subestructura, su masa, tamaño y dispersión de velocidades, así como la actividad de formación estelar en el caso de las simulaciones. A partir de estas propiedades, derivamos las relaciones de escala que caracterizan el equilibrio entre las energías gravitacional y cinética. En la primera parte de la tesis mostramos que las nubes, los grumos y los núcleos densos, siguen la relación $\sigma_v/R^{1/2} \propto \Sigma^{1/2}$, característica de equiparación entre energías gravitacional y cinética, exhibiendo desviaciones sistemáticas que difieren para las distintas clases de objetos. Mostramos que el exceso de energía cinética puede ser explicado, para nubes de baja densidad columnar, como movimientos compresivos a gran escala que ensamblan las nubes o bien, a la dispersión de estas nubes, mientras que, para el caso de densidades columnares más altas, observamos núcleos densos que exhiben formación estelar. En este caso, mostramos que el exceso de energía cinética se debe a la masa estelar que no se tiene en cuenta en el potencial gravitacional del núcleo. En ningún caso existe la necesidad de confinamiento por presión externa.

En la segunda parte, investigamos la evolución del balance energético y la actividad de formación estelar, en los diagramas de $\sigma_v/R^{1/2}$ vs. $\Sigma^{1/2}$ y parámetro virial vs. masa, de una nube y su subestructura. Mostramos que la nube seleccionada evoluciona a partir de una etapa de baja masa, baja densidad y baja tasa de formación estelar (SFR) similar, por ejemplo, a la nube de la Pipa, a una etapa de masa intermedia, alta densidad y más alta SFR similar, por ejemplo, a la nube infrarroja oscura G14.225, en pocos mega años. La trayectoria evolutiva del balance de energía de las subestructuras de la nube simulada pasa por los lugares geométricos de las subestructuras, lo que sugiere que una nube de baja masa y baja SFR, como la Pipa, evolucionará hacia una etapa más masiva, más densa y con mayor SFR en pocos mega años. Este escenario evolutivo concuerda con el escenario de colapso global para nubes moleculares formadoras de estrellas.

Abstract

Star formation theories have been evolving since the last century. The various scenarios proposed in this field differ according to the relative importance to the effects that turbulence, gravity, magnetic fields and stellar feedback have in the process of star formation. Nevertheless, a common idea between these theories, until recent years, has been that molecular clouds and their substructure are stationary and in a state of equilibrium. However, there is increasing evidence that molecular clouds in the interstellar medium evolve in time. The main goal of this thesis is to understand this evolution through the study of the physical properties of the substructure in simulated and real molecular clouds.

The main hypothesis adopted in this thesis is the scenario of global hierarchical collapse, which has been suggested in recent numerical and observational works as the likely state of molecular clouds. We analyze numerical simulations representing the formation and evolution of molecular clouds, in which the main driving mechanism is the gravitational contraction, and the various clouds are in different evolutionary stages. The mass, size, velocity dispersion, and star formation activity are measured in the simulations for clouds and their substructure in our samples. In the first part of this thesis, we derive the scaling relations that characterize the balance between the gravitational and kinetic energies, derived from the mentioned properties. From these, we show that clouds, clumps and cores tend to follow the relation $\sigma_v/R^{1/2} \propto \Sigma^{1/2}$, but exhibit various kinds of deviations from this relation that are systematic and different for different classes of objects, such as diffuse clouds, filaments, and dense cores. We suggest that low-column density clouds tend to exhibit an excess of kinetic energy because they are dominated by motions induced by agents different from their self-gravity, but that in roughly half of the cases, these motions may be large-scale compressions that assemble the clouds and lead them to the onset of self-gravitation. The other half is in the process of dispersal. On the other hand, some of the more evolved high-column density cores that present star formation, also show a slight excess of kinetic energy, which we show is originated by the stellar mass that is not taken into account in the gravitational potential of the whole core. In no case is there a need for an external confining pressure.

In the second part of this thesis, we investigate the evolution of the energy balance and star formation activity of a clump, showing that it evolves from a low-mass, low-density, low-star formation rate (SFR) stage similar, for example to the substructure in the Pipe cloud, to an intermediate-mass, high-density, higher-SFR stage similar, for example, to the substructure in the G14.225 infrared dark cloud, over the course of a few megayears. We also show that the substructure in this region evolve in the $\sigma_v/R^{1/2}$ vs. $\Sigma^{1/2}$ and virial parameter vs. mass diagrams, indicative of their energy balance. Comparison with the observational data from these two clouds shows very good agreement with the respective evolutionary stage of the numerical clump, suggesting that a low-mass, low-SFR cloud such as the Pipe will evolve into a more massive, higher-density and higher-SFR in a few megayears, and supporting the collapsing, evolutionary scenario for star-forming molecular clouds.

Contents

Introduction

Star formation is one of the fundamental problems in astrophysics. In order to understand how stars are born, it is necessary to study the regions where they are formed, not only because these regions provide the raw material for their formation, but also because they constitute the initial conditions for the structure and kinematics of stellar clusters and associations, and therefore play a crucial role in the evolution of galaxies. These regions are the so-called molecular clouds.

Molecular clouds are cold dense entities that consist principally of molecular hydrogen (H_2), with the presence of dust very well mixed with the gas. These regions seem to be organized in a variety of structures, embedded one into each other, from large-scale filaments to small and dense cores. They are observed to span a wide range of density, temperature, velocity dispersion and size. Multiple models and theories have been developed in order to explain the observations. Currently, the most accepted paradigm is the so called *gravo-turbulent* scenario (e.g. Mac Low & Klessen, 2004), although in recent years it has been challenged by the alternative *global hierarchical collapse* one (e.g. Hartmann et al., 2001; Vázquez-Semadeni et al., 2009; Vázquez-Semadeni et al., 2019).

In the gravo-turbulent scenario, molecular clouds evolve close to equilibrium, and the turbulence plays a crucial role in both inducing density enhancements at small scales, and supporting the clouds in order to prevent star formation at large scales. Although this scenario roughly explains the processes that determine the star formation (in terms of a quasi-static evolution), some questions remain unanswered. For example, what is the source that maintains the turbulence. In the last years, observational and numerical evidence have arisen suggesting that molecular clouds may be undergoing global gravitational contraction motions (Peretto et al., 2007; Vázquez-Semadeni et al., 2007; Galván-Madrid et al., 2009; Peretto et al., 2013; Carroll-Nellenback et al., 2014; Liu et al., 2015; Hacar et al., 2017; Jackson et al., 2019; Barnes et al., 2019). In this global gravitational collapse scenario, the clouds undergo a secular evolution in all its physical properties, including, for example, the star formation rate (SFR).

In this thesis we present results about the structure and evolution of clouds dominated in different degrees by gravitational contraction. We study numerical simulations of the formation and evolution of molecular clouds, where the motions are due to the initial decaying turbulence and subsequently to gravitational contraction. We investigate the substructure and the properties of the clouds formed in the simulations. We focus on the energy balance between gravitational and kinetic energies in order to determine whether the motions in the structures are dominated by gravitational infall or random turbulence. Also, we analyze the temporal evolution of a star forming region in one of the simulations, focusing on the star formation rate and the virial parameter of the region and its hierarchical structure, and we compare our results to those in a pair of real molecular clouds, likely to be at different evolutionary stages. For the latter task, we have made use of existing data in the literature.

Our study shows that molecular clouds, clumps, and cores, in both the numerical and observational samples, follow the *generalized Larson scaling relation*, $\sigma_v/R^{1/2} \propto \Sigma^{1/2}$, where σ_v is the velocity dispersion, R is the size of the cloud and Σ is the column density (Heyer et al., 2009; Ballesteros-Paredes et al., 2011), although we also find that the clouds and their substructure show deviations from this relation during their evolution. We show that these deviations reflect the initial compressive motions likely to be generated by large-scale collapse or large-scale turbulence in the diffuse medium, or else true disrupting motions.

We propose that different kinds of deviations are characteristic of different clump evolutionary states, and that this evolution determines also the star formation activity of the clumps, which is consistent with the analyzed observational data. These results are consistent with the recently proposed scenario of hierarchical gravitational collapse.

In Chapter 1 we introduce the main properties and physical processes of the interstellar medium, which are important to understand the composition and evolution of molecular clouds. Molecular clouds and their main physical properties are described in Chapter 2. Some of the numerical models that have been developed in the star formation field are shown in Chapter 3, as well as the numerical simulations used in this thesis. In Chapter 4 we discuss the molecular clouds properties derived from observations. The analysis of the cloud energy budget in numerical simulations is presented in Chapter 5; these results have been published in Camacho et al. (2016). Chapter 6 shows the study of the temporal evolution of a star forming region and the comparison with observational data (Camacho et al. in prep.). Finally, in Chapter 7 the conclusions are presented.

Chapter 1

The Interstellar Medium

The structure of a galaxy has a number of components that characterize its morphology and evolution. One of the most important is the responsible for the star formation, the interstellar medium (ISM). In a simple way, it can be described as the environment between the stars, a tenuous medium mostly containing a combination of gas, dust, cosmic rays, magnetic fields, and the radiation field spread throughout the medium, where all the other components are immersed. In our Galaxy, the detection of components of the ISM was made gradually over more than fifty years (∼1904-1965, see review by Ferrière, 2001) by indirect methods as absorption lines, stellar reddening, and polarization effects. Since then, a variety of studies have provided vast information about the constituents of the ISM, how they are distributed at different densities and temperatures, and how they connect to each other. Understanding the components and the physical processes that rule the ISM is crucial in our understanding of the star formation process given that the ISM constitutes the reservoir from which stars are born.

In the next sections we present a brief description of the main elements of the ISM and the phases that exhibits at different conditions, the physical processes that contribute to maintain its structure and the equations that describe the interaction between the components and the physical processes.

1.1 Analytical description of the ISM

The ISM is compressible, its temperature differs from a region to another, causing the sound speed to vary from super- to sub-sonic regimes. Additionally, it is subject to a number of physical processes that makes it complex and dynamical. In order to identify its components, the sources, the forces and how they interact with each other to maintain the observed structure and dynamics, the ISM can be described

by the fluid equations.

Consider the mass-weighted Euler equations for a compressible self-gravitating, magnetized gas in absence of diffusive effects.

Mass conservation or *continuity equation*,

$$\frac{\partial \rho}{\partial t} + \mathbf{u} \cdot \nabla \rho = -\rho \nabla \cdot \mathbf{u}, \tag{1.1}$$

where $\rho = \mu\, m_{\rm H} n$ is the mass density, μ is the molecular weight, $m_{\rm H}$ is the proton mass, n is the number density, and $\mathbf{u}$ is the velocity vector.

Equation of *conservation of momentum*,

$$\frac{\partial \mathbf{u}}{\partial t} + \mathbf{u} \cdot \nabla \mathbf{u} = -\frac{\nabla P}{\rho} - \nabla \phi + \frac{1}{4\pi\rho}(\nabla \times \mathbf{B}) \times \mathbf{B}, \tag{1.2}$$

where P is the thermal pressure, $-\nabla\phi$ is the gravitational potential, and $\mathbf{B}$ is the magnetic field. In this work we do not consider the magnetic field. However, as a component of the ISM it is briefly described in Sec. 1.2.1. In general, the ISM is assumed to behave as an ideal gas, thus, $P = nk_BT$, where k_B is the Boltzmann constant.

Equation of *energy conservation*,

$$\frac{\partial e}{\partial t} + \mathbf{u} \cdot \nabla e = -(\gamma - 1) e \nabla \cdot \mathbf{u} + \Gamma - n\Lambda, \tag{1.3}$$

where e is the internal energy per unit mass, γ is the ratio of specific heats, and $\Gamma = \Gamma(n, T)$ and $n\Lambda = n\Lambda(n, T)$, are the rates of radiative heating and cooling respectively, which in thermal equilibrium fulfill the condition $\Gamma - n\Lambda = 0$. These rates are described in Sec. 1.3.1.

The *magnetic flux conservation*, or the induction equation, for an ideal magnetohydrodynamic medium (MHD),

$$\frac{\partial \mathbf{B}}{\partial t} = \nabla \times (\mathbf{u} \times \mathbf{B}). \tag{1.4}$$

which describes the evolution of the magnetic field in the case of infinite conductivity. In the absence of magnetic fields the fluid equations can be simplified. In the above set of equations we include the B term for completeness.

Finally, the gravitational field is described in terms of the gravitational potential $-\nabla\phi$, which is related to the gas density through the *Poisson's equation*,

$$\nabla^2\phi = 4\pi G\rho, \tag{1.5}$$

where G is the gravitational constant.

This set of equations is suitable for describing the ISM since the characteristic length scale of the analyzed systems are several times larger than the mean free paths of the gas molecules (Shu, 1992). Equations (1.1 to 1.5) describe the evolution of the ISM during the star formation process while it is subject to multiple forces and different mechanisms that affect its energy and dynamics.

1.2 The structure of the ISM

1.2.1 Components and energy sources

.

The Milky Way contains matter inhomogeneously distributed into the interstellar space in the form of atoms, molecules, ions, electrons and tiny dust particles. The mass of the Galaxy within 15 kpc of the center is $\sim 10^{11} M_\odot$, of which $\sim 10-15\%$ is confined to the Galactic disk. This material includes $\sim 5\times10^{10} M_\odot$ of stars, $\sim 5\times10^{10} M_\odot$ of dark matter, $\sim 7\times10^{9} M_\odot$ of interstellar gas (Draine, 2011), and $3\times10^{7} M_\odot$ of dust, assuming a dust-to-gas mass ratio of 1:150 (Kruegel, 2003). The gas and the dust components are primordial in the evolution of the ISM. Some of their main characteristics are:

- **Gas**: In our Galaxy, most of the mass of the interstellar medium can be found in the gas phase. Its chemical composition (by number, see Ferrière, 2001) is 90.8% of hydrogen (H), 9.1% of helium (He), and 0.12% of heavier elements. Approximately 60% of the interstellar hydrogen mass is in H atoms, $\sim 20\%$ is in H_2 molecules, and $\sim 20\%$ is ionized (Draine, 2011). Most of the gas falls close to some characteristic states or "phases" such as molecular, neutral and ionized gas, both at different temperatures, see Sec. 1.2.2.

- **Dust**: This material was first detected by the obscuration and reddening of starlight. In the ISM, one expects a more or less constant dust-to-gas ratio, since dust is made up of metals such as carbon and silicon, and the mass fraction in metals is 1 % (Rohlfs, & Wilson, 1996). Even when dust represents a small fraction of the mass in the interstellar space, it has a crucial role. The dust grains contribute to the molecular hydrogen content (and other molecules) in the medium by promoting its formation, their surfaces act as catalysts for the conversion of hydrogen into H_2. In addition, dust grains provide some shielding against the interstellar radiation field to the H_2 molecule, since H_2 is dissociated by energetic photons, mainly ultraviolet radiation in diffuse gas. Furthermore, an indirect method to determine H_2 column densities is the measurement of the thermal emission from dust (Ferrière, 2001; Rohlfs, & Wilson, 1996).

The gas and dust are related in the ISM. The column density of neutral (both atomic and molecular) gas is associated to the dust extinction. The extinction is defined as the sum of the absorption and the scattering of the radiation (starlight) from a source (Rohlfs, & Wilson, 1996). Thus, the attenuation of the starlight by dust as a function of the wavelength, λ, can be determined. Measured in magnitudes it is proportional to the optical depth, τ:

$$\frac{\mathrm{A}_\lambda}{\mathrm{mag}} = 1.086\,\tau_\lambda. \tag{1.6}$$

In other words, the change in magnitude due to extinction is proportional to the optical depth along the line of sight. The dust responsible for interstellar extinction seems to be mixed with the gas, then the column density is also related to the extinction, e.g., for the visual extinction, $\mathrm{A_V}$,

$$\frac{\mathrm{A_V}}{N_\mathrm{H}} = 1.87 \times 10^{21}\,\mathrm{cm}^{-2}. \tag{1.7}$$

Depending on the extinction, the interstellar radiation incident on a region can penetrate much more easily or not, thus, the extinction can affect any predictions of its physical conditions.

Other important components of the ISM are the energetic particles and the radiation field that contributes to the heating and cooling of the medium, see Sec. 1.2.2. These elements of the ISM are:

- **Cosmic rays**: They consist of ions and electrons with velocities near the speed of light. These energetic particles fill the interstellar space contributing to the ionization of the interstellar matter and as a source of heating. Together with the magnetic field, they exert pressure on the interstellar matter affecting its dynamics, the hydrostatic balance of the ISM and its stability (Ferrière, 2001).

- **Radiation Field**: The radiation field consists of electromagnetic radiation from different types of sources including the starlight, the thermal emission from dust grains heated by starlight, the cosmic microwave background, free-free emission form interstellar plasma, synchrotron radiation and gamma rays (Draine, 2011). These fields contribute to heating and cooling (Sec. 1.2.2) processes in the ISM.

Together with the gas and dust, these components of the ISM are mixed in our Galaxy additionally to the magnetic field, which may play an important role in the star formation process:

- **Magnetic field**: In the ISM, magnetic fields, **B**, were detected 70 years ago through polarization effects (Hiltner, 1949). Davis & Greenstein (1951) concluded that the interstellar magnetic field is locally parallel to the Galactic plane, and according to Shu et al. (1987) the magnetic support of molecular clouds, which are primordial for star formation, is essentially provided by magnetic pressure gradients in the directions perpendicular to the average field. However, more recent observations suggest that the magnetic field is dynamically sub-dominant (Crutcher, 2012). In our Galaxy, the magnetic field is nearly constant at densities up to $n_H \sim 300$ cm^{-3}, with a value ~ 10 μG. For larger densities, B increases as a power-law of density $\sim n^{2/3}$, up to values ~ 1 mG at densities of $10^6 - 10^7$ cm^{-3} (see Fig.6 of Crutcher, 2012).

The interaction between these components allows the evolution of the interstellar matter to be gradually transformed into stars; part of this matter returns to the medium and some other is ejected out of the Galaxy. Throughout this process, the ISM is subject to a variety of forces that inject energy into it and impact on the process itself . Some of the most important energy sources are:

- **Gravity**: Gravity holds galaxies together. At smaller scales, this force has a key role in the star formation. It is due to self-gravity, that the gas in the ISM proceeds from large clouds to small dense cores and eventually to star formation.

- **Stellar Feedback**: Once the stars begin their nuclear reactions, they affect the interstellar medium through their radiation field and their stellar winds, and, at the end of their life, in some cases, also by the energy and the expelled matter from supernova explosions. These processes are known as stellar feedback. The injection of mass, momentum, and thermal, radiative, and bulk kinetic energies by these events contributes to maintain the inhomogeneous structure and the pressure gradients of the ISM. The thermal effect of these energy sources as well as the effects of radiative cooling, is represented through the heating (Γ) and cooling (Λ) functions in the energy equation (see Secs. 1.1 1.3.1). Furthermore, the material from stellar winds and supernova explosions contribute to the chemical enrichment of the medium.

The interplay between the components of the ISM and the physical process mentioned above cause the system to be far from equilibrium and highly inhomogeneous. Thus, rather than being uniformly distributed in density and temperature, the gaseous component of the ISM can exist in different phases.

1.2.2 Phases of the interstellar gas

The interstellar gas can be in different thermodynamic phases: ionizing photons from stars can convert cold molecular gas to hot HII (T$> 10^4$ K); radiative cooling can allow hot gas to cool to low temperatures; ions and electrons can recombine to form atoms, and H atoms can combine to form H_2 molecules (with T $\sim 10 - 50$ K). Thus, the gaseous component can be found in atomic, molecular and ionized form, with a wide distribution of densities and temperatures. According to McKee & Ostriker (1977) supernova explosions induce the existence of three phases in the ISM in pressure balance with each other. These phases are the hot ionized medium, the warm phase, and the cold phase. However, this model has been refined, with additional phases identified according to their distribution and pressure (Heiles, 2001; Ferrière, 2001; Draine, 2011; Klessen & Glover, 2016), and the assumption of pressure balance challenged, see below. The phases are:

- **Hot ionized medium (HIM)**: It has temperatures $T \gtrsim 10^6$ K and characteristic density $\sim 10^{-2}\,\mathrm{cm}^{-3}$. This hot ionized phase is induced by supernova explosions (McKee & Ostriker, 1977).

- **Warm ionized medium (WIM)**: The low-density photoionized regions are often referred to as the warm ionized medium. The temperature is T$\sim$ 8000

K[1] and the density is in the range $n \sim 0.2 - 0.5\,\mathrm{cm}^{-3}$ (Ferrière, 2001).

- **Warm neutral medium (WNM)**: Predominantly atomic gas heated to temperatures $T \approx 6000 - 10^4$ K. This gas is found at densities $n_{\mathrm{H}} \approx 0.6\,\mathrm{cm}^{-3}$. Its main component is the neutral atomic hydrogen (HI) which is not directly observable at optical wavelengths. The existence of the 21-cm line results from the splitting of the 1s ground state of the hydrogen atom due to the spin-flip transition.

- **Cold neutral medium (CNM)**: Predominantly atomic gas at temperatures $T \approx 50 - 100$ K, with densities $n \approx 30\,\mathrm{cm}^{-3}$ (Ferrière, 2001).

- **Dense molecular gas**: It is characterized by dense gas that have achieved $n_{\mathrm{H}} \gtrsim 10^3\,\mathrm{cm}^{-3}$ and temperatures $10 - 50$ K. This gas is found distributed in clouds at different masses and sizes. It is within these regions that star formation takes place (Ferrière, 2001).

The CNM and the WNM are, generally, in pressure equilibrium with each other in a stable regime (Field et al., 1969). However, there is a significant fraction of atomic gas at intermediate temperatures in the thermally unstable regime between the CNM and WNM (Vázquez-Semadeni et al., 2000b; Gazol et al., 2001), see Sec. 1.3.2. Since the 1970's, it was observed that hydrogen exhibited intermediate temperatures between the hot and cold hydrogen (Dickey et al., 1977). A few decades later, numerical works Ballesteros-Paredes et al. (1999); Vázquez-Semadeni et al. (2006) and Banerjee et al. (2009) showed that the interfaces between the WNM and the CNM are in general not isolating, but rather allow mass flux across them, so that the cold, dense gas accretes mass from the diffuse phase.

1.3 Physical processes in the ISM

1.3.1 Heating and cooling

The development of the phases in the ISM is a result of the density and temperature dependence of the heating, Γ, and cooling, Λ, processes. At macroscopic scales in the gas, heating processes correspond to adiabatic compressions while cooling is induced by adiabatic expansions (Mac Low & Klessen, 2004; Klessen & Glover, 2016),

[1] At the same temperatures, T$\sim$ 8000 K, we can identify the HII regions, which also consist of ionized gas. However, HII regions are constituted by denser gas than the WIM. Their main component is photoionized gas from massive stars, O- and B-type stars (Draine, 2011; Klessen & Glover, 2016), which is not consider part of the WIM.

while, at microscopic scales, the heating occurs through collisions between atoms, ions, molecules and dust grains, and interactions with radiation. The main heating mechanisms are: *photo-ionization*, it occurs when an energetic photon from a star ionizes an atom or an ion, thus, the energy excess of the ejected electron is given by the difference between the energy of the photon and the ionization potential of the initial particle; *cosmic ray heating*, cosmic rays can remove electrons from an ion or a molecule through collisions, these collisions increase the effective heating, and *photo-electric heating*, produced by photoelectrons ejected with an excess of kinetic energy when a photon hits a dust grain.

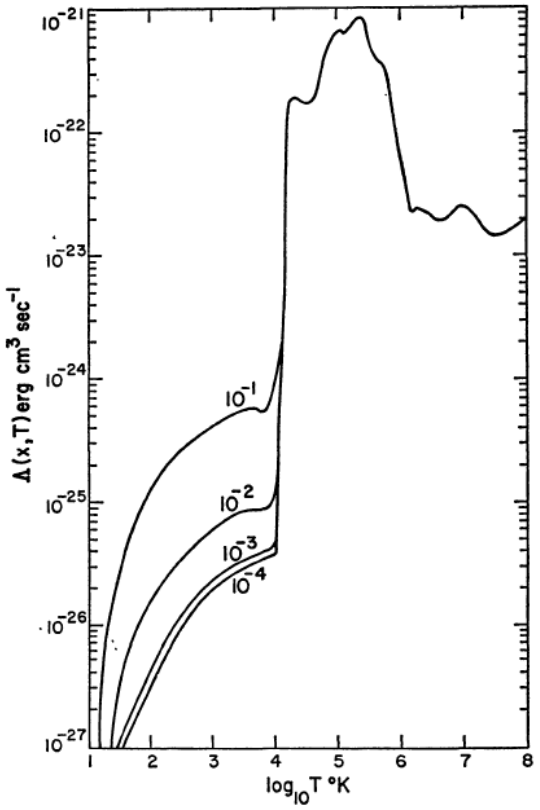

Figure 1.1: The interstellar cooling function at different ionization fractions (Dalgarno & McCray, 1972).

The cooling, on the other hand, results from the conversion of kinetic energy into radiation via collisional excitation of atoms and molecules followed by radiative decay, whose energy escapes from the system (Draine, 2011). The interstellar cooling function depends on the temperature, the cosmic rays, the radiation field, the metallicity, and on the ionization fraction $x = n_e/n_{\rm H}$. Figure 1.1 shows the dependence with the later. In a completely ionized gas, the cooling is due to bremsstrahlung, while in a partially ionized gas, it is due to electron impact excitation of the neu-

tral and ionized levels (at high temperatures of the electronic levels, and at low temperatures of fine structure levels; Dalgarno & McCray, 1972).

1.3.2 Thermal instability in the atomic ISM

It is known that the warm and cold phases of the atomic ISM can coexist over a narrow range of pressures (Field et al., 1969). Actually, the ISM is approximately isobaric, with a typical pressure $P \sim 3000\,\mathrm{K\,cm^{-3}}$.

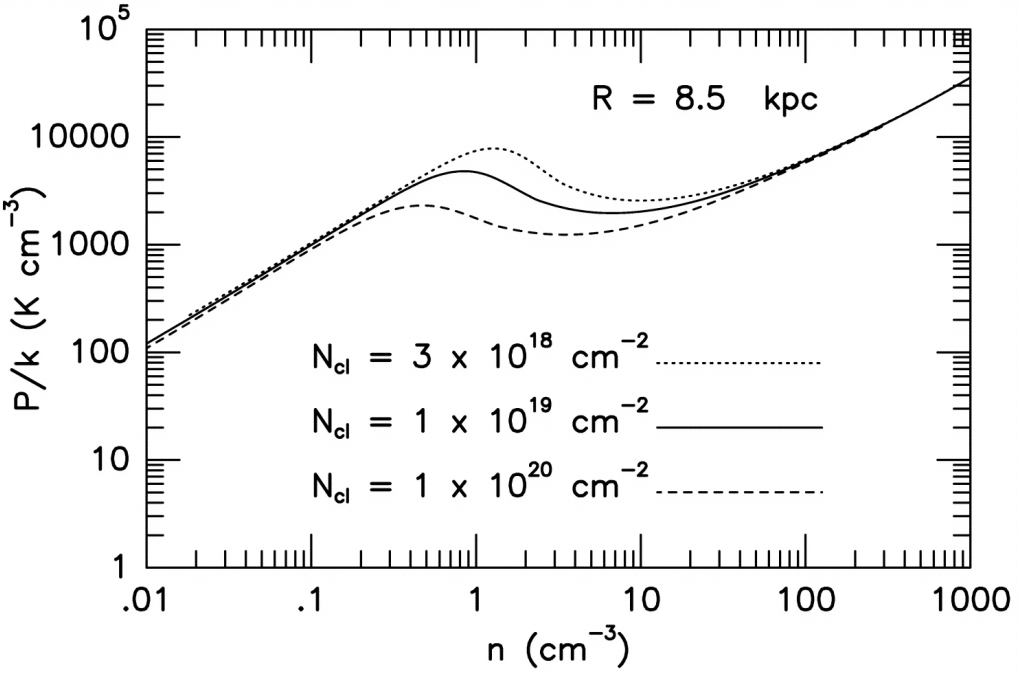

Figure 1.2: Thermal equilibrium pressure, Wolfire et al. (2003), for various values of WNM atomic column density at the Galactocentric distance of the Sun.

The condition for thermal equilibrium is that the heating and the cooling balance each other, $\Gamma(n,T) - n\Lambda(n,T) = 0$. Under this conditions, it is possible to express the equilibrium temperature as a function of the density or, via the equation of state, to write an expression for the pressure as a function of the density only, $P(\rho)$, which is referred to as the "thermal equilibrium pressure". Figure 1.2 shows the resulting form of $P_{eq}(\rho)$, where the solid curve indicates the locus of thermal equilibrium. The gas is thermally stable under the isobaric mode when the pressure increases for increasing density ($\mathrm{d}P_{eq}/\mathrm{d}\rho > 0$), and is thermally unstable if the pressure decreases with increasing density ($\mathrm{d}P_{eq}/\mathrm{d}\rho < 0$). In this case, a small density increment in a fluid parcel will cause its pressure to decrease as the system seeks thermal equilibrium. Then, the fluid parcel will be at a lower pressure than the ambient medium, which compresses the parcel even more, causing a runaway compression.

In the opposite case, if the density decreases in the parcel, its pressure increases and the opposite happens. The instability ends when the slope of the curve becomes positive again.

It has been found (see Fig.1.2) that there is only a narrow range of thermal pressure in which the gas can be at two densities and remain in pressure equilibrium. The atomic medium is thermally unstable at densities between $1 \leq n \leq 10\,\mathrm{cm}^{-3}$. When the gas is in this range, it spontaneously segregates in two phases, the warm, diffuse and the cold, dense phases, which are the stable equilibria at lower and higher density, respectively, and the same pressure (Field et al., 1969, and references therein). The cold gas, on the other hand, is expected to condensate into small clumps.

1.3.3 Gravitational instability

Another important instability for the formation of dense gas and stars is the gravitational instability. The stability of a gaseous medium of uniform density ρ_0 and sound speed c_s in the presence of self-gravity and thermal pressure was investigated by Jeans (1902). He found, by the use of the equations (1.1, 1.2, 1.5) without magnetic fields, that perturbations of wavelength λ larger than a critical value now called the Jeans length (L_J) are unstable and proceed to collapse, while perturbations of wavelength $\lambda < L_J$ are stable, and simply oscillate. The Jeans length was found to be given by

$$\lambda_J = \sqrt{\frac{\pi c_s^2}{G\rho_0}}, \tag{1.8}$$

which can be also described in terms of the temperature, since, for an ideal gas, the sound speed is defined as $c_s = \sqrt{k_\mathrm{B}T/\mu m_\mathrm{H}}$, where k_B is the Boltzmann constant, μ is the mean particle weight, and m_H is the hydrogen mass.

A mass scale is associated to this critical length scale by considering the mass in a sphere of diameter equal to the Jeans length, given by

$$M_\mathrm{J} = \frac{\pi^{5/2} c_s^3}{6G^{3/2}} \left(\frac{1}{\rho_0}\right)^{1/2}. \tag{1.9}$$

Once a dense object reaches the Jeans mass it becomes unstable and collapses. However, self-gravity does not act alone, it competes with other forces and physical processes like, turbulence, magnetic fields, radiation pressure, and shear. Then, the interplay between gravity and the competing forces is what determines the formation and collapse of the structure in molecular clouds, and the clouds themselves.

Chapter 2

Molecular Clouds

Regions in the ISM with sufficiently high density and size, allow the formation of hydrogen molecules, by allowing sufficiently high molecule formation rates on dust grains and avoiding molecule destruction by self-shielding.

Observations have shown that the molecular gas is organized self-similarly, like a fractal, in a hierarchy of structures from giant clouds to small dense cores (Larson, 1981; Goldsmith, 1987; Falgarone et al., 1992; Lada et al., 2008). Their observed shapes exhibit clumpy and filamentary structure over a wide range of scales. The boundaries between these structures are not well defined, as the phases in the interstellar medium can coexist and are mixed together. In general, since the ISM is a fluid, it is a continuum, and therefore clear boundaries between regions of typically different densities (from giant clouds to small clumps) are not common except for the shock, ionization, and phase transition fronts (Vázquez-Semadeni et al., 2006; Draine, 2011). Historically, these different types of structures have been identified through the use of different observational tracers, such as atomic or molecular line emission, but in terms of density, the medium is a continuum, often with smooth transitions between different classes of regions, and with the ability to exchange mass and energy between them (Ballesteros-Paredes et al., 1999). These clouds and their substructure contain half of the gaseous mass in the Galaxy. Star formation takes place in the densest regions within them (clumps, cores and filaments), although most of the clouds' mass remains at lower densities. Therefore, the understanding of their origin, their properties and their dynamical evolution is essential to understand star formation.

In the next section we will describe the main properties of molecular clouds and their substructures, their observed scaling relations and their role in the star formation process.

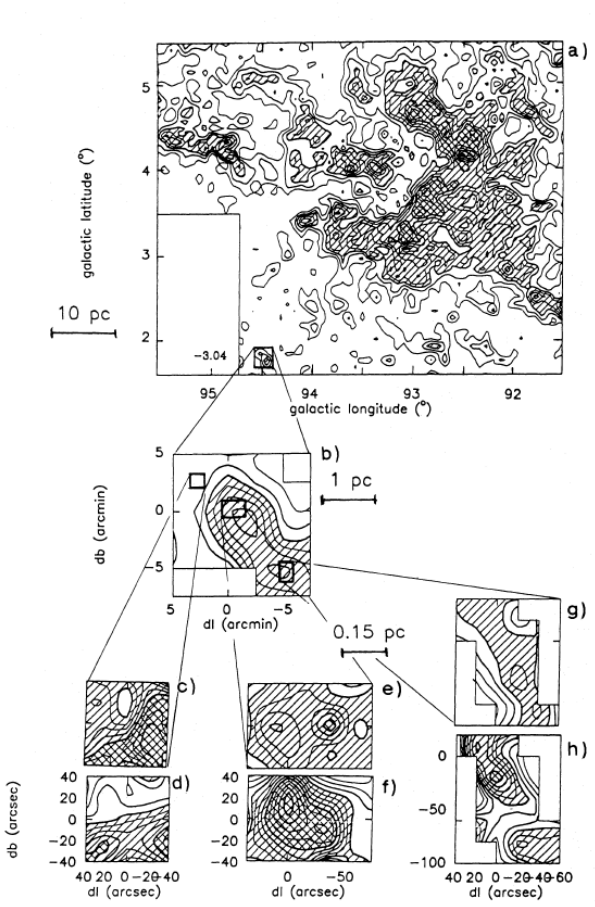

Figure 2.1: Map of the giant molecular cloud Cyg OB7 (Falgarone et al., 1992). High angular resolution observations show the internal hierarchical structure of the cloud.

2.1 The molecular gas hierarchy

The study of the molecular gas in our Galaxy from measurements of the CO emission lines, and other interstellar molecules, such as CH, CH^+ and NH_3, has allowed the identification of dense structures characterized by different densities and temperatures. Table 2.1 shows some of the values used to define the hierarchy of molecular structures.

	GMC	Molecular Cloud	Clump	Core
Size (pc)	10-100	2-20	0.1-4	< 0.1
Mass ($M_\odot$)	$10^4 - 10^6$	$10^2 - 10^4$	$10 - 10^3$	$1 - 10$
Density (n(H_2) cm^{-3})	100-500	$10^2 - 10^4$	$10^3 - 10^5$	$> 10^5$
Temperature (K)	15-40	10-30	10-30	10
Lindewidth ($km\,s^{-1}$)	5-15	1-10	0.3-4	0.1-0.7

Table 2.1: Adapted from Goldsmith (1987) and Mac Low & Klessen (2004).

The properties described in Table 2.1 are just guidelines, as there is no precise separation between the regimes. In this work we considered them as the values of reference as well as the classification of objects described below.

The largest identified molecular objects are *Giant Molecular Clouds* (GMC), which are inhomogeneous entities that contain a number of smaller and denser regions. GMCs can be formed by spiral-arm shocks, shear instabilities or Rayleigh-Taylor instabilities (Blitz, 1993, and references therein). Since the 1980's, giant molecular clouds have been considered to be in approximate virial equilibrium (Larson, 1981; Myers & Goodman, 1988) and supported against their self-gravity by magnetic fields (Shu et al., 1987; Mouschovias, 1991) or turbulence (Vázquez-Semadeni et al., 2000; Mac Low & Klessen, 2004; McKee & Ostriker, 2007; Ballesteros-Paredes et al., 2007). However, in the last two decades this interpretation has changed (see discussion in Sec. 2.3). GMCs are often observed to be the sites of massive star formation (Blitz & Thaddeus, 1980). Once massive stars are formed, they emit strong ultraviolet radiation inside the cloud resulting in an expanding ionized region, i.e., an HII region. The HII regions are thought to quench the further star formation and to destroy the parental molecular clouds (e.g. Blitz & Thaddeus, 1980; Blitz, 1993; Matzner, 2002; Murray, 2011; Hennebelle & Inutsuka, 2019, and references therein).

The next structures in the hierarchy are the isolated molecular clouds, or simply, *molecular clouds* (MCs). Even when they do not have well defined edges, observationally molecular clouds can be delimited by the abundance of some molecules, principally the CO molecule and its isotopologues, see Chap. 4. Furthermore, besides their molecular emission, it has also been observed that their envelopes and their interiors exhibit atomic emission (Goldsmith, 1987). Although all star formation in the Galaxy occurs in molecular clouds, not all molecular clouds exhibit star formation (SF) (Maddalena, & Thaddeus, 1985) . Moreover, the level of SF activity varies among clouds of similar conditions, for example Orion (A) and the California clouds with similar masses but the latter with lower star formation (Lada et al., 2009; Barnes et al., 2013, 2016, 2018). Thus, the star formation process depends on the dynamics of molecular clouds and their physical conditions, like density. Similarly to the GMCs, molecular clouds have been considered as bound objects in approximate virial equilibrium.

Embedded in molecular clouds, denser and more compact objects have been observed; these regions are termed *clumps*. The clumps are objects identified obser-

vationally from spectral line maps of molecular emission, which are generally gravitationally bound. Stellar clusters are thought to be formed from massive clumps (Williams et al., 2000).

At even smaller scales it is possible to identify dense *cores*. These regions are thought to be the seeds of individual stars or multiple systems, where the material came not just from the core, but also some may be accreted from the surrounding medium (a clump or a cloud), or by a fragmentation process (Bonnell et al., 1997; Bonnell, 1997). Their definition varies depending on the techniques and the methods used to select them which can vary from author to author. Some of the algorithms used are the CLUMPFIND algorithm (Williams et al., 1994), which applies a segmentation technique and the GAUSSCLUMP algorithm (Kramer et al., 1998), which fits Gaussians to a data cube (see Ch. 4). Despite the ambiguity in the definition and geometry, most cores used to appear near virial equilibrium (Myers, 1991). However, numerical and observational studies in the last decade have shown the existence of dense cores out of this state (see Sec. 2.2.3).

2.1.1 Filaments

It has been recognized, for many years, that the ISM is remarkably filamentary. In the late 70's Schneider & Elmegreen (1979) reported a catalog with elongated structures, which were called globular filaments. Since then, filamentary structure has been found at all scales (Schneider & Elmegreen, 1979; Loren, 1989; Williams et al., 2000; Goldsmith et al., 2008). Recently, the Herschel Space Observatory has provided high-density maps of the cold ISM, traced by cold dust, where the ubiquitous existence of filaments has been confirmed (Arzoumanian et al., 2011; André, 2017; Arzoumanian et al., 2019). Herschel studies have revealed statistical properties for the filaments, like the observed range of column densities and masses, and possibly a characteristic width for nearby molecular clouds (André et al., 2013). Additionally, filaments are thought to be important on the star formation process, since, it has been observed that most star forming cores sit inside self-gravitating filaments (Hennebelle & Inutsuka, 2019, and references therein).

In addition to the physical properties, like size and density, the kinematics of a cloud and its embedded structures reflects the motions that brought the gas to its current configuration and predicts the cloud's evolution (Loren, 1989). Then, the study of possible correlations between the physical parameters derived from the

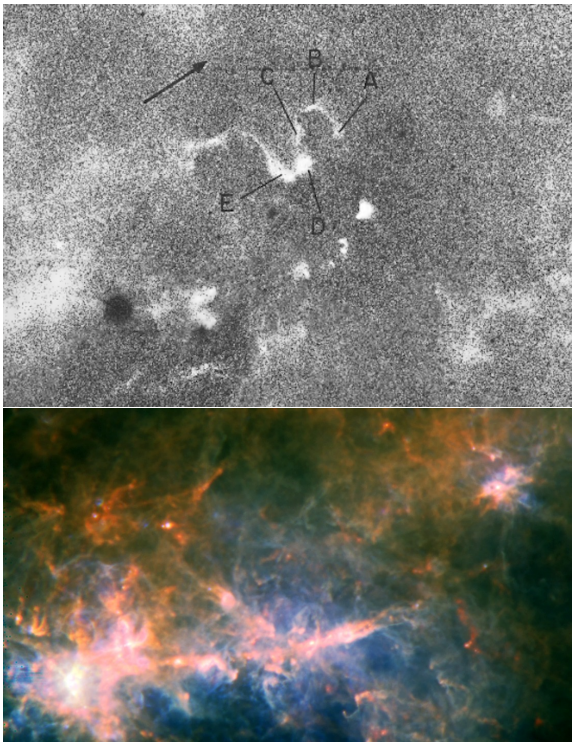

Figure 2.2: Upper image: Filamentary structure, or "globular filaments", form the early study of Schneider & Elmegreen (1979), denser condensations are observed inside these elongated structures. Lower image: filamentary structure observed by the Herschel Space Observatory, view of the G49 filament.

observations may be important to understand the internal structure and evolution of the interstellar filaments and molecular clouds, clumps and cores.

2.2 Scaling relations

Understanding the properties of the sites of star formation and being able to predict their long-term evolution requires a detailed knowledge of the dynamics and energetics of the molecular clouds. A first step in this process has been the identification of the scaling relations existing between their observed properties.

2.2.1 Larson's scaling relations

Using previously-published data of many molecular clouds, Larson (1981) found a power-law correlation of the velocity dispersion and the density with the size of the cloud. These relations were confirmed observationally some years later (Dame et al., 1986; Solomon et al., 1987; Myers & Goodman, 1988). Today they are known as the "Larson's relations" or the "Larson's laws". The relations observed by Larson

(1981), Fig. 2.3, are:

$$n(\mathrm{H_2})(\mathrm{cm^{-3}}) = 3400\, L(\mathrm{pc})^{\beta}, \tag{2.1}$$

$$\sigma_{v,3\mathrm{D}}(\mathrm{km\,s^{-1}}) = 1.10\, L(\mathrm{pc})^{\delta}, \tag{2.2}$$

where n is the average number density, L is the region size, and $\sigma_{v,3\mathrm{D}}$ is the three-dimensional velocity dispersion derived from the observed radial velocities and linewidths. The exponents reported by Larson were $\beta = -1.10$ and $\delta = 0.38$. According to these relations, Larson (1981) concluded that:

(i) Relation (2.1) implies that the column density ($\Sigma \sim nL$) is nearly independent of size, i.e., molecular clouds tend to have roughly the same column density.

(ii) According to relation (2.2), the velocity dispersion increases systematically with the region size with a power-law similar to the Kolmogoroff law ($\sigma \propto L^{1/3}$), appropriate for incompressible and mildly compressible (subsonic, with rms Mach number $\lesssim 0.3$; Passot & Pouquet, 1987) turbulence. Thus, the motions considered are part of a hierarchy of interstellar turbulent motions.

(iii) Most of the regions studied are gravitationally bound and at least approximately in virial equilibrium. Thus, the observed internal velocities support clouds against collapse.

In the same work, Larson (1981) pointed out some considerations to take into account: the density-size relation may be the result of observational effects due to the limited range of column density detectable with some techniques and, given that the free-fall velocity differs only by a factor of $\sqrt{2}$ from the one corresponding to virial equilibrium, then deviations from the velocity dispersion-size relation can be related to gravitational contraction, indicating that some clouds may be collapsing. Despite these caveats, Larson's relations and their turbulent interpretation, points *i*) to *iii*), have been considered as representative properties of molecular clouds.

Different observational works have searched for the Larson's relations in MCs. They are observed to apply to different clouds as well as some clumps inside them (Solomon et al., 1987; Caselli & Myers, 1995; Heyer & Brunt, 2004). The most accepted values for the exponents in equations (2.1) and (2.2) at present are $\beta \approx -1$ and $\delta \approx 0.5$ (Heyer & Brunt, 2004; Ballesteros-Paredes et al., 2011, and references therein). This value for δ is expected for a supersonic turbulent flow dominated by

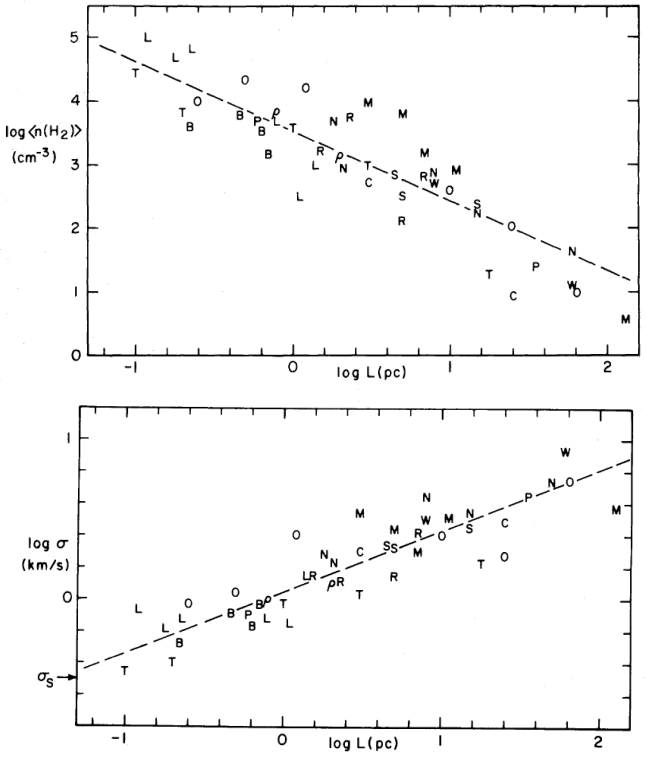

Figure 2.3: Larson scaling relations (Larson, 1981).

shocks, such as the interstellar medium, which is highly compressible. Additionally to the observational works, analytical calculations and numerical simulations have supported these relations. For example, the velocity dispersion-size relation has been studied in works like Vázquez-Semadeni et al. (1997); Ballesteros-Paredes et al. (1999b); Ballesteros-Paredes & Mac Low (2002). However, some other studies, both numerical and observational, have provided evidence showing that the Larson's relations are not universal. For example, Keto & Myers (1986) presented a study of CO observations of high-latitude clouds that span three orders of magnitude in column density, contradicting the constancy of Σ suggested by Larson. Additionally, they suggested that denser clouds may be confined by an external pressure. This differs from the turbulent support and virial equilibrium proposed in Larson (1981). Actually, Bertoldi & McKee (1992) surveyed a series of observational works reporting that only the largest and most massive clumps are self-gravitating, whereas the smaller clumps appear to be confined by some external pressure. On the other hand, Kegel (1989) showed that the constant column density suggested by Larson implies that clouds should have approximately the same extinction, A_V, which contradicts the studies showing $2 \leq A_V \leq 20$ (e.g. Frerking et al., 1982). Thus, Kegel (1989) proposes that the density-size relation is the result of an observational selection

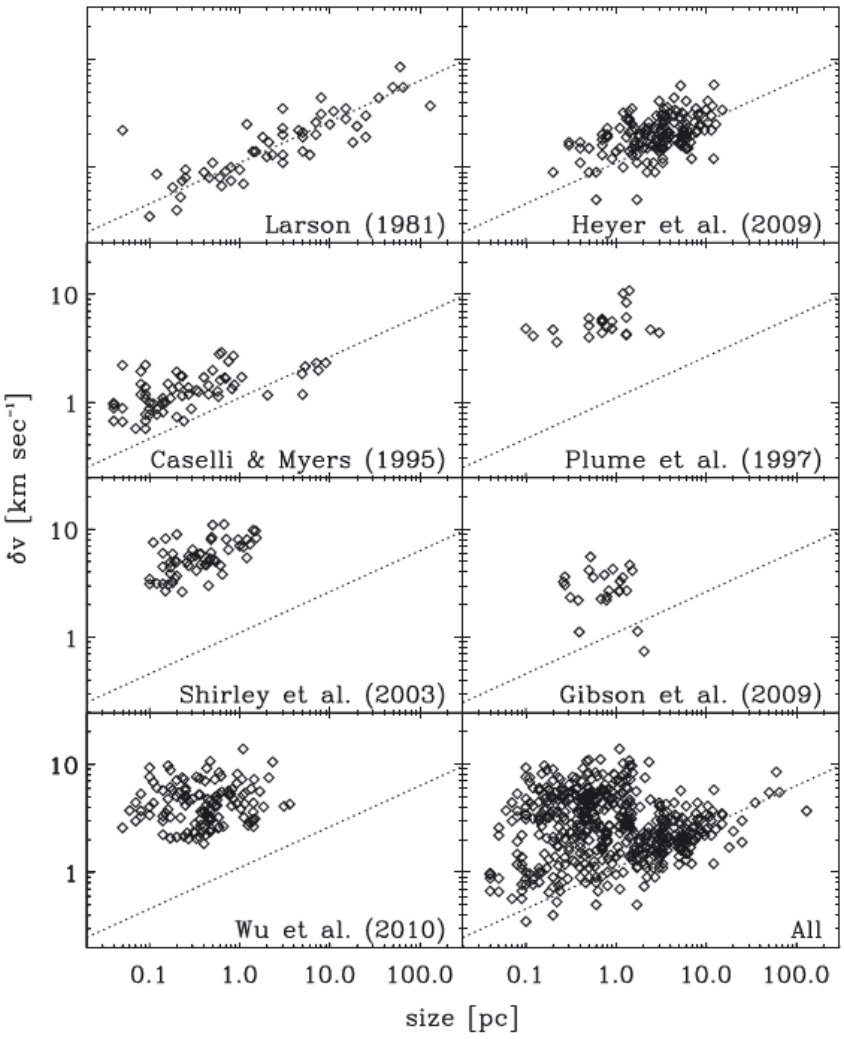

Figure 2.4: Velocity dispersion-size relation observed clouds and clumps from different studies (Ballesteros-Paredes et al., 2011).

effect. Additionally, other numerical and observational works contradict the density-size relation arguing that the dynamical range of the observations is limited by the sensitivity of the telescopes, saturation of the detectors, optically thick effects, and depletion (Scalo, 1990; Ballesteros-Paredes & Mac Low, 2002; Ballesteros-Paredes, 2006). Concerning the velocity dispersion-size relation, Ballesteros-Paredes et al. (2011) showed a compilation of objects from molecular clouds to dense cores in velocity dispersion versus size plots (Fig. 2.4). It can be seen that Larson's velocity dispersion-size relation does not apply to all of them, especially for the dense massive cores. Additionally, studies on intermediate- and high-mass clumps (Barnes et al., 2011, 2018) have shown that these objects do not exhibit the velocity dispersion-size relation and neither constant column-density. Moreover, Traficante et al. (2018) showed that this Larson relation varies for massive objects at different evolutionary

stages. These works show that Larson's relations appear to apply to objects selected to have roughly the same column density, but not to the full sample of the clouds and their internal clumps, and cores.

2.2.2 Generalization of Larson's relations

Two decades after the work by Larson, Heyer et al. (2009), hereafter H09, studied a set of clouds that were previously investigated by Solomon et al. (1987). Both surveys were performed with the same telescope (Five College Radio Astronomy Observatory, 14m) but with significant differences. The H09 sample was observed with ^{13}CO and a multiple-pixel camera, while the survey in 1987 was performed with ^{12}CO and a single-pixel detector. The sample by Solomon et al. (1987) has been considered as evidence in favor of the Larson scaling relations. However, H09 found that the ratio $\sigma_v/R^{1/2}$, which according to Larson ($\sigma_v \propto R^{0.5}$) should be constant, varies with the column density as $\Sigma^{1/2}$. Note that H09 define σ_v as the one-dimensional velocity dispersion, following Bertoldi & McKee (1992). This conflicts with both of Larson's velocity dispersion-size and density-size scaling relations. Instead, the scaling found by H09 follows the relation

$$\frac{\sigma_v}{R^{1/2}} = \left(\frac{\pi G \Sigma}{5}\right)^{1/2}, \tag{2.3}$$

which shows that neither $\Sigma \sim$ constant or the Larson's velocity dispersion-size relation are applicable, since the cloud sample studied by H09 exhibited a column density range of nearly two orders of magnitude. Also, H09 noted that most of the clouds tend to be above the virial equilibrium line (again, see Fig. 2.5), and interpreted this in terms of a possible systematic underestimation of the clouds masses due to the techniques used.

Field et al. (2011), on the other hand, interpreted the results from H09 as an indication that the clouds are not sufficiently self-gravitating, so that their internal turbulence would disperse them, unless they are confined by an external pressure. Similarly to Keto & Myers (1986), Field et al. (2011) suggested that the kinetic energy excess of the clouds over their gravitational energy must be balanced by a confining external pressure that prevents the clouds from expanding.

A radically different scenario was proposed by Ballesteros-Paredes et al. (2011) to explain the deviations from eq. (2.3) in H09 data. Instead of attributing this correlation to virial equilibrium, Ballesteros-Paredes et al. (2011) point out that the correlation agrees better with free-fall. They argue that the free-fall relation implies

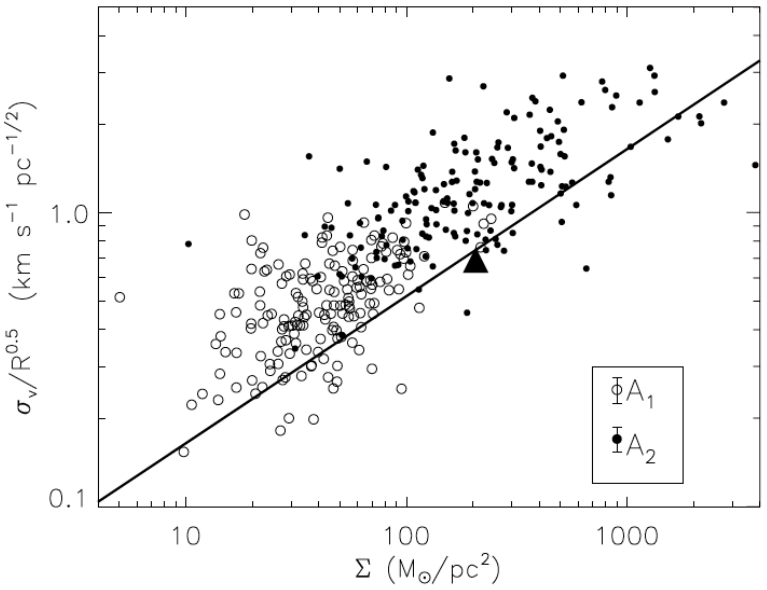

Figure 2.5: Scaling of the velocity dispersion with the column density (Heyer et al., 2009). The solid line indicates the virial equilibrium condition for a uniform-density sphere, eq. (2.3).

larger velocity dispersions than the virial equilibrium by a factor of $\sqrt{2}$, and thus clouds with high velocities are not unbound or confined by an external pressure but in gravitational contraction. This suggestion has been supported by observational and numerical works (e.g. Camacho et al., 2016; Traficante et al., 2018; Ballesteros-Paredes et al., 2018).

The relation proposed by Heyer et al. (2009) generalizes the Larson scaling relations. We call this relation the *generalized Larson scaling relation*,

$$\sigma_v/R^{1/2} \propto \Sigma^{1/2}, \tag{2.4}$$

where the ratio $\sigma_v/R^{1/2}$ has been referred to as the $\mathcal{H}$ parameter (Camacho et al., 2016), or the Larson ratio, $\mathcal{L}$, Ballesteros-Paredes et al. (2018),

$$\mathcal{H} = \mathcal{L} \equiv \frac{\sigma_v}{R^{1/2}}. \tag{2.5}$$

In this thesis we settle on the symbol $\mathcal{L}$ for this quantity. The study of molecular clouds and their substructure in terms of relation 2.2.2 is one of the main objectives of this work.

For constant column density, $\Sigma \propto nR$, relation (2.4) implies both Larson's relations,

$$\begin{aligned} \sigma_v &\propto R^{1/2} \quad velocity\ dispersion - size\ relation, \\ n &\propto R^{-1} \quad\quad\quad\quad\quad density - size\ relation, \end{aligned} \tag{2.6}$$

Thus, Larson's relations are a special case of Heyer et al. (2009)'s generalized relation, satisfied for constant column density.

2.2.3 Virial Parameter

An alternative way of describing the energy balance of clouds and their substructures is by means of the so-called *virial parameter*.

In its simplest form, assuming spherical geometry, the absence of external pressure and magnetic field, the virial parameter α denotes the ratio of twice the kinetic energy over the gravitational energy, $2E_k/|E_g|$. Thus, α can be expressed in the form (Bertoldi & McKee, 1992):

$$\alpha \equiv \frac{5\sigma_v^2 R}{GM}, \tag{2.7}$$

where G is the gravitational constant.

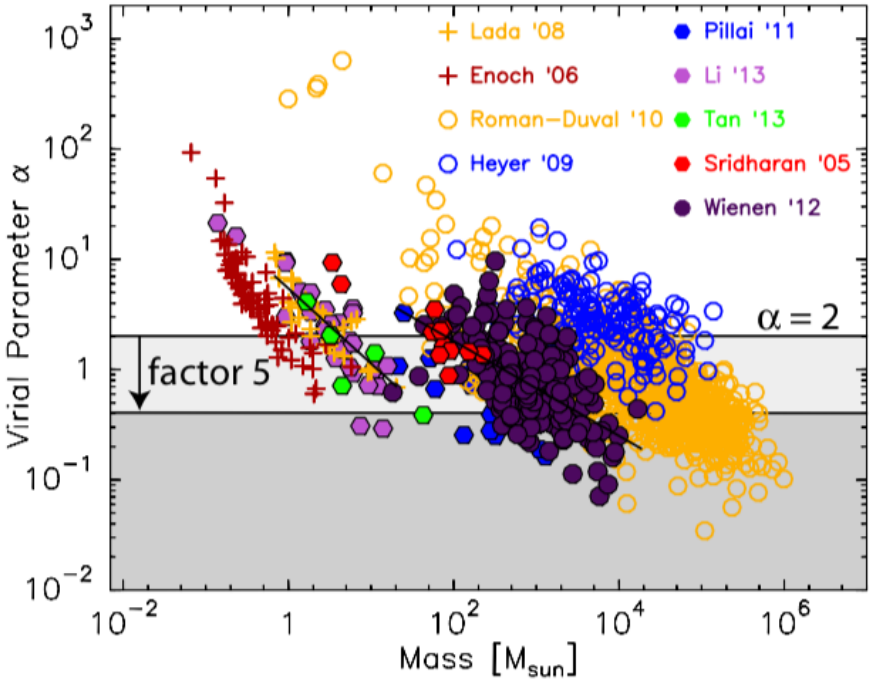

Figure 2.6: Virial parameter for different samples (Kauffmann et al., 2013).

The values of the virial parameter of the order of unity, found by Larson (1981),

contributed to establish the notion that MCs and their substructures are in near virial equilibrium (VE)[1]. Additionally, he stated that GMCs are mostly gravitationally bound objects. Correspondingly, clouds with $\alpha > 1$ have been regarded as unbound objects, out of virial equilibrium.

Nevertheless, in recent years, a number of observational and numerical studies have shown that most of the observed clumps have virial parameters $\alpha \gg 1$ (Leroy et al., 2015; Traficante et al., 2018), while high-mass star formation regions have been observed with low α values (Kauffmann et al., 2013). Therefore, there is a large range of α values observed in molecular clouds and their substructure. Figure 2.6 shows a compilation of virial parameters for different observational samples by Kauffmann et al. (2013).

According to Kauffmann et al. (2013), the unbound cloud fragments, called "subcritical", may expand and dissolve back into the diffuse interstellar medium. On the other hand, bound or marginally gravitationally bound clouds can undergo collapse when perturbed; they are referred to as "supercritical". In this context, the virial parameter can be used as a measure of whether a cloud fragment is subcritical or supercritical.

2.3 Star formation

2.3.1 Molecular cloud stability

Whether the molecular clouds and their substructure are in a state of virial equilibrium or in gravitational contraction, bound or unbound, and whether these conditions are the consequence of turbulent motions, of the free-fall condition or of external forces, is currently a matter of debate.

Goldreich & Kwan (1974) noted that the observed velocity dispersions in MCs could correspond either to cloud-scale systematic motions (presumably gravitational collapse), or to small-scale random motions (small-scale turbulence). Then they argued that, if these differences were the result of supersonic turbulence, a strong source of mechanical energy would be needed in order to maintain the turbulence against decay. Furthermore, those authors argued that, in a turbulent scenario, the thermal pressure is highly inadequate to maintain the clouds in hydrostatic equilibrium. Therefore, they concluded that the observed velocity differences arise from large-scale velocity gradients across the cloud. Since the turbulence seemed not

[1]For isothermal spheres, or Bonnor-Ebert spheres, the hydrostatic equilibrium implies $\alpha \simeq 2$ (Kauffmann et al., 2013)

to balance the clouds' self gravity, the clouds should be in a state of gravitational collapse. This scenario was dismissed by Zuckerman & Evans (1974) and Zuckerman & Palmer (1974), who argued that it would be inconsistent with the star formation activity observed in the Galaxy. They argued that, if all molecular clouds were collapsing, the star formation rate (SFR) would be approximately $30\,M_{\odot}\,\mathrm{yr}^{-1}$. At that time, the reported Galactic SFR was approximately $4\,M_{\odot}\,\mathrm{yr}^{-1}$ (at present, the observed value is $\sim 2\,M_{\odot}\,\mathrm{yr}^{-1}$; Chomiuk & Povich, 2011). Then, the low observed rate of star formation could be explained if only a small fraction of the linewidth were due to collapse. Zuckerman & Evans (1974) explained the differences in radial velocities as random motions of the cloud fragments instead of cloud-scale systematic motions. The arguments against the clouds gravitational collapse led to the search for new interpretations of the observed motions trying to explain the dynamical state of the clouds.

In order to understand why the observed molecular clouds in our Galaxy are in approximate virial equilibrium different scenarios have been proposed. The most common ones are briefly described here.

- The magnetically-supported model (e.g. Shu et al., 1987; Mouschovias, 1991), in which the magnetic fields provide support against self-gravity. In this model a cloud can be either magnetically subcritical or magnetically supercritical. In the first state, the cloud is supported by the magnetic field against its own gravity, however it can form low-mass stars through ambipolar diffusion. On the other hand, magnetically supercritical clouds are not supported against collapse so they collapse globally and can form massive star-forming regions.

- The turbulent model (e.g. Vázquez-Semadeni et al., 2000; Padoan & Nordlund, 2002; Mac Low & Klessen, 2004; McKee & Ostriker, 2007; Ballesteros-Paredes et al., 2007), which suggests that the non-thermal motions correspond to strongly supersonic turbulence that can be driven by stellar feedback in order to maintain the clouds supported against collapse. In this model, the turbulence has a dual role: globally, it supports the cloud against collapse and locally, it produces density enhancements that may form the substructures of the clouds.

In these scenarios the clouds and their substructure can be stabilized against gravitational collapse through the support of turbulent pressure and magnetic fields, so the clouds are near the virial equilibrium. However, other possibilities in addition to turbulent virial equilibrium have been explored.

In particular, the Global Hierarchical Collapse model (GHC; e.g. Vázquez-Semadeni et al., 2007; Klessen & Hennebelle, 2010; Ballesteros-Paredes et al., 2011; Colín et al., 2013; Carroll-Nellenback et al., 2014; Vázquez-Semadeni et al., 2017, 2019) proposes a return to the original idea of Goldreich & Kwan (1974), that MCs are in the process of global gravitational collapse. In this model, turbulence is not enough to support the clouds. Instead, the clouds and their substructure are not in equilibrium but rather in global gravitational contraction, which starts after the mass exceeds the thermal Jeans mass (Vázquez-Semadeni et al., 2007). The clouds initiate their lives as a result of phase transitions caused by large-scale motions in the warm diffuse gas, which trigger a transition to the cold atomic phase (Hennebelle & Pérault, 1999; Koyama & Inutsuka, 2000, 2002). These initial fluctuations are subject to continued accretion from the surrounding medium. Later, as the gas increases its mass, it becomes Jeans unstable and begins to collapse. Thus, the non-thermal turbulent motions consist primarily of gravitational collapse. Global gravitational contraction has been supported observationally through kinematic studies of molecular clouds and filaments (Galván-Madrid et al., 2009; Peretto et al., 2013; Hacar et al., 2017). In agreement with this scenario, Ballesteros-Paredes et al. (2011) suggest that the generalized Larson scaling relation, eq. (2.4) can be interpreted as the result of gravitational collapse at all scales, rather than virial equilibrium. The problem of an excessive SFR is avoided by the asynchronous collapse of the different scales, which allows the majority of the cloud's mass to be dispersed by the feedback of the first massive stars to appear in the cloud (Vázquez-Semadeni et al., 2017, 2019).

2.3.2 Star formation efficiency

One fundamental property of MCs is their star formation activity, measured either as the rate at which it forms stars (the star formation rate, or SFR), or as the time-integrated mass fraction of a cloud that has been converted to stars over its lifetime, called the star formation efficiency (SFE), which is defined as

$$SFE = \frac{M_*}{M_* + M_g}, \tag{2.8}$$

where M_* is the mass of the newborn stars and M_g is the cloud mass. Note that the SFE is time-dependent as well. Thus, the SFE will evolve from 0 to some value < 1 during the cloud lifetime. The SFE is a function of space and time, but it also depends on the region and its intrinsic properties, which in turn depend on how the region is defined. A natural time unit to be considered would be the free-

fall time, t_{ff}. For this case, Krumholz & McKee (2005) suggest a *star formation efficiency per free-fall time* in terms of the instantaneous star formation rate, see next section, as $\mathrm{SFE}_{ff} = SFR/(M_g/t_{ff})$. In any of these forms, instantaneous or per free-fall time, as new stars are formed the SFE should increase. Note, however, that Vázquez-Semadeni et al. (2019) have pointed out that the SFE_{ff} is ill-defined in the case that MCs are in global contraction, since in this case the free-fall time is time-dependent as well.

Observations and simulations suggest that the SFE is very low. It varies depending on the analyzed region, e.g., $\sim 1\%$ for molecular cloud complexes ($\sim 10^6 M_\odot$) (Myers et al., 1986), 10% for cluster forming clouds (Galván-Madrid et al., 2013; Ginsburg et al., 2016), $\sim 10-30\%$ for cluster forming clumps (Lada & Lada, 2003), and $\sim$ 30% for dense cores (Alves et al., 2007). Theoretically, Matzner & McKee (2000) investigated the disruption of dense cores by protostellar outflows concluding that the disruption of individual cores can produce SFE between $25-75\%$. Shu et al. (2004) have developed a self-consistent analytical theory where cores are formed from magnetized turbulent gas and are disrupted by outflows with a resulting SFE $\approx 30\%$. More recently, Zamora-Avilés & Vázquez-Semadeni (2014) developed an analytical model where low-to-intermediate-mass ($M \lesssim 10^4 M_\odot$) clouds exhibit a mean SFE $\sim 1\%$ reaching values of $\sim 60\%$ at the end of their life, when the clouds have gone through the cluster-forming-clump stage, and a star formation burst has been produced that destroyed them, leaving a naked cluster behind. In general, theoretical models have tried to explain the observed efficiencies in terms of either large-scale turbulence that supports the clouds (e.g. Krumholz & McKee, 2005; Padoan & Nordlund, 2011; Federrath & Klessen, 2012), or feedback from massive stars that disrupt the clouds at early stages (e.g. Zamora-Avilés et al., 2012; Colín et al., 2013; Dale et al., 2014; Myers et al., 2014; Haid et al., 2019).

2.3.3 Star formation rate

Similarly to the definition of the star formation efficiency, the instantaneous star formation rate (SFR) can be expressed as the amount of gas that is transformed into stars over a certain time, i.e.,

$$SFR = \frac{dM_*}{dt}. \tag{2.9}$$

As already mentioned in Sec. 2.3.1, one of the main arguments against the gravitational collapse model was the low value of the observed Galactic SFR. Zuckerman

& Evans (1974) argued that, if the clouds were in global collapse, the SFR in the Galaxy would be much greater than the observed at least one order of magnitude. The mechanisms that have been proposed in order to explain the observed SFE apply also to explain the observed SFR. Among these models, the suppression of the star formation activity in the context of the Global Hierarchical Collapse (GHC) scenario has been explained by Vázquez-Semadeni et al. (2010) and Zamora-Avilés et al. (2012), in the gravitational collapse scenario, as the destruction of molecular clouds early in their evolution (Kruijssen et al., 2019) by stellar feedback, even before ∼10% of their mass is converted into stars, i.e, the clouds are destroyed by their own stellar products (e.g. Whitworth, 1979; Cox, 1983; Elmegreen, 1983). Thus, the radiation of massive stars (ionizing photons, radiation pressure, winds and supernova explosions) can regulate the SFR. More recently, Zamora-Avilés & Vázquez-Semadeni (2014) suggest a model in which the mass (at high densities) and consequently the SFR initially increase over time and, once the SFR is high enough, the feedback from the massive stars evaporates the cloud. Observations (e.g. Blitz & Thaddeus, 1980; Brunt et al., 2003; Blitz et al., 2007) of molecular clouds immersed in an atomic envelope, and numerical simulations (e.g. Ballesteros-Paredes et al., 1999; Koyama & Inutsuka, 2002; Vázquez-Semadeni et al., 2007) of the formation of clouds from the WNM, where the clouds accrete mass, support the mass increment of this model.

Chapter 3

Numerical simulations of the ISM, molecular clouds and star formation

Numerical simulations have become an essential tool in astrophysics. Without them the progress in our understanding of the universe would be much less complete. In astrophysics, simulations have been used to study the formation and evolution of multiple systems at multiple scales, from protoplanetary discs to the cosmic web, including galaxy formation, ISM, molecular clouds, supernovae, outflows, star clusters and many other interesting topics. Simulations have also been used to reproduce multiple physical conditions such as gravitational collapse, stellar feedback, stellar dynamics, turbulence, magnetic fields, N-body problems, tidal forces, thermodynamic problems and more. The first simulations and analytical calculations were often restricted to idealized problems. Nowadays it has become possible to bring them closer to reality by introducing an ever-increasing number of physical processes. However, as important as including many physical processes in detail is, it is not less important to set up realistic initial and boundary conditions, as otherwise the system simulated may not correspond to the actual physical system one aims to describe. For example, if MCs are undergoing global gravitational contraction, a simulation designed to maintain support for the clouds (by either applying continuous driving in Fourier space, or preventing the stellar feedback energy to escape from the numerical box, by choosing too small a box size together with periodic boundary conditions) will not be able to correctly represent the cloud regardless of how much detail is included in modeling the feedback or the radiative transport.

3.1 Star formation scenarios in numerical simulations

In the star formation field, simulations of the ISM have been developed in order to study the main mechanisms of cloud formation. Depending on the initial conditions they can represent a certain phase of the ISM and incorporate the processes that allow the development of its structure and dynamics.

A number of studies of the ISM have shown that the formation process of cold dense HI gas from the WNM is a phase transition that increases the density abruptly (Hennebelle & Pérault, 1999; Koyama & Inutsuka, 2000) that could be triggered by large-scale flows in the medium. Models of the thermally bistable medium including the cooling of the atomic gas (Piontek, & Ostriker, 2004, 2005; Brandenburg et al., 2007) suggest that the phase transition induces turbulent motions where cold HI clumps are embedded in the warm neutral medium. Thus, molecular cloud formation may result from generic compressions in the WNM, which can be induced either by larger-scale instabilities (such as kpc-scale magneto-Jeans instability, Kim et al., 2002), the stellar spiral potential well, or generic turbulence in the diffuse medium.

3.1.1 Driven turbulence simulations

Turbulence has been considered as the main mechanism for cloud formation and evolution. The study of this process in numerical simulations has allowed a statistical description of the fluctuations arising in molecular clouds.

The simplest way to simulate turbulence in the medium is to continuously drive it through a numerical prescription that generates velocity fluctuations in Fourier space (e.g., Passot & Pouquet, 1987; Stone et al., 1998; Federrath et al., 2008) and continuously applies it to the flow, in which case it is referred to as *driven* turbulence (e.g., Padoan & Nordlund, 1999; Heitsch et al., 2000; Vázquez-Semadeni et al., 2003, 2005, 2008; Federrath & Klessen, 2013), or applies it at the beginning only, and lets it decay afterwards, in which case it is referred to as *decaying* turbulence (e.g., Ostriker et al., 1999; Bate et al., 2003; Li & Nakamura, 2004; Heiner et al., 2015; Vázquez-Semadeni, 2015). An alternative way to continuously drive the turbulence is to maintain a prescribed SFR, and apply an energy injection mechanism such as supernova explosions (e.g. de Avillez & Breitschwerdt, 2005; Joung & Mac Low, 2006; Padoan et al., 2016).

3.1.2 Colliding flows simulations

One problem with the method of Fourier-driving of turbulence is that the turbulence is applied at every point in space, and at a rate and scale prescribed by the user, rather than in a self-consistent manner.

Turbulence in the ISM is driven by either stellar feedback or large-scale instabilities. If the turbulence is supersonic, large density enhancements are produced by shocks or the formation of compressed layers at the interfaces of oppositely-directed flow streams. In general, the compressions can be the result of either the transonic turbulence in the WNM, or of the gravitational potential of the stellar spiral arm. The expected typical velocities for the colliding streams in either case are $\sim 10\,\mathrm{km\,s^{-1}}$ (e.g., Roberts, 1969; Heiles & Troland, 2003). In turn, the compressed layers develop turbulence by the combined action of several instabilities in a self-consistent manner (e.g. Vishniac, 1994; Heitsch et al., 2006).

Therefore, a class of numerical simulations, known as "colliding-flow simulations", has arisen, in which the initial condition is a pair of oppositely directed gas streams in the WNM, which form a dense layer by cooling, and the layer becomes turbulent by the combined action of the instabilities. In this kind of simulations the cloud starts as a two-dimensional thin shocked layer where nonlinear density fluctuations will form due to a variety of instabilities (e.g. Vázquez-Semadeni et al., 2006; Heitsch et al., 2006). This way realistic velocity dispersions and density fluctuations are generated, forming a turbulent cloud that grows in mass at roughly constant density and turbulence level, until it becomes Jeans unstable, at which point it begins to collapse globally inducing clumpy and filamentary structure, where simultaneously, the turbulent nonlinear density fluctuations induce fast, local collapse events (Vázquez-Semadeni et al., 2007, and references therein). Thus, the turbulence initially produced by the convergent gas flows will have an important role in the subsequent development of the cloud and its star formation activity. These simulations have been developed generally reproducing a frontal shock where several fluctuations are formed. Simulations with oblique shocks (e.g. Fogerty et al., 2016, Fig. 3.1 b), have shown that as the strength of the shock increases, the star formation decreases. The GMCs in this kind of simulations may be formed if the mass of the streaming flows is large enough to reach the required column density for molecule formation $N \sim (1-2) \times 10^{21}\,\mathrm{cm^{-2}}$. At the typical density ($\sim 0.5\,\mathrm{cm^{-3}}$) and velocity dispersion of the WNM ($\sim 10\,\mathrm{km\,s^{-1}}$, Heiles & Troland, 2003), from which we assume the clouds form, the time required to reach this column density is $\sim 10-20$ Myr. Thus, the final clouds would be a mixture of warm and cold gas (Koyama

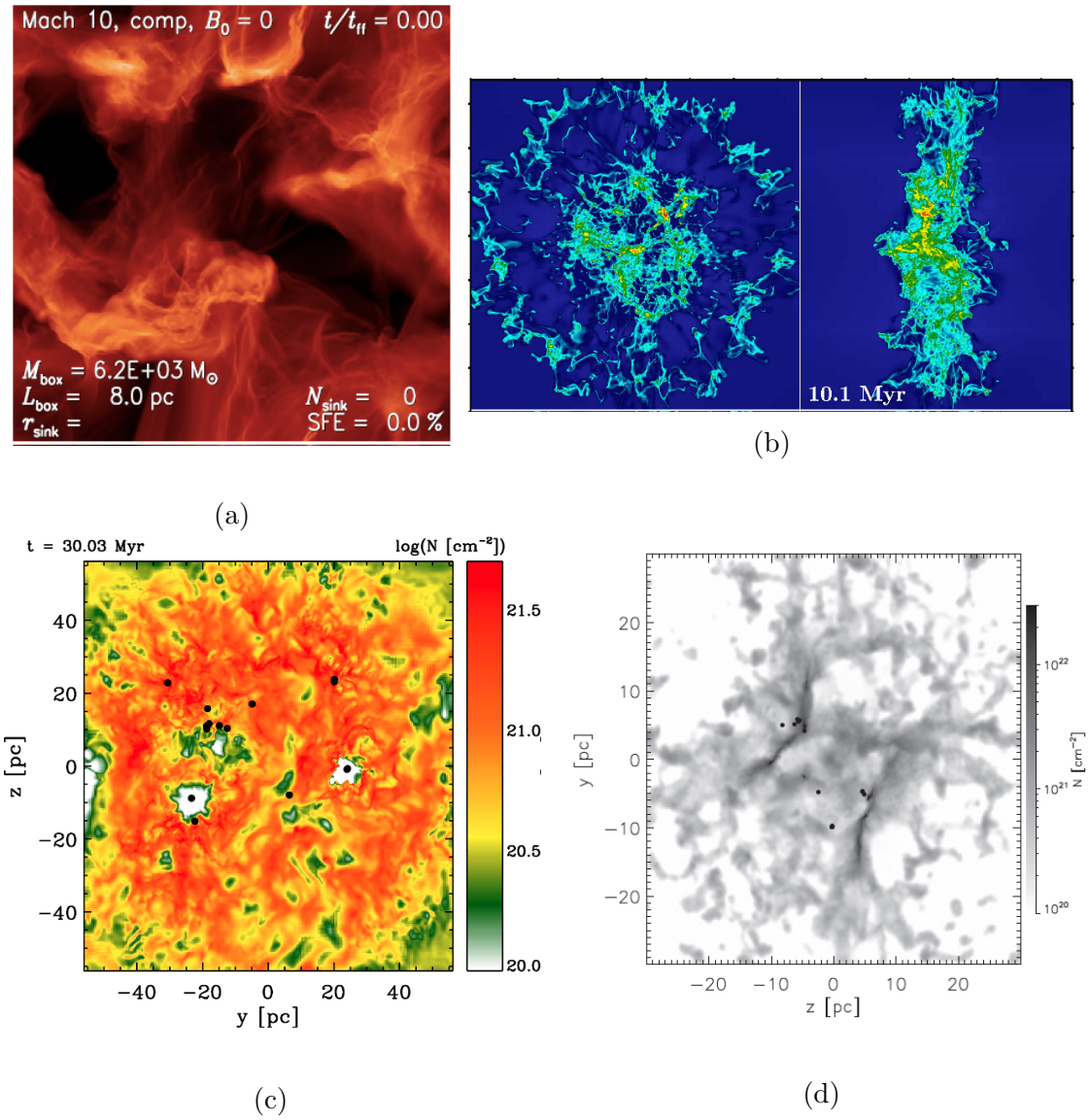

Figure 3.1: a) Turbulence driven simulation (Federrath & Klessen, 2013). b) Face-on and lateral view from a colliding magnetized flow simulation (Fogerty et al., 2016). c) Simulation including stellar feedback Körtgen et al. (2016). d) Face-on view of a colliding flow simulation with self-gravity (Gómez & Vázquez-Semadeni, 2014).

& Inutsuka, 2002; Heitsch et al., 2005; Banerjee et al., 2009; Vázquez-Semadeni et al., 2010; Hennebelle & Inutsuka, 2006). This setup has the important advantage that both the cloud and its internal turbulence develop and evolve self-consistently, rather than being imposed externally by the user.

3.1.3 Simulations including feedback

When stars are born and during their evolution, they contribute to the enrichment of the ISM by the injection of matter and energy through winds, outflows, and in some

cases by supernova explosions. Furthermore, their radiation also contributes to the heating and ionization of their surrounding media. These processes, known as stellar feedback (c.f. Sec.1.2.1) have important effects on the ISM, since they may trigger or reduce star formation, cause the destruction of star forming clouds or support them against collapse, drive turbulence, and induce or prevent fragmentation.

Simulations including these different types of feedback have been developed in order to understand their effects on the star formation process. For example, both analytical calculations and simulations of feedback from stellar objects, like photoionization from massive stars, (e.g. Franco et al., 1994; Hartmann et al., 2001; Matzner, 2002; Nakamura & Li, 2005; Li & Nakamura, 2006) show that this process is probably essential for the energy balance and the possible destruction of the cloud. The simulations also suggest, that in the presence of ionization heating the clouds exhibit SFEs much lower and closer to the observed values, than the case without it (e.g. Peters et al., 2010; Vázquez-Semadeni et al., 2010; Dale et al., 2012; Colín et al., 2013). According to these works, this effect is the result of the evaporation of a fraction of the cloud's mass by the feedback, which in turn, restricts the accretion from the infalling gas. On the other hand, simulations of feedback from supernova explosions (e.g. Körtgen et al., 2016; Padoan et al., 2016; Gatto et al., 2017, Fig. 3.1 c) show that supernovae can be an important regulator of the galactic star formation rate. Simulations using both stellar winds and supernova explosions (e.g. Rogers & Pittard, 2013) show that the SN energy is only weakly coupled to the ambient ISM since the winds have already dispersed the clump significantly. Finally, at cloud core scales, simulations including radiative transfer (thermal emission, radiative shocks, and radiative heating) and magnetic fields (e.g. Commerçon et al., 2011; Bate, 2012; Krumholz et al., 2012; Myers et al., 2013) have shown that in some circumstances, the combination of these forms of feedback reduces fragmentation significantly and at cloud scales, the magnetic field (Zamora-Avilés et al., 2018) increases the star formation rate by reducing the turbulence in the clouds.

3.1.4 Simulations including gravity

Simulations of cloud formation and evolution including self-gravity have also been performed. These studies show that the clouds, rather than remaining globally supported by turbulence, engage in global gravitational contraction (e.g. Burkert & Hartmann, 2004; Hartmann & Burkert, 2007; Vázquez-Semadeni et al., 2007; Heitsch et al., 2008; Banerjee et al., 2009; Vázquez-Semadeni et al., 2009; Vázquez-Semadeni et al., 2011; Carroll-Nellenback et al., 2014).

Burkert & Hartmann (2004) found in 2D simulations of self-gravitating gaseous sheets, that clouds may originate as roughly sheet-like regions of gas driven by large scale flows in the ISM as a result of self-gravity. Then, the supersonic turbulence observed in molecular clouds might be gravitationally generated (Klessen & Hennebelle, 2010). Using 3D MHD simulations, including self-gravity and radiative heating and cooling functions (Vázquez-Semadeni et al., 2007; Banerjee et al., 2009), it has been shown that dense gas structures are formed by transonic compressions in the diffuse atomic medium. This process induces density fluctuations that collapse gravitationally as they approach their Jeans mass, and eventually, the clumps are able to grow in mass and size. Additionally, it is observed that at low magnetization levels the effects of the magnetic fields is negligible (Hennebelle, & Pérault, 2000).

The formation and evolution of filaments has also been studied in MC-formation simulations. It has been shown that filamentary structures are produced self-consistently in simulations of colliding flows due to anisotropic, nearly pressureless gravitational contraction (e.g. Gómez & Vázquez-Semadeni, 2014, Fig.3.1 d). Clarke et al. (2016) have studied the fragmentation of a filament that is accreting instead of being in equilibrium, and Zamora-Avilés et al. (2017) analyze the morphology and kinematics of dense filamentary structures produced in a numerical simulation of a star-forming cloud evolving under their own self-gravity in a magnetized media. More recently Li & Klein (2019), have shown simulations of ideal MHD showing that magnetic fields help forming and reinforcing the filamentary structure in molecular clouds.

3.2 The simulations for the present study

In this thesis we use two numerical simulations that represent the formation and evolution of molecular clouds in the driven turbulence and colliding flows scenarios, including self-gravity. The simulations were first presented in Heiner et al. (2015, RUN03) and (Gómez & Vázquez-Semadeni, 2014, RUN20).

Both runs were performed with the cosmological GADGET-2 code (Springel, 2005). This code follows the dynamics of an ideal gas by means of smoothed particle hydrodynamics (SPH, Monaghan, 1992; Springel et al., 2001), which uses a Lagrangian technique that discretizes mass, using, for example, a set of fluid particles to model the flow. This allows to solve hydrodynamical problems in a simple form, for example, the equations of momentum and energy as a set of ordinary differential equations. Also, GADGET solves self-gravity by means of tree algorithms. (Monaghan, 1992; Springel et al., 2001; Springel, 2005).

The SPH particles in the simulations used in this work have a fixed mass, $m_{\rm SPH}$, different in each setup, and a smoothing length that depends on the number of neighbors (see Sec. 5.2.1); an initial density and temperature, n_0 and T_0 respectively, that were set to be different in each simulation in order to represent different conditions in the ISM. Nevertheless, the initial temperatures were set to the thermal equilibrium value at the chosen densities. In addition to the SPH particles, a prescription for the formation of sink or "stellar" particles (Jappsen et al., 2005) was included. Sink particles represent the formation of stars in order to prevent the timestep from becoming arbitrarily small. Once a set of particles reaches a critical density, n_{sf}, the total mass, momentum, and angular momentum of the SPH particles within the region are computed in order to determine whether they are gravitationally bound. If this is the case, the SPH particles in the region are removed from the gas phase and a point-like "sink particle" is created, inheriting the total mass and momentum of the removed particles. From this moment, the sink particle can continue to accrete SPH particles if they are gravitationally bound to it. The density threshold for sink formation and the accretion radius, in both RUN03 and RUN20 are $n_{sf} = 3.2 \times 10^6\,\mathrm{cm}^{-3}$ and $r_{acc} = 0.04$ pc respectively. The resolution used in the simulations does not allow to resolve single stars or multiple systems; thus, in this work the sinks are in general considered as star clusters rather than isolated stars.

On the other hand, for the heating and cooling, the simulations include a standard cooling function per gas particle (c.f. eq. 1.3) (Dalgarno & McCray, 1972; Koyama & Inutsuka, 2002; Vázquez-Semadeni et al., 2007) of the form

$$\frac{\Lambda(T)}{\Gamma} = \left[10^7 \exp\left(\frac{-1.148\times10^5}{T+10^3}\right) + 1.4\times10^{-2}\sqrt{T}\exp\left(\frac{-92}{T}\right)\right]\mathrm{cm}^{-3}, \qquad (3.1)$$

where T is in kelvins and $\Gamma = 2.0\times10^{-26}\,\mathrm{erg\,s^{-1}}$ is the heating rate, which is applied everywhere in the SPH particle fluid.

The general characteristics of the simulations are described below. Details of the initial conditions are described in Sec. 5.2.1.

3.2.1 RUN03: Driven turbulence simulation

RUN03 (Heiner et al., 2015) is a numerical simulation that models the formation of dense clouds in the turbulent interstellar medium with initial density and temperature ($n = 3\,\mathrm{cm}^{-3}, T = 730$ K) that represent a slightly overdense region in the ISM, as in a spiral arm. At these initial conditions the simulation has $\sim 4\,\mathrm{M_J}$. However,

as it evolves, its density and temperature change such that each fluid parcel tends toward the thermal equilibrium temperature corresponding to its density. The simulation was started by applying a Fourier turbulence driver with purely solenoidal modes and periodic boundary conditions. The inclusion of the heating and cooling functions, given by eq. (3.1), allows the development of the thermal instability that, as the time progresses in the simulation, enhances the density fluctuations from the initial turbulence. Eventually, induced by the gravitational contraction of the density fluctuations, filaments and clumps are formed. Figure 3.2 shows an image from the simulation in the full 3D box, left panel, and a projection on the XY plane, right panel.

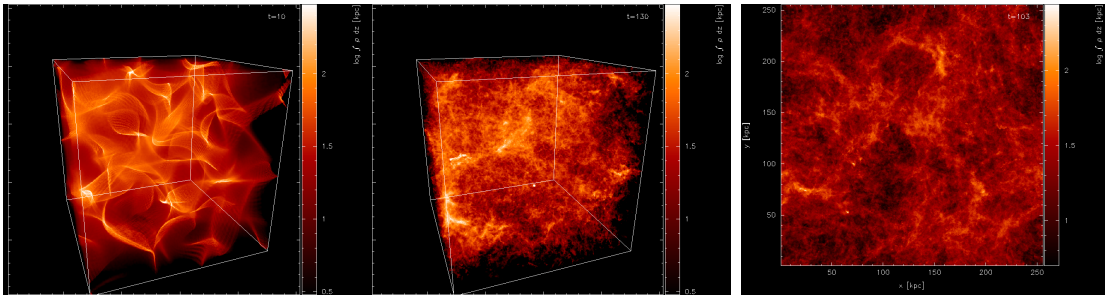

Figure 3.2: RUN03 (Heiner et al., 2015) simulation observed at different evolutionary times. The first image shows the simulation at an early stage, where dense layers due to the initial conditions can be observed. The central image show the complete box and the right panel a projection in the z=128 plane.

This simulation constitutes a model of decaying turbulence in the thermally bistable neutral medium, which produces a clumpy medium where self-gravity causes these clumps to merge and form filamentary dense clouds. The filaments and clumps that collapse from the initial fluctuations accrete gas from the surrounding medium.

3.2.2 RUN20: Colliding flow simulation

RUN20 (Gómez & Vázquez-Semadeni, 2014) describes the collision of two streams of warm gas in opposite directions, which initial density and temperature represent the warm neutral medium ($n = 1$ cm^{-3}, $T = 5206$ K). With these conditions the simulation has an initial mass $M \sim 0.4\,\mathrm{M_J}$. As in RUN03, the Jeans mass later varies in each region according to its own density and temperature. The gas streams in this simulation are represented by two cylindrical regions extending along the x axis within the box, which collide at the central plane creating a dense layer that cools by thermal instability and develops turbulence self-consistently by several thermal instabilities (Heitsch et al., 2006). The cylinders have a mass of $2.64 \times 10^4 M_\odot$ each,

and opposite initial velocities of $v_{inf} = \pm 9.2\,\mathrm{km\,s^{-1}}$[1]. After all the mass in the streams has been incorporated into the dense layer, some material from the ambient is accreted into the layer as well. Thus, the total mass in the cloud is larger than the mass in the inflows, $5.2 \times 10^4\,M_\odot$. In order to break the symmetry of the cylindrical colliding streams, and allow the development of instabilities in the cloud formed by the collision, small-amplitude turbulent motions were added to the gas with an amplitude of $v = 0.17\,\mathrm{km\,s^{-1}}$ in the Fourier space. These motions represent the fact that the ISM is turbulent in general.

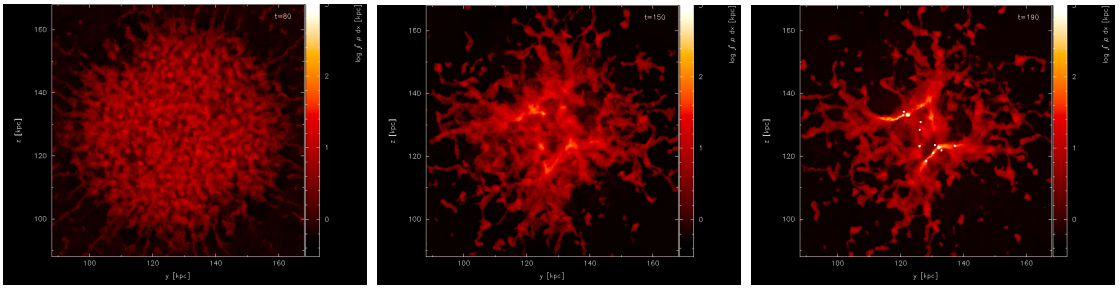

Figure 3.3: Face on view at different times in the evolution from the RUN20 simulation (Gómez & Vázquez-Semadeni, 2014) of colliding flows.

Thus, inside the cloud, hydrodynamical instabilities produce moderately supersonic turbulence, which in turn produces nonlinear density fluctuations. Eventually, they become gravitationally unstable because of the reduction of the average Jeans mass in the cloud due to its contraction, and collapse before the global contraction is completed. Figure 3.3 shows a series of time steps from the simulation. It can be noticed that, additionally to the clumpy appearance, filamentary structure also appears. The filaments are formed by the fragmentation of the dense layer. Inside these elongated structures, clumps are formed, which grow in mass and eventually form sink particles. Later the rest of the filament continues to accrete onto the clumps. Finally, the entire filament-clump system falls into the large-scale potential well at the center of the simulation.

3.2.3 Limitations

Gravitational collapse has been recently proposed as a main driver of the motions in molecular clouds and their substructure (Vázquez-Semadeni et al., 2007, 2009; Vázquez-Semadeni et al., 2019; Ballesteros-Paredes et al., 2011). The simulations studied in this thesis are representative of this scenario. However, throughout this

[1]The velocities of this flows are in accordance with typical velocity in the ISM $\sim 10\,\mathrm{km\,s^{-1}}$.

chapter several mechanisms affecting molecular clouds were mentioned, such as magnetic fields, turbulence and feedback. In RUN03 and RUN20 neither magnetic fields nor stellar feedback are included.

In order to account for the effects of feedback, from photoionizing radiation and supernova explosions principally, a first caveat in these simulations is that, due to the limited mass resolution, the sinks do not reproduce a stellar population. It is not possible to discern between a single star, a multiple system or a cluster. Thus, in general, they are considered as star clusters. Next, the lack of stellar feedback means that star formation is not suppressed once massive stars form, and so eventually the SFR and SFE of the simulations is overestimated. For this reason, in the studies presented below, we often restrict the analysis to clumps where the sink mass has not become much larger than half the gas mass.

Of course, more sophisticated simulations, including a larger number of physical ingredients have been performed, but computational cost increases drastically as the number of included ingredients increases. Thus, to understand the fundamental processes controlling the early stages of star-forming regions, a first step before complex setups is the developing and understanding of simulations with a few ingredients, where recognizing their effects is simple. Then, despite the caveats previously mentioned, we consider that these simulations constitute a sufficient representation of the early stages of the formation and evolution of molecular clouds and their substructure. Here, by "early stages" we refer to star forming regions that do not show clear evidence of having their dynamics affected by feedback.

Chapter 4

Observations of Molecular Clouds

4.1 Observed properties

It is well established that stars are formed within extended regions of high density in the interstellar medium: the molecular clouds.

A molecule can exhibit three main types of transitions: rotational, vibrational, and electronic. For each of these transitions to occur, there is a required minimum energy so that electronic transitions fall in the UV range ($\sim$ 7.5 eV), vibrational transitions in the IR ($\sim$ 0.06 eV), and rotational transitions in the radio range ($\sim$ 4×10^{-4} eV), with corresponding temperatures of $\sim$ 10^4, $\sim$ 600, and 5 K respectively, which are the temperatures needed in order to excite these transitions through collisions (Estalella & Anglada, 1996). The distinct ranges of emission for each transition allow to observe molecular clouds with different techniques.

The natural molecule to be observed would be molecular hydrogen H_2, which is the main component by mass in molecular clouds. However, the properties of this molecule make its direct observation difficult for various reasons. The typical temperature in molecular clouds is 10 K. At this temperature, just the rotational transitions can be excited. Thus, just the molecules with nonzero dipole moment can emit. H_2 is a symmetric molecule with zero dipole moment. Consequently, it cannot emit in purely rotational transitions. Its vibra-rotational transitions can only be excited in shocked regions where temperatures are high (Estalella & Anglada, 1996). Then, to determine the cloud's physical properties, it is necessary to use other molecules that are not homonuclear, by observing their emission and absorption lines, in addition to dust extinction or thermal emission in the IR range. Figure 4.1 shows the range of physical conditions in which various molecular lines can be observed (Tielens, 2005).

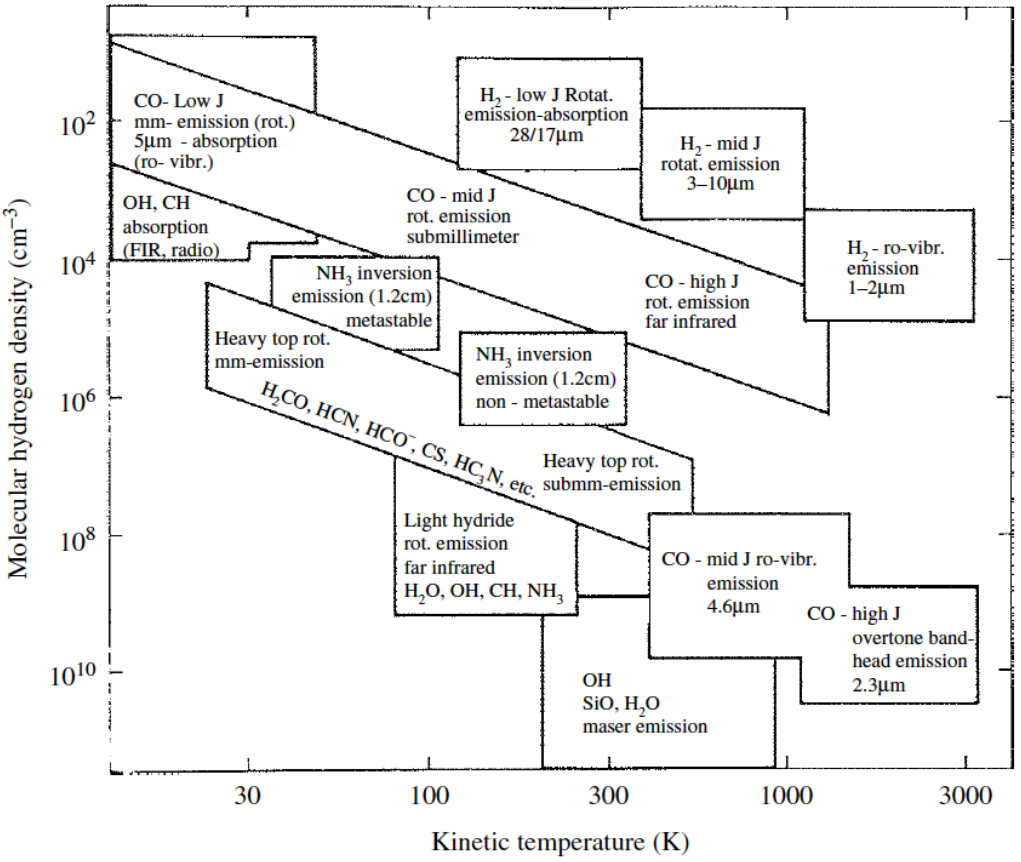

Figure 4.1: Some of the molecules used to study the physical properties of molecular clouds (Tielens, 2005).

After H_2, carbon monoxide (CO) is the most abundant molecule in the ISM. It has low frequency rotational transitions that can be excited at the typical temperatures of molecular clouds $\sim$ 10 K; it is observable at radio wavelengths, even in tenuous molecular gas, and it possesses various observable optically thin isotopologues. These properties allow a good estimation of the total column density of H_2 by means of a conversion factor usually referred to as the "X factor", which is the ratio of H_2 column density to CO intensity (e.g., Dickman, 1978; Dame et al., 2001). Thus, CO surveys have been the primary way to identify giant molecular clouds. Figure 4.2 shows the Milky Way in a velocity-integrated CO map (Dame et al., 2001).

Given that CO lines are optically thick, its isotopologue lines have been used to observe different regions in molecular clouds. Optically thick lines allow to see the outer regions in molecular clouds. In order to observe deeper into the clouds, molecules with transitions with high critical densities are needed. These molecules use to exhibit optically thin lines, which have a minor opacity and allow to observe denser gas, for example, the isotopologues of CO ,^{13}CO and C^{18}O, or molecules like

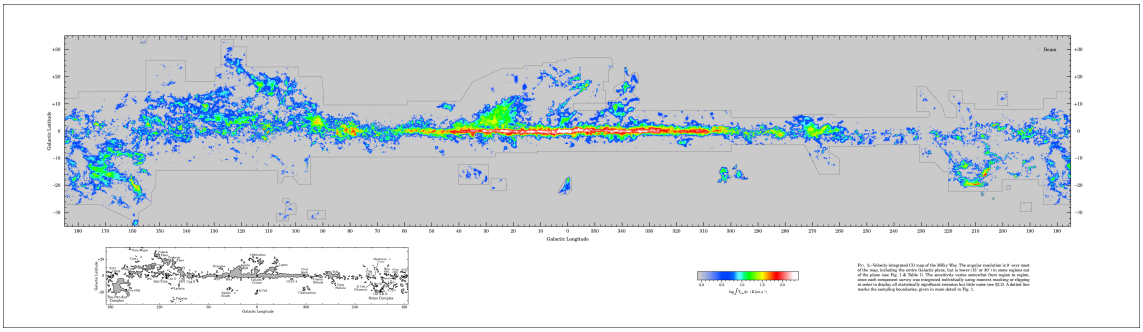

Figure 4.2: Velocity integrated CO map of the Milky Way, Dame et al. (2001).

NH_3, CS, HCO^+, N_2H^+, etcetera. The observations from these and other molecules allow measurement of various gas physical properties at different densities and temperatures.

4.1.1 Analysis tools for observational data

A first step in the derivation of the physical parameters of MCs is the identification of these clouds and their substructure.

Different algorithms have been developed to characterize the nature of molecular clouds, in molecular and atomic line surveys and extinction or emission mapping. These algorithms follow different approaches to identify clumps and, in some cases, select the hierarchical structure even in 2D, 3D data or both. Among the most common algorithms used are:

- GAUSSCLUMPS (Stutzki & Guesten, 1990; Kramer et al., 1998). This algorithm iteratively fits three-dimensional emission line data of Gaussian shaped clumps, from the decomposition of the observed intensity distribution (main-beam brightness temperature versus two spatial coordinates and velocity) to the peak position in the map. Then, it subtracts the fitted clump and fits the next clumps to the residual map or data cube to continue identifying structures.

- CLUMPFIND (Williams et al., 1994). This is a procedure for finding clumps or discrete density enhancements in two- or three-dimensional data. In this algorithm, the structures are selected by first contouring data at different levels. At each level, the isolated contours are defined as clumps. Then, at lower levels, if contours are blended, they are separated by a friends of friends algorithm, precluding finding overlapping objects. If they are isolated, they are considered as a new structure. Then, clumps are defined as contours containing a single maximum.

- DENDROGRAMS (Rosolowsky et al., 2008). This is an algorithm that represents the changing topology of isosurfaces as a function of contour levels, i.e., how the number of structures changes at distinct levels, either increasing (when new isosurfaces appear) or decreasing (if already defined structures mixed), in three-dimensional molecular line data cubes or 2D images. This algorithm tracks the hierarchical structure based on the structure trees (Houlahan & Scalo, 1992) determining whether an object combines with a distinct contiguous structure. Thus, this algorithm classifies structures in leaves and branches to the root, defining physical relationships between the different catalogued objects.

- SCIMES (Colombo et al., 2015). More recently, this algorithm to identify giant molecular clouds based on dendrograms and clustering analysis. The cluster analysis allows classification of data into groups based on similarity criteria. This algorithm can be applied to PPV data cubes, position-position-position simulations or position-position images.

These and other algorithms have been used not only in observational data but also to analyze numerical simulations.

In this thesis we study the substructure of an infrared dark cloud. To do this, we compute the main physical parameters identifying the substructure with the `dendrogram` algorithm. This algorithm works by constructing a tree, where the bottom level represents the lower density gas. The brightest pixels in the data cube are identified and progressively fainter pixels are added, these local maxima are considered the leaves of the tree. Then, the pixel with the next larger value is taken and the algorithm decides whether to add it to an existing structure or to create a new one, which will happen if its value is greater than its immediate neighbors. The identified structures keep growing until a pixel adjacent to two structures is found, in this case, they are merged into a branch. The branches can grow while more structures are found. These structures can be merged to new branches to finally end up in a tree. In order to account for the noise, a minimum value (`min_value`) above the noise σ, is set in the dendrogram, so any structure peaking below this minimum is excluded. To avoid maxima identified because of noise, a minimum relative height (`min_delta`) is required for a structure to be considered. Thus, once the height exceeds the minimum, the structure is considered as part of the tree. Both `min_value` and `min_delta` are function of the rms noise. Finally, a minimum number of pixels (`min_pix`) is considered for the structures in order to be considered as real

objects. The `dendrogram` allow to compute some parameters for these structures, like the major and minor axis of the projection on the position-position plane, the radius, and the mean position in the x and y directions. The one we consider for this study is the radius. This is computed as the geometric mean of the major and minor axes of the projection onto the position-position plane for each structure.

In addition to the IRDC, we also analyze the published data from a different cloud, for which the properties of its internal structure have already been reported and, from numerical simulations, we study the formation and evolution of molecular clouds and their substructure. For the later case, we use a different algorithm to identified structure, it is described in Sec. 5.2.2.1. It works similarly to the dendrograms algorithm. As dendrograms, our algorithm works by selecting objects at different isosurfaces or thresholds. However, in our case, the thresholds are defined arbitrarily instead of being defined by the merged level between structures as in dendrograms.

4.1.2 Physical properties in molecular clouds

Even though there are advantages and disadvantages in all of the methods described before, they have allow to avoid the arbitrary eye analysis made in the past. By the use of these and other techniques, molecular clouds and their substructure have been identified and their physical properties have been derived.

In particular, molecular-line observations provide information about the gas component of clouds and their substructure, size, velocity linewidth, density, temperature, and chemical composition (Rosolowsky & Leroy, 2006; Bergin & Tafalla, 2007). Additionally, dust emission and absorption can give information about the structure of molecular clouds since the dust density and mass are correlated with the H_2 properties. The physical properties derived with all these data allow understanding the formation and evolution of clouds.

An important parameter for cloud description is the temperature, either rotational, kinetic or of excitation ($T_{\rm rot}$, $T_{\rm k}$, and $T_{\rm ex}$ respectively). To measure the temperature of the gas component in clouds, clumps, and cores, the excitation level of simple molecules is commonly used (Evans, 1999). The excitation temperature can be derived from the radiative transport equation in the optically thick case (e.g., CO) or, using molecular lines, from the ratio of the populations in different energy levels (e.g., in molecules such as NH_3 or CH_3CN) (Estalella & Anglada, 1996). The hyperfine structure of NH_3, for example, has transitions close in frequency, but from well separated levels. These properties are ideal for accurate measurements (Thad-

deus, 1977). When the observed lines are in local thermodynamic equilibrium, $T_{\rm ex}$ is related directly to $T_{\rm K}$; thus, it is generally assumed that $T_{\rm ex} = T_{\rm K}$. The kinetic temperature, in addition to kinematic information, like the velocity of clouds, is an important parameter of the state of the clouds.

Thermal and non-thermal motions are present in molecular clouds. For the determination of these motions, saturated lines are avoided, as they need to be optically thin and strong enough for a precise velocity measurement. Thus, the observations of molecular lines can give estimates of these velocities. Line spectra gives information about the radial component (along the line of sight), i.e., the radial velocity $V_{\rm lsr}$, which in turn has two components, the centroid velocity (usually referred to as the first-moment) and the velocity dispersion (the second-moment). These velocities are representative of the motions inside the cloud, they can be identified in the spectra as the peak velocity and the line width or FWHM, see Fig. 4.3.

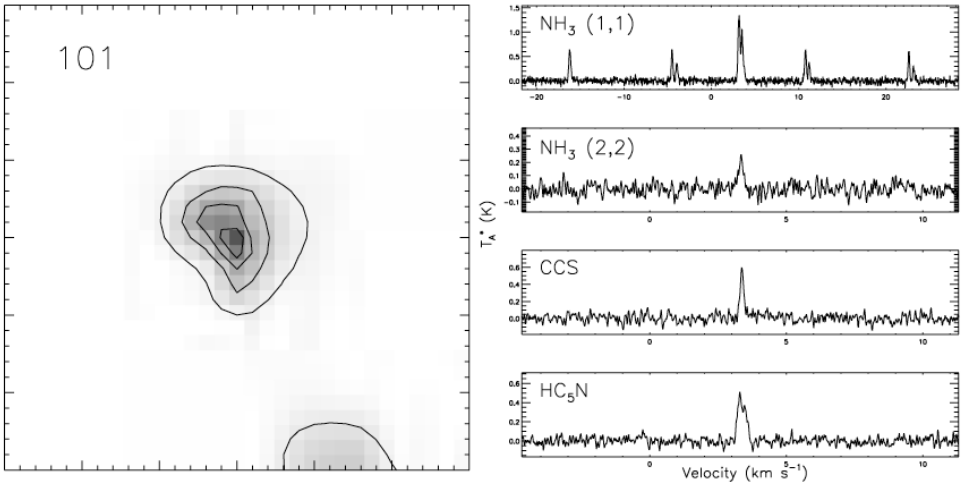

Figure 4.3: Extinction image (left) and spectra (right) of different molecular lines observed in a dense core in the Pipe Nebula (Rathborne et al., 2008).

The emission from molecules can also be converted into a molecular column density by different methods. For a given spectral line, for example, the derived column density will depend on the relation between the source size and the telescope beam size. If the source is resolved, i.e., the source size is larger than the beam size, the molecular column density will be "source-averaged". Otherwise, it is called "beam-averaged". In the latter case, the measured column density would be a lower limit given that the spatial extent of the emission will be averaged over the beam (Rohlfs, & Wilson, 1996). The total column density is obtained by assuming an abundance of the tracer molecule relative to H_2.

As mentioned before, the CO molecule allows a good measurement of the total column density due to its high line intensity (usually expressed as an integrated brightness temperature), low critical density, excitation close to local thermodynamic equilibrium (LTE), and its large abundance relative to H_2 (10^{-4}) (Rohlfs, & Wilson, 1996). However, this abundance exhibits large fluctuations, reflected on the X factor, which, according to Barnes et al. (2016), rather than be constant, it varies with the excitation temperature. An additional way to derive N_{H_2} is by dust observations. The dust-to-gas ratio is approximately constant in the ISM. Then, from the column density of dust the column density of gas can be obtained (Rohlfs, & Wilson, 1996). This method depends on the visual extinction, A_V, for which there are well known relations (c.f., Sec. 1.2.1). On the other hand, if volume density needs to be determined, additional assumptions must be made (such as the thickness of the molecular cloud in the line of sight).

For mass determination there are also different techniques. As with the column density, mass can be derived from molecular lines, mainly optically thin, or by dust measurements. Traditionally, even though CO is optically thick, by summing the CO intensities over the velocity channels and assuming the emission in each channel is optically thin, the mass of the clouds can be obtained (Rohlfs, & Wilson, 1996; Tielens, 2005). However, more recently Barnes et al. (2018) and Pitts et al. (2019) have found that the CO abundance is variable even in a single region. Thus, velocity channels in CO observations are also optically thick, in which case the total mass of the clouds cannot be estimated. Once the column density is determined, another possibility to calculate the mass of an object is simply by assuming a geometry and compute the mass corresponding to the column density in that object. Additionally, assuming a gas-to-dust ratio, the mass in dust, which can be measured directly from observations, can be converted into a gas mass (Galván-Madrid et al., 2013).

GMCs, and their substructure, are often asymmetrical and have poorly defined boundaries. Thus, another particular difficulty, is the determination of the cloud radius. Many approaches have been made in order to determine the size of a cloud. For example, it has been inferred based on the area of identified clouds (e.g. Williams et al., 1994), or the mean of the deconvolved FWHMs of the emission distribution along two perpendicular directions (e.g. Wilson & Scoville, 1990). All these measurements, the mass and column density for example, can be affected by uncertainties in the molecule abundance and the distance to the cloud.

Even from the time of the first molecular line observations, different theories have been developed assuming some characteristics of MCs that nowadays have changed interpretation. In the next section we quote some of them.

4.2 Molecular cloud models derived from observations

CO observations have revealed a vast collection of giant molecular clouds in our Galaxy. As mentioned in the previous section, this molecule just allows the identification of extended structure at low densities, given that it is optically thick. Fortunately, molecules different than CO (and its own isotopologues), which are optically thin, as well as dust observations, allow to go deeper into the clouds making possible to observe structures at higher densities, $n > 10^3\,\mathrm{cm}^{-3}$. From these data, the presence of hierarchical structure, observed with increasing spatial resolution, has been recognized as a common feature of molecular clouds. Thus, thanks to the diversity of data, it has been possible to study the process of star formation at different scales, densities and temperatures.

Analytical and numerical models have been developed in order to explain the observed properties of molecular clouds, see discussion in Chap. 2. Among these properties, one of the observed features that set a benchmark in the understanding of molecular clouds was the broadening of molecular-lines (Wilson et al., 1970). Observations showed the presence of non-gaussian line shapes and velocity differences across clouds of $\sim 1\,\mathrm{km\,s}^{-1}$ or more (at $T = 30$ K the rms thermal velocity of CO is 0.16 $\mathrm{km\,s}^{-1}$). Different interpretations were proposed to explain these large velocities. Since then, the discussion of whether the dominant motions are due to collapse, rotation, small- or large-scale random motions, or even a combination of some of them, continues.

The most frequent explanations of the line broadenings have been the collapse and the support models, see Sec. 2.3.1. Concerning the first model, in the early 1900's, Jeans (1902) showed that initially uniform clouds could be supported against gravitational collapse by thermal pressure up to a critical size scale, or mass (Sec. 1.3.3). This is now known as the Jeans criterion. In this context, the line broadening was interpreted as the result of the clouds being in a state of collapse with the linewidths being the result of the collapsing motions (Goldreich & Kwan, 1974). However, molecular cloud observations seemed to be inconsistent with the idea of the gas being driven by gravitational collapse, given that the star formation rate was lower than the prediction of this model and that no signatures of collapse were observed in molecular clouds (Zuckerman & Evans, 1974). Instead, they argued that clouds could not be collapsing but they have to be supported and that the linewidths corresponded to supersonic turbulent motions.

The support model has two variants, the magnetic (Shu et al., 1987) and the turbulent (Zuckerman & Evans, 1974; Zuckerman & Palmer, 1974; Mac Low & Klessen, 2004) support scenarios. In these models, either magnetic fields or small-scale turbulence provide support against collapse resulting in clouds with low star formation activity. Nevertheless, recent observations of magnetic fields have suggested that magnetic fields in molecular clouds are not strong enough to support them (Crutcher, 2012). Instead, from the 2000's, the turbulent support model has been the most accepted. In this scenario, the irregular supersonic motions were interpreted as the result of turbulent motions (Zuckerman & Palmer, 1974; Larson, 1979, 1981), from the largest to the smallest scales, thus supporting the clouds and their substructures against their self-gravity. The "turbulent nature" inferred from observations was recognized as the main property of molecular clouds and their substructure (Vázquez-Semadeni et al., 2000; Mac Low & Klessen, 2004; Ballesteros-Paredes et al., 2007).

Other features observed in molecular clouds that were explained by the turbulent support model, were the Larson scaling relations (Larson, 1981). As discussed in Sec. 2.2, these relations were interpreted as molecular clouds being bound objects in virial equilibrium and with roughly constant column density. In this picture, the virial equilibrium is the result of the kinetic turbulent energy counteracting the gravitational collapse. The improvement in observational samples however, has shown that these scaling relations are not valid for either the subsrtucture in molecular clouds or the clouds themselves (see discussion in Sec. 2.2.2 and Sec. 2.3). New data show that clouds are incompatible with Larson's scaling relations (Heyer et al., 2009; Field et al., 2011; Leroy et al., 2015). Instead, these relations seem to be a spacial case of a more general relation (c.f., eq.(2.4), Sec. 2.2.2), which can be explained by means of gravitational collapse (Ballesteros-Paredes et al., 2011; Camacho et al., 2016; Ballesteros-Paredes et al., 2018). Thus, the gravitational collapse model (Goldreich & Kwan, 1974) has emerged again (e.g. Vázquez-Semadeni et al., 2007; Heitsch et al., 2008; Vázquez-Semadeni et al., 2009; Vázquez-Semadeni et al., 2019).

In the next two chapters, the analysis of molecular clouds in numerical simulations, supporting the gravitational hierarchical collapse model in an evolutionary context, is presented. The results shown here are consistent with the observed properties of molecular clouds.

Chapter 5

Energy budget of forming clumps in numerical simulations of collapsing clouds

We analyze the physical properties and energy balance of density enhancements in two SPH simulations of the formation, evolution, and collapse of giant molecular clouds[1]. In the simulations, no feedback is included, so all motions are due either to the initial, decaying turbulence, or to gravitational contraction. We define clumps as connected regions above a series of density thresholds. The resulting full set of clumps follows the generalized energy-equipartition relation $\sigma_v/R^{1/2} \propto \Sigma^{1/2}$, to which we refer as the generalized Larson scaling relation, where σ_v is the velocity dispersion, R is the "radius", and Σ is the column density. We interpret this as a natural consequence of gravitational contraction at all scales, rather than virial equilibrium. Nevertheless, clumps with low Σ tend to show a large scatter around equipartition. In more than half of the cases, this scatter is dominated by external turbulent compressions that *assemble* the clumps, rather than by small-scale random motions that would disperse them. The other half does actually disperse. Moreover, clump sub-samples selected by means of different criteria exhibit different scalings. Sub-samples with narrow Σ ranges follow Larson-like relations, although characterized by their respective value of Σ. Finally, we find that: i) clumps lying in filaments tend to appear sub-virial; ii) high-density cores ($n \geq 10^5$ cm^3) that exhibit moderate kinetic energy excesses often contain sink ("stellar") particles, and the excess disappears when the stellar mass is taken into account in the energy balance;

[1]The present chapter has been published in the Astrophysical Journal (doi:10.3847/1538-4357/833/1/113). Here we present the original version with modified notation in order to make it consistent with the thesis.

iii) cores with kinetic energy excess but no stellar particles are truly in a state of dispersal.

5.1 Introduction

Ever since the pioneering work of Larson (1981) it has been recognized that molecular clouds (MCs) obey scaling relationships, that have been interpreted as representative of approximate virial equilibrium in the clouds between their internal "turbulent" motions and their self-gravity. Subsequently, however, there have been suggestions that these relations may actually be the result of observational selection effects (e.g., Kegel, 1989; Scalo, 1990). In addition, there have been attempts at generalization of these relations (e.g., Keto & Myers, 1986; Heyer et al., 2009) and reinterpretations in terms of global cloud collapse rather than virialization (Ballesteros-Paredes et al., 2011, hereafter B11). Moreover, there are structures that are observed to possess kinetic energies in excess of those that would be consistent with equilibrium (or more generally, energy equipartition).

In this chapter we aim to investigate whether clumps forming in numerical simulations of clouds undergoing global gravitational contraction exhibit similar properties as those in observational surveys such as Larson scaling relations, and search for a cause of the apparent kinetic energy excesses seen in some subsets of clumps in observational samples.

5.1.1 Larson's relations and their generalization

For over three decades, it has been accepted that molecular clouds (MCs) satisfy the so-called Larson (1981) scaling relations between velocity dispersion ($\sigma_{\rm v}$), mean number density ($\langle n \rangle$) and size (L). In their presently accepted form, these relations are (e.g., Solomon et al., 1987; Heyer & Brunt, 2004)

$$\langle n \rangle \approx 3400 \left(\frac{L}{1\,\mathrm{pc}} \right)^{-1} \mathrm{cm}^{-3}, \tag{5.1}$$

and

$$\sigma_{\rm v} \approx 1 \left(\frac{L}{1\,\mathrm{pc}} \right)^{1/2} \mathrm{km\,s}^{-1}. \tag{5.2}$$

Larson (1981) additionally showed that these relations implied that the velocity dispersion is close to the value corresponding to virial equilibrium. In what follows, we will more generally refer to this as "near equipartition" between the nonthermal

kinetic and the gravitational energies. Also, it should be remarked that eq. (5.1) implies that the column density of the clouds, $\Sigma = \int_{\rm LOS} \rho d\ell$ is approximately the same for MCs of all sizes. In this expression, ℓ is the length element, and the integration is performed along the line-of-sight (LOS) through the cloud.

However, the validity of Larson's relations has been questioned by various authors. Kegel (1989) and Scalo (1990) argued that the apparent constancy of the column density may arise from selection effects caused by the need to exceed a certain minimum column density in order to detect the clouds, and by a maximum apparent column density caused by line saturation (optical thickening). This possibility was in fact recognized by Larson (1981) himself. Some time later, Ballesteros-Paredes & Mac Low (2002) showed that, in numerical simulations of turbulent clouds, clumps defined by means of a column density threshold exhibited a Larson-like density-size relation, but clumps defined by means of a *volume* density threshold did not.

Several years later, using the Boston University-FCRAO Galactic Ring Survey (Jackson et al., 2006), Heyer et al. (2009, hereafter H09) re-analyzed the giant molecular cloud (GMC) sample of Solomon et al. (1987). The higher angular sampling rate and resolution available to H09, as well as the use of the ^{13}CO $J = 1$–0 line allowed them to obtain a much larger dynamic range in column density than that available to Solomon et al. (1987). Moreover, H09 considered two different definitions for the cloud boundaries, thus effectively obtaining two different MC samples.[2] With this procedure, the GMC sample of H09 spanned over two orders of magnitude in column density, making it clear that column density is *not* constant for GMCs (see also Heyer et al., 2001). Nevertheless, H09 noted that, in spite of the non-constancy of the column density, the GMCs are still consistent with virial equilibrium. They showed this by noting that their GMC sample satisfied

$$\frac{\sigma_{\rm v}}{R^{1/2}} \approx \left(\frac{\pi G \Sigma}{5}\right)^{1/2} . \tag{5.3}$$

When the column density is not constant, this relationship corresponds to virial equilibrium; i.e., to $|{\rm E_g}| = 2{\rm E_k}$, with $\rm E_k$ being the nonthermal kinetic energy and $\rm E_g$ being the gravitational energy for a spherical cloud of uniform density and radius R. Thus, eq. (5.3) can be considered as the generalization of Larson's relations when Σ is not constant.

[2]Contrary to some claims in the literature, these two definitions of the cloud boundaries do amount to *two* different MC samples, as the masses and velocity dispersions were measured for each cloud within each of the two boundaries. Thus, the 'A2' clouds in H09 constitute a sample of smaller, denser objects within the 'A1' sample, just like dense clumps and cores are substructures of their parent MCs, with independent dynamical indicators.

Shortly thereafter, Lombardi et al. (2010) claimed that the column density of GMCs is constant after all. Using near-infrared excess techniques, these authors argued that the mean GMC column density in their sample remained constant in spite of being sensitive to very low extinctions, thus suggesting that the minimum-column density imposed by a sensitivity threshold was not an issue. However, it has subsequently been recognized that this effect is natural for clouds with a Σ probability density function (PDF) that peaks at some value and drops fast enough at lower column densities (Beaumont et al., 2012; Ballesteros-Paredes et al., 2012). The lack of pixels at low Σ implies that the dominant apparent column density will be that of the peak, and it is now recognized that the presence of a peak may be an artifact of incomplete sampling at low column densities (Lombardi et al., 2015). Moreover, recent observational studies have shown evidence on the non-constancy of Σ in our Galaxy (Barnes et al., 2018; Pitts et al., 2019). Therefore, at present there is no compelling evidence for the validity of the density-size relation (eq. 5.1) for GMCs nor their substructures in general (see also Barnes et al., 2011).

On the other hand, the velocity dispersion-size relation,[3] expression (5.2) above, has often been interpreted as the signature of supersonic turbulence, with an energy spectrum $E(k) \propto k^{-2}$, where k is the wavenumber. Indeed, the velocity variance, interpreted as the average turbulent kinetic energy per unit mass in scales of size $\ell \leq 2\pi/k$, given by $\sigma_{\rm v}^2(\ell) = \int_{k>2\pi/\ell} E(k)dk$, scales as $\ell^{1/2}$ (e.g. Vázquez-Semadeni et al., 2000; Elmegreen & Scalo, 2004; McKee & Ostriker, 2007). In this case, the velocity dispersion- size relation would have a completely independent origin from that of the density-size relation, and the reason for the observed near- equipartition between the gravitational and turbulent kinetic energies would require a separate explanation. However, massive star-forming clumps notoriously do not conform to the $\sigma_{\rm v}$-L relation (e.g., Caselli & Myers, 1995; Plume et al., 1997; Shirley et al., 2003; Gibson et al., 2009; Wu et al., 2010), a situation that appears inconsistent with a universal turbulent energy cascade spanning the whole range from the scale of GMCs down to the scale of massive clumps.

An alternative interpretation was suggested by BP11, who proposed that the origin of the $\sigma_{\rm v}$-L relation was not turbulence, but rather gravitational contraction of the clouds, combined with the observational selection effect of a restricted column density range. This possibility was actually suggested over four decades ago by Goldreich & Kwan (1974). Similarly, Liszt et al. (1974) suggested that their line profiles and LOS-velocity maps of the Orion MC were consistent with extended radial motions, although they could not discriminate between expansion and col-

[3] In what follows, we will refer to this relation as the linewidth-size relation as well.

lapse. However, the extended-motion scenario was soon dismissed by Zuckerman & Palmer (1974), who argued that, if that were the case, then the star formation rate in MCs should be much larger than observed, and that systematic shifts between emission lines produced by HII regions at the centers of the clouds and absorption lines produced in the radially- moving cloud envelopes should be observed, but they are not. Zuckerman & Evans (1974) then proposed that the observed linewidths corresponded to supersonic, small-scale turbulence.

The small-scale turbulence scenario, however, suffers from a number of problems (see Vázquez-Semadeni, 2015, for a detailed discussion). Instead, B11 have suggested a return to the scenario of gravitational collapse at the scale of the whole GMCs, with the problem of an excessive SFR being solved by early destruction of the clouds by stellar feedback (Vázquez-Semadeni et al., 2010; Zamora-Avilés et al., 2012; Dale et al., 2012; Colín et al., 2013; Zamora-Avilés & Vázquez-Semadeni, 2014). B11 noted that the generalized Larson relation, eq. (5.3) is not only satisfied by GMCs, but also by massive clumps that do not satisfy Larson's velocity dispersion-size relation, eq. (5.2).

Thus, B11 interpreted the near-equipartition as evidence for free-fall in the clouds (see also Traficante et al., 2015) rather than near-virial equilibrium, noting that the virial and free-fall velocities differ only by a factor of $\sqrt{2}$. Indeed, for a freely collapsing cloud, defining the total energy as zero, the nonthermal kinetic energy and the gravitational energy satisfy $\mathrm{E_k} = |\mathrm{E_g}|$, so that, instead of eq. (5.3), we have

$$\frac{\sigma_\mathrm{v}}{R^{1/2}} \approx \left(\frac{2\pi G\Sigma}{5}\right)^{1/2}. \tag{5.4}$$

Generally, the observational errors and uncertainties in cloud and clump surveys are larger than this slight $\sqrt{2}$ factor, so that, for all practical purposes, *any evidence in favor of virial equilibrium based on energetics of the clouds can just as well be interpreted as evidence in favor of free collapse.* Recent observational studies have shown signatures of infall motions in line profiles along filaments and massive clumps in the Cygnus X region (Schneider et al., 2010), in massive star-forming cores of the infrared dark cloud SDC335.579-0.272 (Peretto et al., 2013), in massive starless cores (Traficante et al., 2015), and massive clumps (Barnes et al., 2018), supporting the notion that these systems are consistent with a global gravitational collapse. Moreover, Traficante et al. (2015) introduce an equivalent analysis as in H09 to demonstrate that most of the non-thermal motions in their sample originate from self-gravity.

5.1.2 Deviations from energy equipartition

An additional important feature in the GMC sample studied by H09 is that the clouds tended to lie systematically *above* the virial-equilibrium line in a plot of $\sigma_{\rm v}/R^{1/2}$ *vs.* Σ, a plot that we refer to the $\mathcal{L}\,vs.\,\Sigma$ diagram, where $\mathcal{L}=\sigma_{\rm v}/R^{1/2}$. This feature has received different interpretations by different authors. H09 themselves interpreted it simply as a systematic underestimation of the cloud masses, due to the various assumptions they used in determining the masses from ^{13}CO emission. On the other hand, Dobbs et al. (2011) have interpreted this feature as evidence that most of the GMCs are gravitationally unbound, probably because they form by cloud-cloud collisions, which feed a large velocity dispersion that unbinds the GMCs. Keto & Myers (1986) and Field et al. (2011), instead, have assumed that the clouds are gravitationally unbound, but confined by an external pressure, while B11 suggested that the GMCs are actually collapsing, and that, at face value, the H09 data are slightly more consistent with free-fall than with virial equilibrium, since the free-fall velocity is slightly larger than the virial one.

In addition to the slight systematic supervirial nature of cloud surveys, in several observational clump and core surveys, some objects appear to be *strongly* supervirial, exhibiting values of the *virial parameter*, $\alpha\equiv 5\sigma_{\rm v}^2R/GM\sim 10$–$100$ (see,e.g., fig. 1 and fig. 16 in Barnes et al., 2011; Kauffmann et al., 2013), although the first authors corrected their results later (Barnes et al., 2016), especially in the case of low-mass objects. These objects are traditionally interpreted as having a kinetic energy significantly larger than their gravitational energy, perhaps due to driving by stellar feedback, and therefore requiring confinement by external pressure to prevent them from dispersing, as in the interpretation by Field et al. (2011) of the H09 sample. However, if we adopt the interpretation that star-forming GMCs are undergoing global and hierarchical collapse, pressure confinement is not satisfactory, since in this scenario the clumps should be gravitationally-dominated as well. Investigating the origin of these kinetic energy excesses within the scenario of collapsing clouds is one of the goals of this chapter.

5.1.3 This work

In this work we create an ensemble of clumps in simulations of the formation and evolution of molecular clouds, in order to investigate their energy balance under a scenario of initial turbulence and subsequent gravitational collapse. Our simulations, of course, have a number of limitations, which are discussed in more detail in Sec. 5.4.1, but here we note that they neglect magnetic fields, stellar feedback, and have

relatively low masses that restrict the clumps and cores we obtain to values typical of low-mass star-forming regions, which form low-mass stellar groups or low-mass clusters. Nevertheless, we expect that the results we obtain can be extrapolated to regions of larger masses.

The organization of the chapter is as follows. In Sec. 5.2.1 we briefly describe the simulations, and in Sec. 5.2.2, we describe the clump-finding algorithm used to define clumps at various values of volume density, $n_{\rm th}$, as well as the selection criteria we used in order to avoid considering unrealistic clumps (i.e. those that would be affected by stellar feedback in reality). Next, in Sec. 5.3, we present our results on the energetics of the clumps and cores and their implications on Larson's relations. In Sec. 5.4 we discuss our work in context with recent related numerical studies, as well as the range of applicability, possible extrapolations, and limitations of our study. Finally, in Sec. 5.5 we present a summary and some conclusions.

5.2 Numerical data and analysis

5.2.1 The simulations

The simulations used in this work are those presented in Gómez & Vázquez-Semadeni (2014) and Heiner et al. (2015). For historical reasons, we refer to these simulations as RUN20 and RUN03, respectively. Both simulations were performed with the code Gadget-2 (Springel et al., 2001), using $296^3 \approx 2.6 \times 10^7$ SPH particles and a numerical box of 256 pc per side. Each SPH particle is characterized by a single mass and a smoothing length, the latter defined as the radius of the volume that contains 40 ± 5 neighboring particles. The simulations include the prescription for the formation of sink particles by Jappsen et al. (2005), and the fix proposed by Abel (2011), which eliminates several unphysical effects that arise in the standard SPH prescription, and describes more accurately a number of physical instabilities, such as the Kelvin-Helmholz and Rayleigh-Taylor instabilities. Both simulations used the cooling and heating functions of Koyama & Inutsuka (2002), corrected for typographical errors as described in Vázquez-Semadeni et al. (2007). Details on the sink particle prescription and the cooling function are described in Sec. 3.2.

In RUN20, the (uniform) initial density and temperature were set at $1\,{\rm cm}^{-3}$ and 5206 K, and the mass per SPH particle is $\approx 0.02\ M_\odot$ so that the total mass in the box is $5.26 \times 10^5 M_\odot$. In this simulation, two cylindrical streams of warm neutral atomic gas, of diameter 64 pc and length 112 pc, were set to collide at the central ($x = 0$) plane. In addition, a small amount of turbulent energy was added (with

speeds $\sim$ 10% of the collision speed), at wave numbers k = 8-16 $\times$ $2\pi/L$, where L is the box size, so that the perturbations are applied at scales smaller than the inflow diameter. The collision produces a turbulent cloud, which grows in mass until it becomes gravitationally unstable and begins to collapse (e.g., Vázquez-Semadeni et al., 2007; Heitsch et al., 2008). The collapse, however, is irregular and chaotic, because of the turbulence in the cloud, which creates a multi-scale and multi-site chaotic collapse (Heitsch et al., 2008; Vázquez-Semadeni et al., 2009), rather than a monolithic one, producing a complex morphology, in which filamentary structures arise self-consistently. We refer the reader to Gómez & Vázquez-Semadeni (2014) for more details.

On the other hand, RUN03 was produced with the aim of avoiding the over-idealized conditions of a colliding-flow simulation, in which the flows are perfect cylinders with circular cross-sections, moving in opposite directions along the same axis. Instead, RUN03 was started by applying a Fourier turbulence driver with purely solenoidal modes, with wave numbers in the range $1 < kL/2\pi < 4$ over the first 0.65 Myr of the simulation, reaching a maximum velocity dispersion of $\sigma \approx 18$ km s^{-1}. This produces a complex network of sheets and filaments, which subsequently grow by gravitational accretion. In this simulation, the initial density and temperature were set at 3 cm^{-3} and 730 K, respectively, the total mass in the box was $1.58 \times 10^6 M_\odot$, and the mass per SPH particle was $\approx 0.06\ M_\odot$.

Finally, in both simulations, the density threshold to form sink particles is set at 3.2×10^6 cm^{-3}, and no prescription for feedback is included. This implies that we must be careful in the choice of the clumps to be analyzed, in order to avoid including clumps that would have already been destroyed by stellar feedback, had it been included (see Sec. 5.2.2). The main parameters of the simulations are summarized in Table 5.1.

	L [pc]	T_0[K]	n_0[cm^{-3}]	$m_{\rm sph}$ [$M_\odot$]	M$_{\rm box}$ [$M_\odot$]	Type
RUN03	256	730	3	0.06	1.5×10^6	Decaying turbulence
RUN20	256	5206	1	0.02	5×10^5	Colliding flows

Table 5.1: Initial conditions in simulations. L is the box size, $m_{\rm sph}$ is the mass per SPH particle, T_0 is the initial temperature, and n_0 is the initial density.

In these simulations, we analyze the physical properties of the clumps formed self-consistently, using a clump finding algorithm that we describe in Sec. 5.2.2. We then measure the mass, size, density and velocity dispersion of the clumps in physical space (not projected), to investigate their energy balance. Table 5.2

gives the velocity dispersion, mass in sinks and global star formation efficiency, SFE $= M_*/(M_* + M_{\rm cold})$, of the simulations at the chosen times. Here, $M_{\rm cold}$ is the total mass in cold gas ($n > 50$ cm^{-3}, T$\sim$10-20 K).

	t (Myr)	σ_v (km/s)	M$_{sink}$ (M$_\odot$)	SFE
	15.6	4.15	83.8	0.0002
	18.2	3.69	512.9	0.0012
RUN03	18.5	3.65	576.9	0.0013
	19.5	3.50	1300.0	0.0027
	22.1	3.21	6786.9	0.1200
	20.8	0.536	57.0	0.0032
	21.1	0.533	119.6	0.0067
RUN20	22.2	0.526	763.5	0.0409
	24.8	0.518	2995.7	0.1471
	26.5	0.517	4817.1	0.2234

Table 5.2: Total velocity dispersion, mass in sinks, and total SFE ($= M_*/(M_* + M_{\rm cold})$) at the times analyzed in the two simulations. Here, $M_{\rm cold}$ is the total mass in cold gas ($n > 50$ cm^{-3}).

5.2.2 Generation of the clump ensemble

In the present work, we use the term "clump" in a loose way, simply to denote a local density enhancement above a given density threshold, except for the objects defined at the highest thresholds ($n_{\rm th} \geq 10^5$ cm^{-3}), which will be referred to as "cores", and those defined at the lowest thresholds ($n_{\rm th} = 300$ cm^{-3}), which will be sometimes referred to as "clouds". No implication is made about a specific density or mass range for the clumps, nor about whether they will form only a few stars, or a cluster. This is a somewhat looser usage of the term "clump" than the meaning adopted sometimes, of clumps being the gaseous objects from which stellar clusters form (see, e.g., the review by Blitz & Williams, 1999). However, for the purposes of the present study, which considers objects with a variety of densities and masses, our more generic terminology is adequate. Note that, in general, a single clump at a lower threshold may contain several clumps at a higher one.

In what follows, we first describe the procedure for finding the clumps, and then the selection criteria to include them in our sample.

5.2.2.1 Clump finding algorithm

The procedure to find clumps in the simulation was performed directly in the SPH particles, without a previous mapping onto a grid. This allows the procedure to find the clumps in a manner independent of the grid resolution and without the smoothing inherent to the gridding procedure.

The procedure is the following. First, we select all the SPH particles in the simulation with density above a certain threshold, n_{th}. We then locate the particle with the highest density. This particle and all those located within its smoothing length are labeled as members of the clump. Then, the following steps are iterated: we locate the member of the clump with the highest density to which this subprocedure has not been applied, and then label as members all the particles within a smoothing length not-yet belonging to the clump. The iteration ends when all the clump members are examined. If there are particles remaining with density $n > n_{th}$ that are not yet members of any clump, we locate the one with the highest density and use it to define a new clump and the procedure is repeated.

In summary, this procedure finds the largest connected object above a volume density threshold.

5.2.2.2 Clump sample

For the analysis of both simulations we only considered clumps with more than 80 SPH particles ($M \geq 4.8\ M_{\odot}$ in RUN03 and $M \geq 1.6\ M_{\odot}$ in RUN20), in order to guarantee that they are well resolved, according to the criterion by Bate & Burkert (1997). This amounts to twice the number of particles contained within one particle smoothing length.

Since in RUN03 we first apply a turbulent driver, and then we leave the simulation to decay and collapse, we analyze various timesteps that correspond to different levels of the turbulence and different evolutionary stages of the clouds and clump populations. Specifically, we analyze the simulation at $t = 15.6$, 18.1, 18.5, 19.5, and 22.1 Myr. Sink ("star") formation begins in the simulation at $t \sim 14.7$ Myr, and at $t = 22.1$ the total mass in sinks is $6787 M_{\odot}$, amounting to $\sim 0.4\%$ of the total mass in the box, and $\sim 4\%$ of the cold gas mass. At these times, we generate an ensemble of clouds, clumps and cores by applying the clump-finding algorithm at the density thresholds, $n_{\rm th} = 300$, 10^3, 3×10^3, 10^4 and 10^5 cm^{-3}, for both simulations.

In RUN20 the turbulence in the cloud develops self-consistently, and so it never is excessive (i.e., not larger than what would be produced self-consistently by the gravitational contraction). Nevertheless, the structures (filaments and clumps) still

evolve, the filaments gathering mass by accretion from their surrounding medium, and the filaments themselves feeding the clumps inside them (Gómez & Vázquez-Semadeni, 2014). However, close inspection of the evolution of the filament/clump systems shows that they form at about the same time, and the flow along the filaments toward the clumps develops later (see also Gong & Ostriker, 2015). This will be relevant later in the investigation of whether the accretion from the filaments onto the clumps has any effects on the dynamics of the latter. In this simulation we choose timesteps that exhibit well-defined filament/clump systems, in order to study whether clumps accreting from filaments exhibit systematically larger velocity dispersions than those expected from energy equipartition considering the mass of the clump only. Specifically, we consider time steps at $t = 20.8$, 21.2, 23.2, 24.8 and 26.5 Myr.

In order to find cores of high column density we selected some timesteps [4], $t =$ 18.1 and 18.5 Myr for RUN03, and $t = 20.8$ and 21.2 Myr for RUN20, and we applied the clump-finding algorithm at $n_{\rm th}$ =3x10^5 and 10^6.

In the SPH simulations used in this work, the SPH particle mass ($m_{\rm SPH}$; see Table 5.1) is fixed. Thus, for clumps satisfying the above conditions, we compute the gas mass as $M_{\rm gas} = N_{\rm cl} m_{\rm SPH}$, where $N_{\rm cl}$ is the number of SPH particles contained in the clump. Note that , in general, the measured masses are smaller at higher thresholds, because denser objects are embedded within larger ones that are more massive, but less dense on average.

Finally, note also that the clumps exhibit complex morphologies, being far from spherical in general, and often display elongated and twisting shapes, as shown in Fig. 5.1. This implies that there is an inherent ambiguity in the definition of the clump size, since in general they have more than one characteristic dimension. With this caveat in mind, we compute the clump "radius" as $R = (3V/4\pi)^{1/3}$, where V is the sum of the specific volumes of all particles that belong to a clump, i.e.,

$$V = \sum_{i=1}^{N_{\rm cl}} V_i = \sum_{i=1}^{N_{\rm cl}} \frac{m_{\rm sph}}{\rho_i} = m_{\rm sph} \sum_{i=1}^{N_{\rm cl}} \rho_i^{-1}, \tag{5.5}$$

where ρ_i is the density of particle i. With this definition, the mean density of the

[4] It is important to note that the original timestep between successive dumps in both simulations was $\Delta t = 0.136$ Myr. This timestep proved inadequate to resolve the formation and collapse of the densest clumps which, at $n > 10^6$ cm^{-3}, have free-fall times $\tau_{\rm ff} \lesssim 0.045$ Myr. Therefore, to find cores of high column density we restarted the simulations shortly before new sinks appeared with 10 times finer temporal resolution.

clump ($\bar{\rho} = M/V$) is given by,

$$\bar{\rho} = \frac{m_{\rm sph} N_{\rm cl}}{m_{\rm sph} \sum_{i=1}^{N_{\rm cl}} \rho_i^{-1}} = \frac{N_{\rm cl}}{\sum_{i=1}^{N_{\rm cl}} \rho_i^{-1}}. \tag{5.6}$$

Since feedback is not included in either of our simulations, we need to apply some kind of criterion to avoid including clumps that exhibit unrealistic physical properties because feedback should be already dominating their dynamics if it had been included. We therefore consider only clumps that, at a density threshold of $n_{\rm th} = 10^5$ cm^{-3}, have a star formation efficiency SFE$_5$ $< 65\%$, where the SFE$_5$ is defined as

$$\mathrm{SFE}_5 = \frac{M_*}{M_{\rm tot,5}}, \tag{5.7}$$

and $M_{\rm tot} = M_* + M_{\rm gas,5}$, M_* is the mass in stars (sink particles) and $M_{\rm gas,5}$ is the mass in dense gas above $n = 10^5$ cm^{-3}. We choose this value as a compromise between realistic SFEs for massive cluster-forming clumps (10–50%, Matzner & McKee, 2000; Lada & Lada, 2003) and obtaining a reasonably large statistical clump sample.

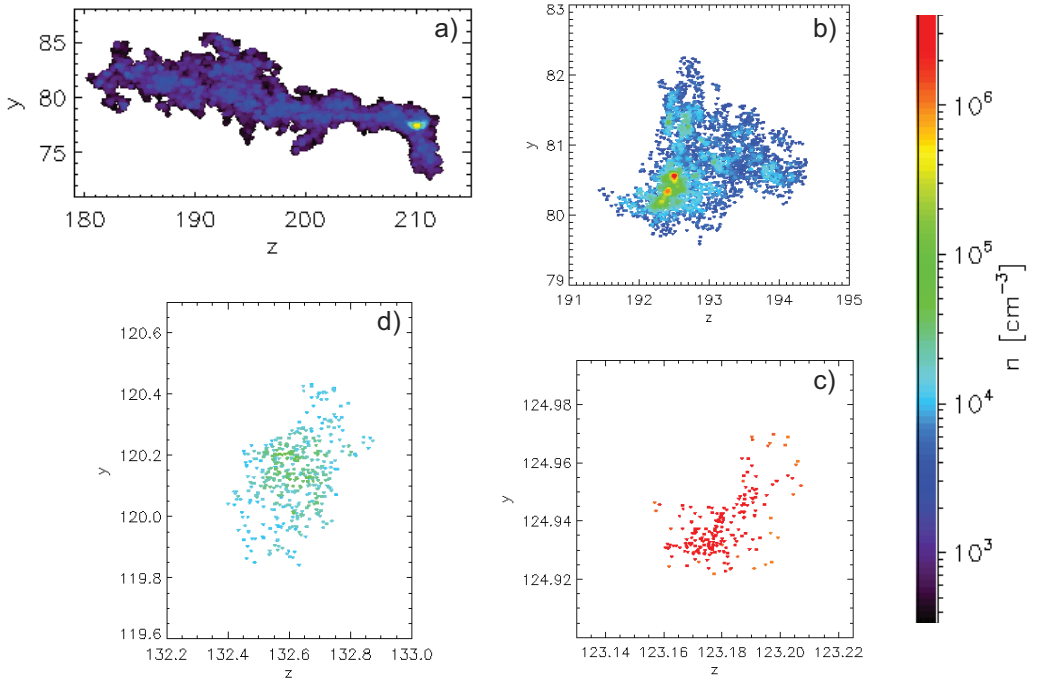

Figure 5.1: Clumps at different density thresholds and snapshots in both simulations at the same density scale. a) Clump in RUN03 at $n_{th} = 300\ n_0$; b) RUN20, $n_{th} = 10^3\ n_0$; c) RUN03, $n_{th} = 3 \times 10^3\ n_0$; d) RUN20 $n_{th} = 10^4\ n_0$. We find, in general, more elongated structures than spherical.

For lower clump-defining density thresholds, we must impose a further restriction on the maximum accepted SFE at each threshold. Star formation is a highly spatially intermittent phenomenon, so that star-forming sites only occur at a few and highly localized positions that have the highest densities in a large MC. Thus, if one focuses on a given star-forming site and measures the gas mass around it at various thresholds, this mass will be larger for lower thresholds, since this procedure includes progressively more material from progressively larger distances from the star-forming site. In consequence, the measured SFE around a star-forming site will be smaller at lower thresholds (as long as no other site enters the domain defined by the threshold). This is consistent with the general trend that lower-density objects generally are observed to have lower SFEs (e.g., Palau et al., 2013; Louvet et al., 2014).

To replicate this trend, we require progressively smaller efficiencies at lower thresholds in order to admit a clump in our sample. Thus, the maximum star formation efficiency, $\mathrm{SFE}_{\mathrm{max},i}$, for any clump included in our sample at threshold i is given by

$$\mathrm{SFE}_{\mathrm{max},i} = \left(\frac{M_5}{M_i}\right) \mathrm{SFE}_5, \tag{5.8}$$

where M_5 is the total mass in clumps defined at threshold $n_{\mathrm{th}} = 10^5$ cm^{-3}, M_i the total mass in clumps defined at the i-th threshold, $n_{\mathrm{th},i}$, and $\mathrm{SFE}_5 = 65\%$. Figure 5.2 shows the mass fraction M_5/M_i as a function of $n_{\mathrm{th},i}$ for the two simulations. With this prescription, we avoid including clumps whose measured SFEs at low thresholds are so large that at a higher threshold they would exceed the maximum SFE allowed for it.

5.3 Results

5.3.1 Testing for Larson's relations

5.3.1.1 The density-size relation

We first check whether our clump sample, occurring in clouds undergoing global collapse, satisfies Larson-like relations. Figure 5.3 shows our clumps in the n *vs.* L and σ_{v} *vs.* L diagrams for the two simulations. In this plot, the different colors represent different column densities, the dashed lines represent various column densities, and the symbols correspond to the volume density thresholds used to define the clumps.

Due to the resolution requirement that our clumps contain at least 80 SPH particles, our sample is mass-limited from below, so that the clumps are constrained

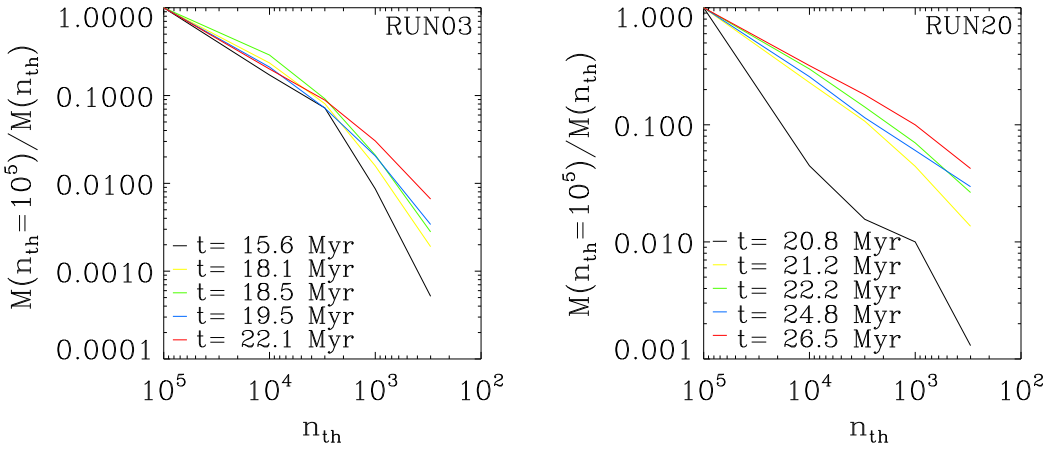

Figure 5.2: Maximum SFE ($\mathrm{SFE}_{max,i}$) allowed for clumps included in the sample as a function of density threshold, $n_{\rm th}$, as given by eq. (5.8), at the various timesteps considered in the two simulations.

to have masses $M_{\rm cl} \geq 1.6\,M_\odot$ in RUN20 and $M_{\rm cl} \geq 4.8\,M_\odot$ in RUN03.

A first point to notice in Fig. 5.3 is that RUN03 produces more clumps than RUN20. This is because in RUN03 the density structures are scattered throughout the simulation domain, since the clouds and clumps have been produced from a large number of turbulent fluctuations in the early stages of the run. Instead, in RUN20 there is only a single large cloud complex, produced initially by the collision of the large cylindrical WNM streams.

From Fig. 5.3, we also see that our clump sample does not follow the standard Larson $n \propto R^{-1}$ relation (Fig. 5.3). Instead, the entire sample occupies a triangular region in the n-R diagram, so that no single density-size relation exists. Additionally, we observe a very well defined group of points at nearly constant density for each volume density threshold. However, we also observe that, when the clumps are classified by column density (with various column density ranges shown as the different colors in the figure), then each sub-sample traces a slope R^{-1} as in the Larson (1981) density-size relation. This supports the notion that the density-size relation is an artifact of defining clumps by a column density threshold.

The fact that the clumps defined at a certain volume density threshold appear to have a nearly constant *volume* density was already noticed in numerical simulations by Vázquez-Semadeni et al. (1997) and Ballesteros-Paredes & Mac Low (2002), and later interpreted by Ballesteros-Paredes et al. (2012) and Beaumont et al. (2012) as a consequence of the steep slope of the high-density side of the density PDF, which implies that most of the volume (and even the mass) is at the lowest densities

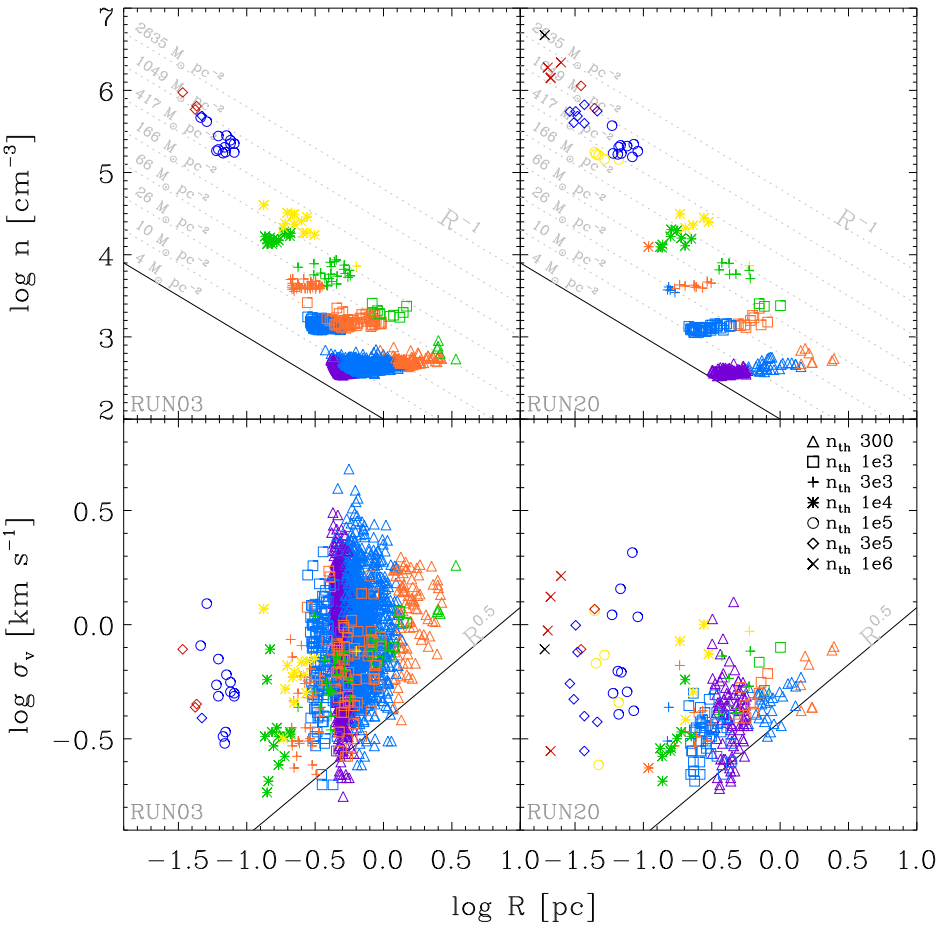

Figure 5.3: Larson-like relations for simulated clumps and cores. Symbols correspond to the volume density threshold used to define clumps. The dotted lines correspond to constant column density values and colors represent the different column density-ranges, bounded by the values of the dotted lines. Purple: $\Sigma < 10 M_\odot \mathrm{pc}^{-2}$; blue: $10 < \Sigma < 26 M_\odot \mathrm{pc}^{-2}$; orange: $26 < \Sigma < 66 M_\odot \mathrm{pc}^{-2}$; green: $66 < \Sigma < 166 M_\odot \mathrm{pc}^{-2}$; yellow: $166 < \Sigma < 417 M_\odot \mathrm{pc}^{-2}$; blue: $417 < \Sigma < 1049 M_\odot \mathrm{pc}^{-2}$; red: $1049 < \Sigma < 2635 M_\odot \mathrm{pc}^{-2}$, and black: $\Sigma > 2635 M_\odot \mathrm{pc}^{-2}$. Note that, by selecting clumps by column density, each sample follows a Larson-like density-size relation.

allowed by the threshold, if the threshold is above the density corresponding to the maximum of the PDF. The same is expected to happen for the column density, if it is also described by a lognormal or a power law with a slope steeper than -1 (Ballesteros-Paredes et al., 2012), again reinforcing the notion that the apparent constant column density of molecular clouds is an artifact of the restricted column density range allowed by the tracers used to observe them, such as the ^{12}CO line.[5]

[5]It has been argued by Lombardi et al. (2010) that the constant column density of molecular clouds is an actual physical property of molecular clouds, which can be observed in dust extinction maps that allow thresholds significantly lower than that claimed for the physical column density of the molecular clouds. However, the proposal by Ballesteros-Paredes et al. (2012) is that it is

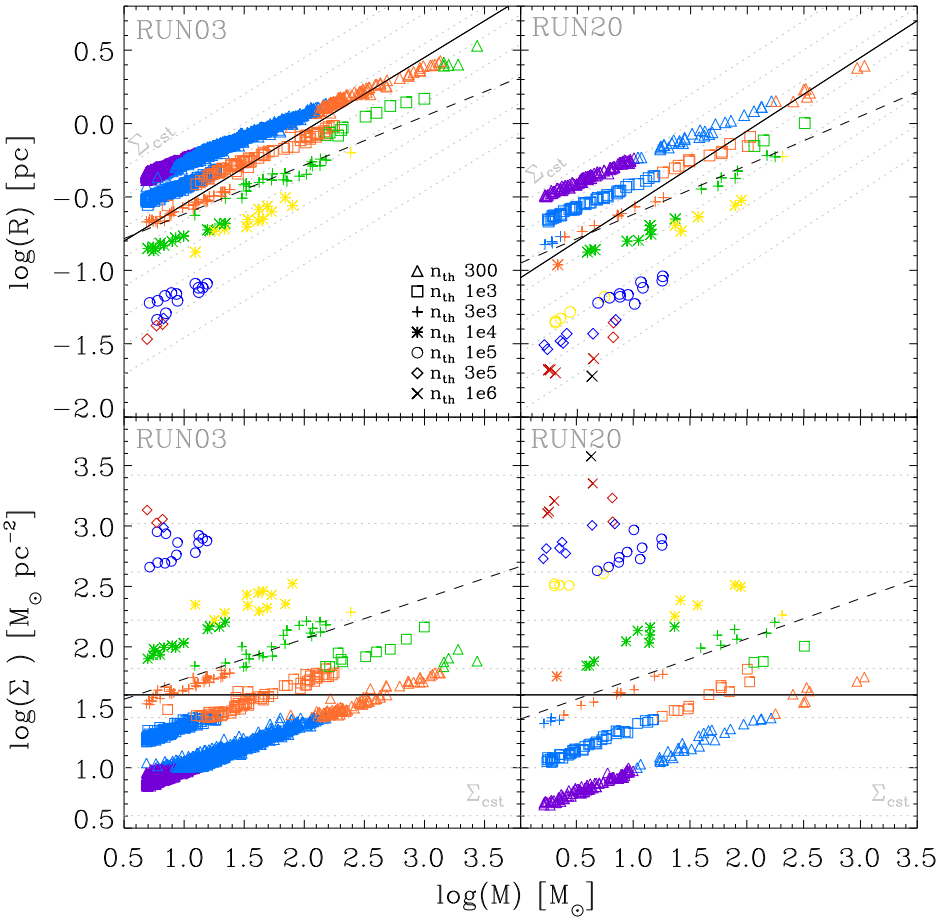

Figure 5.4: Size and column density *vs.* mass. The solid lines show the scaling implied by the density-size Larson-like relation; the dashed lines show the slope 1/3 corresponding to constant volume density. The color scheme, the symbols and the values of Σ (dashed gray lines) are the same as used in Fig. 5.3. Note that the clumps belonging to a given Σ range follow a scaling similar to that implied by Larson's density-size relation.

An expression equivalent to Larson's density-size is that of mass *vs.* size, which reads $M \propto R^2$. Figure 5.4 shows the scaling of size *vs.* mass (top panels) and also the column density *vs.* mass (bottom panels) for our clump sample in the same Σ ranges as in Fig. 5.3. Solid lines correspond to $M \propto R^2$ (or constant-Σ). Again, it can be seen that, in both simulations, when the entire sample is considered, the clumps do not show constant column density (top panels, Fig. 5.4) nor an $M \propto R^2$ scaling (bottom panels, Fig.5.4). However, such a correlation reappears when the data are classified by column density. On the other hand, at every volume density threshold (different symbols for each threshold) clumps show the relation $R \propto M^{1/3}$, denoted by the dashed black line in Fig. 5.4, which is the scaling expected for clumps

a result of an observational selection effect arising from the threshold column density imposed by the observational technique.

of constant volume density (Ballesteros-Paredes et al., 2012; Beaumont et al., 2012).

It is worth noting in the *top* panels of Fig. 5.4 that clumps in a given range of column densities include clumps defined at various *volume* density thresholds. Nevertheless, there is a net trend for clumps defined at higher volume density thresholds to fall in higher column density ranges. This behavior is also present in observational data (see, e.g., Figure 14 of Barnes et al., 2011).

5.3.1.2 The linewidth-size relation

With respect to the $\sigma_{\rm v}$-R relation, we notice in Fig. 5.3 that the $\sigma_{\rm v} \propto R^{1/2}$ scaling is not satisfied by the whole clump sample in either of the simulations and, instead, the ensemble of clumps fills a large area in the $\sigma_{\rm v}$-R diagram (as is often the case in observational surveys as well; see, e.g., Heyer et al., 2001; Ballesteros-Paredes et al., 2011; Heyer & Dame, 2015, and references therein). However, it can be observed that the clumps with $\log(R/{\rm pc}) \gtrsim -0.5$ are bounded from below by approximately the Larson slope (right panels of Fig. 5.3). A similar effect was observed by Vázquez-Semadeni et al. (1997). In addition, it is also noticeable that some of the samples at certain Σ ranges (see, for example the orange and green points) seem to follow this scaling. In Sec. (5.3.2.4) we discuss the origin of the observed scatter.

5.3.2 Generalization of Larson's relations and energy balance

5.3.2.1 The $\mathcal{L} - \Sigma$ diagram

The results from the previous section show that the clumps defined by volume density thresholds in the clouds in our simulations of global, hierarchical gravitational collapse do not seem to follow the linewidth-size relation. Instead, Larson-like density-size (and equivalent) relations appear when the selection of the clumps is done by means of a *column* density threshold or range. Larson-like linewidth-size relations appear for *some* of the clumps.

We now test whether our clump sample follows a relation of the form of eqs. (5.3) or (5.4); i.e., we test for whether the clouds appear to be near virial equilibrium or energy equipartition, respectively, where the latter is consistent with free-fall. These relations can be considered as the generalization of Larson's relations when the column density of the objects in the sample is not constant.

Figure 5.5 shows the ratio $\sigma/R^{1/2}$ *vs.* Σ for clumps in RUN03 and RUN20. The solid line corresponds to virial equilibrium and the dashed line corresponds to energy

equipartition, or free-fall condition. Contrary to figures 5.3 and 5.4, in these plots we use colors to denote the volume density thresholds at which clumps were defined, and different symbols to represent the timesteps considered in each simulation. Column density has been computed as $\Sigma = M_g/\pi R^2$ where M_g represents the gas mass in the clump (we will consider the stellar mass—i.e. sink mass, M_*—later).

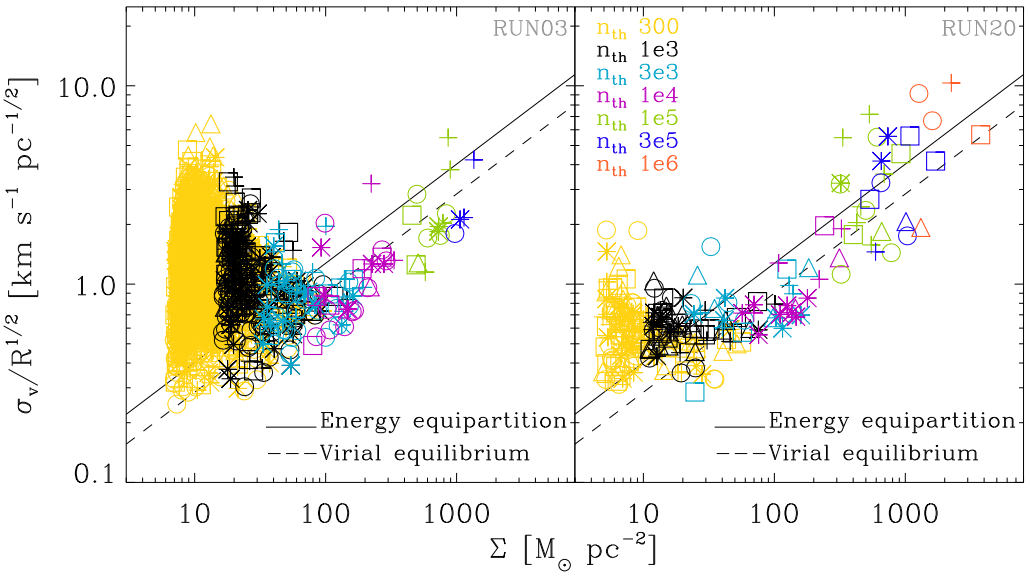

Figure 5.5: Generalization of Larson's scaling relations. The clouds at $n_{\rm th} = 300n_0$ can be considered as atomic because of their low column density. Here, colors represent the different volume density thresholds used to define clumps with the clump-find algorithm described in section 5.2.2. Symbols represent different time-steps for RUN03 (△=15.6, □=18.1,+=18.5, ∗=19.5, ◯=22.1) and RUN20 (△=20.8, □=21.2,+=22.2, ∗=24.8, ◯=26.5).

5.3.2.2 Low-column density clumps

The first noticeable feature in these plots is the group of clumps at the lowest volume density threshold, i.e. $n_{\rm th} = 300n_0$ (yellow symbols), which also have the lowest surface densities. These clumps are seen to occupy a region in the diagram that extends from the virial and free-fall lines to over one order of magnitude in $\sigma_{\rm v}/R^{1/2}$ above those lines, at roughly constant column density. We note that this is precisely the kind of behavior displayed in observational clump surveys (see, e.g., Figure 10 of Keto & Myers (1986) and Figure 13 of Leroy et al. (2015)).

Another frequent way of displaying the energy balance of the clumps is by plotting the "virial parameter" $\alpha = 2{\rm E_k}/|{\rm E_g}| = 5\sigma_{\rm v}R/GM$. Figure 5.6 shows this parameter versus the clump mass for the two simulations. As in Fig. 5.3, the clumps with the lowest masses exhibit the largest scatter in α, with excesses of up to nearly

two orders of magnitude. Again, this is similar to the observed behavior of clump surveys (see, e.g., figure 16 of Barnes et al., 2011).

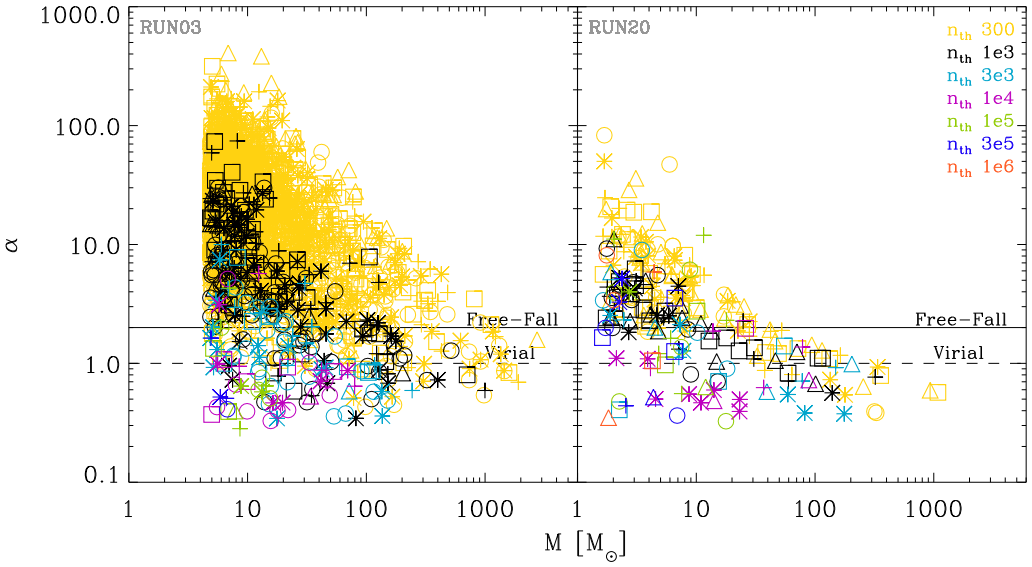

Figure 5.6: α parameter as a function of mass for the clumps for both simulations. Symbols represents different time steps, RUN03 (△=15.6, □=18.1,+=18.5, ∗=19.5, ◯=22.1) and RUN20 (△=20.8, □=21.2,+=22.2, ∗=24.8, ◯=26.5).

This behavior is generally interpreted as implying that these clouds have an excess of kinetic energy over their gravitational energy, therefore being unbound, and needing to be confined by an external pressure to avoid rapid dispersal or else that they are being dispersed by the energizing action of stellar feedback. This latter outcom is not possible in our simulations, because we have not included any kind of stellar feedback, with the purpose of examining the action of only the initial assembling turbulent motions and of the gravitationally-driven motions.

An alternative possibility is that, if turbulent compressions in the atomic interstellar medium (ISM) are causing the early assembly stages of these clouds, their associated velocities may be larger than the corresponding gravitational velocities for those objects, although in this case their role is to *assemble* the clouds rather than to disperse them, in the context of *converging flows* from large-scale turbulent fluctuations. Later, as a cloud gains mass, its gravitational velocity may begin to dominate over the initial turbulent compression that started it, which may itself tend to dissipate.

To test for this, in the *top row* of Fig. 5.7 we show the clouds obtained at the lowest density threshold ($n_{\rm th}$ = 300 cm^{-3}) in the $\mathcal{L} - \Sigma$ diagram, but represent-

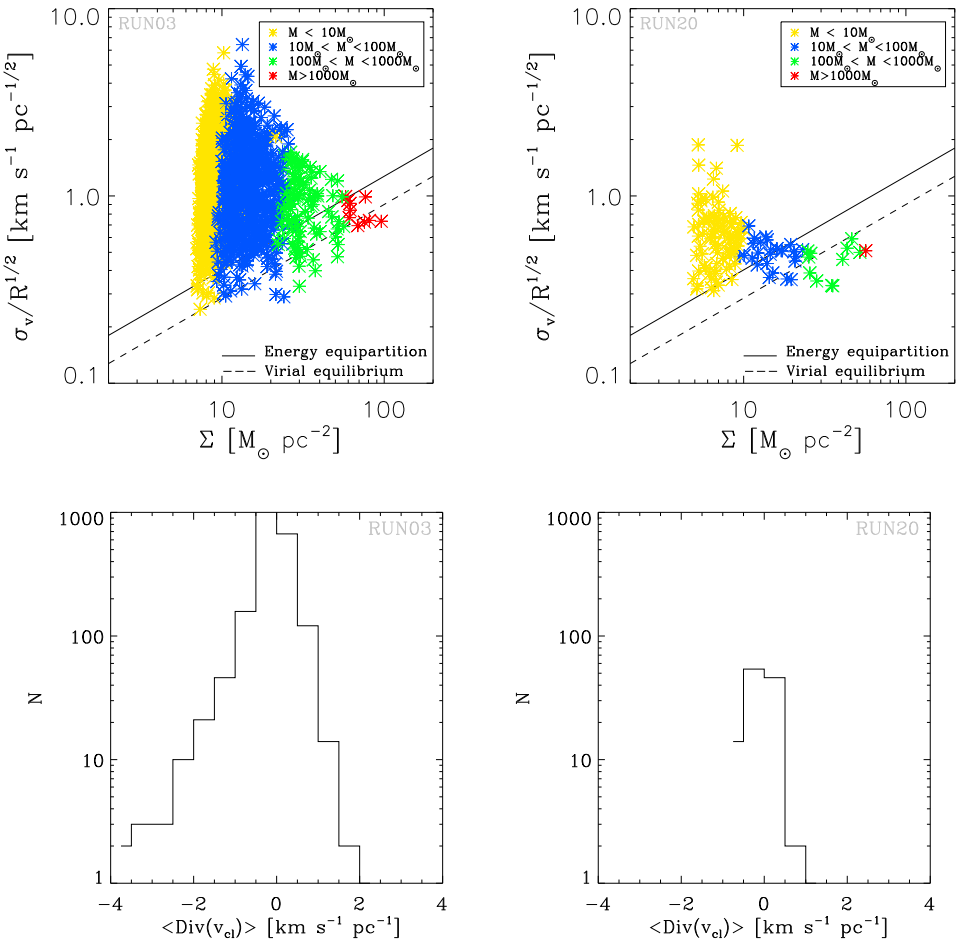

Figure 5.7: *Top:* Clumps defined at the lowest density threshold ($n_{\rm th} = 300\,{\rm cm}^{-3}$) plotted in the $\mathcal{L} - \Sigma$ diagram. Clumps at the lowest volume density threshold generally have the lowest column densities as well. Different colors represent clumps in different mass ranges. The most massive clumps are seen to lie closest to the virial and equipartition lines. The *bottom* row shows the histograms of the mean velocity divergence in the clumps defined at $n_{\rm th} = 300$ cm^{-3} and with masses $M < 100 M_{\odot}$, in RUN03 (*left*) and in RUN20 (*right*).

ing different mass ranges with different colors. Note that colors in these plots are also representative of sizes ranges, given that all these clumps have similar volume densities (cf. Sec. 5.3.1.1), and therefore the most massive ones are also the largest ones. The most massive clumps are seen to lie closest to the virial and equipartition lines, suggesting that these objects tend to be dominated by the gravitational velocity rather than by the turbulent velocity. This means that they have the largest gravitational velocities at a given column density, consistent with an evolutionary picture where the clumps are first assembled by large-scale turbulent compressions and, as they grow, they change from turbulent assembly to gravitational contraction.

This scenario can be further tested by measuring the mean velocity divergence in each clump [6], which shows whether the clump is contracting or expanding as a whole. A negative mean divergence means that the clump is contracting on average and, if its velocity is not driven by gravity, then its contraction must be a turbulent compression from the outside gas (e.g., Vázquez-Semadeni et al., 2008; González-Samaniego et al., 2014; Pan et al., 2015). The *bottom row* of Fig. 5.7 shows the histograms of the mean velocity divergence of all the clouds defined at the lowest threshold ($n_{\rm th} = 300$ cm^{-3}) and with masses $M < 100 M_\odot$ which are the clumps exhibiting the largest scatter in the $\mathcal{L} - \Sigma$ diagram. We see that more than half of the clumps ($\sim 60\%$ in both simulations) have negative divergence, indicating that they are contracting on average, and therefore are in the process of *assembly*, although significant fraction is undeniably in the process of *dispersal*.

Figure 5.8 shows the velocity divergence histograms for all the SPH particles conforming some individual clumps, at similar masses (*top*: low-mass, *bottom*: intermediate-mass) and different values of the mean velocity divergence (*left*: negative, converging clumps; *right*: positive, dispersing clumps). From this figure, we note that the clumps, in general, contain a wide range of values of the divergence; quite wider, in fact, than the range of *average* divergences seen in Fig. 5.7, as expected for the distribution of partial averages of a random variable. In particular, even the clumps with negative mean divergence contain a substantial amount of particles where the local divergence is positive. Note, however, that a local positive divergence does not necessarily imply that the object is expanding globally. For example, a core undergoing non-homologous collapse, with an increasing infall velocity towards its center, will have a positive divergence in its envelope, because of the stretching caused by the differential infall speed. This in fact suggests that in fact our estimate of the fraction of contracting clumps based on the mean divergence may actually underestimate the actual fraction.

5.3.2.3 High-column density clumps

While in the previous section we have discussed the kinetic energy excess in low-column density clumps in the $\mathcal{L} - \Sigma$ diagram, another feature in Fig. 5.5 is that some of the highest-column density objects also exhibit an excess of kinetic energy over the equipartition value, especially in the case of RUN20.

[6] The particle velocity divergence was obtained directly from the GADGET-2 code, which computes the divergence in terms of the kernel function, the density and the velocity of each particle. Therefore, the errors in the velocity divergence are of the same order as those in the integration of the equations.

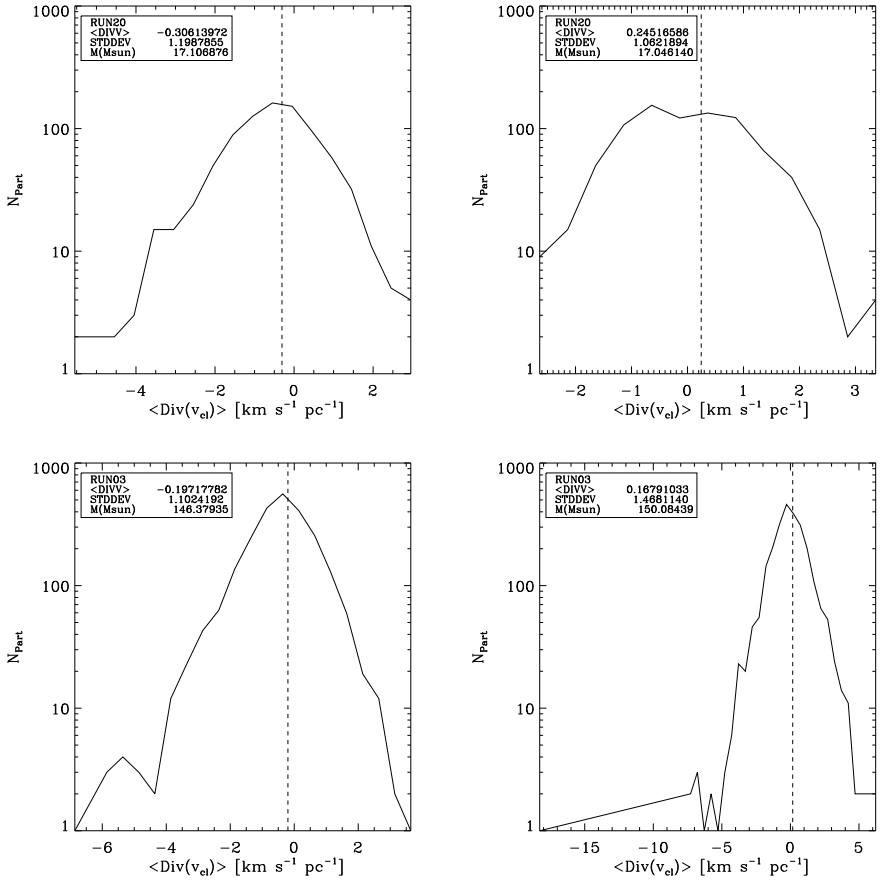

Figure 5.8: Histograms of the velocity divergence for all the SPH particles belonging to four representative low- to intermediate-mass individual clumps from both simulations. The *top* row shows clumps from RUN20, and the *bottom* row shows clumps from RUN03. The *left* colums shows clumps with negative mean divergence (i.e, converging on average), while the *right* column shows clumps with positive mean divergence (i.e., diverging on average).

As mentioned in Sec. 5.1.2, clumps that appear significantly above (by factors of a few) the virial equilibrium line in the $\mathcal{L}-\Sigma$ diagram have often been interpreted as being gravitationally unbound, and requiring an external confining pressure to avoid being dispersed in a crossing time (e.g., Keto & Myers, 1986; Field et al., 2011). However, it is also possible that the apparent kinetic energy excess is due to an underestimation of the relevant gravitational mass involved in the clump dynamics, as proposed, for example, by H09 for their MC sample. Two mechanisms that come to mind for providing additional mass beyond that directly measured in a clump are the mass in stars and the mass of external accreting material that is part of the same gravitational potential well. Even if our high-Σ clumps and cores do not show a very large excess in the $\sigma_{\rm v}/R^{1/2}$ ratio, we investigate their energetics under these two possibilities.

- **The "stellar mass effect"**

  One obvious source of mass in protostellar cores is the mass in (proto-)stellar objects which, in the case of cluster-forming clumps, may reach observed values of up to 30–50% (Lada & Lada, 2003). We thus re-compute the location in the $\mathcal{L} - \Sigma$ diagram of those cores and clumps that do contain sink particles, adding the mass of the latter to the computation of the core column density (i. e., now we consider $\Sigma = (M_g + M_{sink})/\pi R^2$). The result is shown in Fig. 5.9, where symbols represent the same timesteps as in Fig. 5.5 and clumps and cores that contain stellar particles are marked with a red diamond. From this figure, it is clear that the affected cores undergo a displacement in the $\mathcal{L} - \Sigma$ diagram that relocates them closer to the virial equilibrium line in the case of RUN03, and to the region between the energy equipartition and virial equilibrium lines in RUN20. However, some cores with such an excess do not contain sinks, and for them, the excess cannot be explained by this correction.

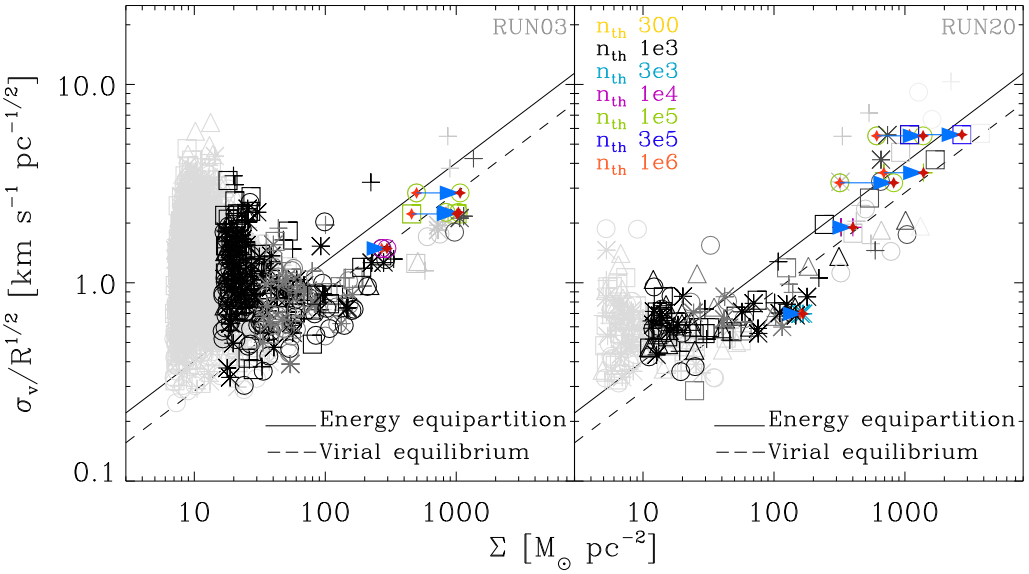

Figure 5.9: Correction to the location of sink-containing cores in the $\mathcal{L} - \Sigma$ diagram (indicated by the arrows) due to the inclusion of the mass in sinks in the clumps' energy balance. The cores with sinks are denoted by a red diamond. As in figure 5.5, different symbols represent different times.

- **The "filament effect"**

  A second possible mechanism for missing relevant gravitational mass in a core may be if the core is gravitationally accreting material from a surrounding structure, with the accretion driving turbulence into it (Klessen & Hennebelle,

2010). In particular, it has been found both in observations (e.g., Schneider et al., 2010; Kirk et al., 2013; Peretto et al., 2013) and numerical simulations (Gómez & Vázquez-Semadeni, 2014), that filaments may provide an accretion channel of cloud material onto cores. In this case, it is reasonable to ask whether the velocity dispersion in the core reflects the gravitational potential of the entire filament/core system.

To test for this possibility, in both simulations we visually examined the set of dense cores in our sample exhibiting a kinetic energy excess, but not the "sink effect", to determine whether they belonged to a filament. Rather surprisingly, we found none. We thus reversed the procedure, visually searching for filament/core systems, and then analyzing their energy budgets.

Figure 5.10 shows one such filament/core system from RUN20 at $t = 26.5$ Myr at different density thresholds. The *right- bottom* corner of this figure shows this system on the $\mathcal{L} - \Sigma$ diagram. Contrary to our expectation, this filament/core system exhibits a *lower* value of the ratio $\sigma_{\rm v}/R^{1/2}$ than that expected for a spherical configuration, appearing *below* both the equipartition and the virial-equilibrium lines in this figure. In hindsight, this is actually natural, since the gravitational potential of a filamentary object of length L is much lower than that of a spherical object of diameter L and the same volume density, implying that the velocity dispersion of the former should be significantly lower than that of the latter (Toalá et al., 2012; Pon et al., 2012).

However, it might still be possible that the central, roundish core, should have a larger velocity dispersion than that of an isolated core of the same dimensions and in equipartition, because of the accretion from the filament. Unfortunately, this system only appears roundish at $n_{\rm th} = 10^6$ cm^{-3}, and even at this threshold density, the core appears sub-virial. In fact, we had to relax our minimum-mass selection criterion (cf. Sec. 5.2.2.2) in order to include this core in the system, since it only contains 60 SPH particles, and it is therefore likely to be significantly affected by numerical dissipation. Thus, we cannot determine where it would be located in the $\mathcal{L} - \Sigma$ diagram had it been free of numerical dissipation.

To try to answer this question, we searched for some other filament/core systems at larger scale, so that the central core would have a sufficient number of particles to be relatively free of numerical dissipation. However, we have been unable to accomplish this task, because of our restriction that the cores should have an SFE $< 65\%$ at $n_{\rm th} = 10^5$ cm^{-3}. Indeed, we found that all larger cores

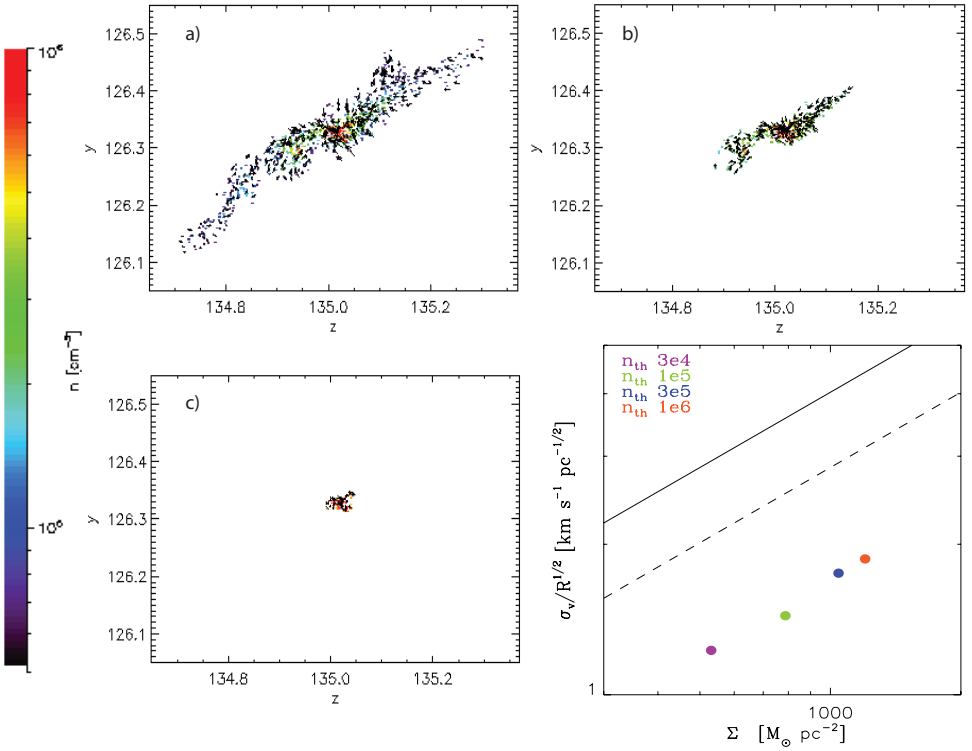

Figure 5.10: Filament/core system above a) $n_{\rm th} = 10^5$, b) 3×10^5 and c) 10^6 cm^{-3}. The right-bottom corner shows the filament/core system in the $\mathcal{L} - \Sigma$ diagram at thresholds $n_{th} = 10^4$, 3×10^4, 10^5, and 10^6 cm^{-3}. The points corresponding to the various thresholds are seen to describe a line parallel to the equipartition and virial-equilibrium lines, but displaced to a lower value of the ratio $\sigma_{\rm v}/R^{1/2}$, except for the point corresponding to $n_{\rm th} = 10^6$ cm^{-3}, which is probably affected by numerical dissipation.

that appeared to be accreting from filaments already had efficiencies larger than this. This seems to be a consequence of the fact that the filaments and the cores grow roughly simultaneously, and accretion from the filament onto the core only begins by the time the core has already undergone significant sink formation, as also noted by Gong & Ostriker (2015). This suggests that cores located within filaments in their prestellar or early protostellar stages should not exhibit excess kinetic energies, because they are not accreting significantly from their filaments at these stages.

We conclude that filaments, and the pre- and protostellar cores located within them, tend to exhibit sub-virial velocity dispersions, due to the lower gravitational energies of these configurations than those of the spherical structures assumed for the virial velocity dispersion estimate.

- **Dispersing clumps and cores**

  After considering both corrections by the mass in sink particles and by existing in a filamentary environment, we are nevertheless left with some dense cores whose kinetic energy excess cannot be explained by either of these effects. Such is the case, for example, of the cores indicated by the green and red '+' symbols with high values of $\sigma_{\rm v}/R^{1/2}$ in the right panel of Fig. 5.9. Figure 5.11 shows this core at a threshold $n_{\rm th} = 10^5$ cm^{-3} and at three times separated by 0.2 Myr, with the arrows indicating the velocity field on the plane shown. It can be seen that the core is actually being disrupted, and so this is indeed a case of a starless core that will probably never form stars.

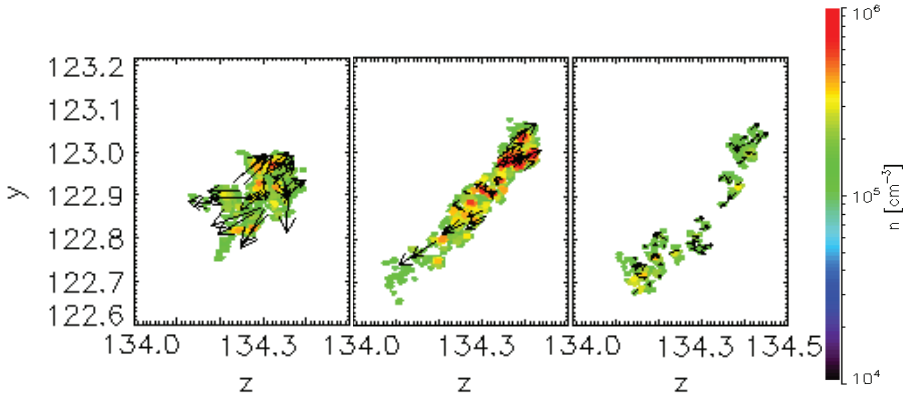

Figure 5.11: High-column density core from RUN20 at times t = 22.2, 22.4 and 22.6 (from left to right)Myr at $n_{th} = 10^5 \mathrm{cm}^{-3}$, showing that the core is being disrupted. The velocity field, shown by the arrows, also indicates that the clump is being dispersed, since in general it is divergent.

5.3.2.4 Scatter propagation from $\mathcal{L} - \Sigma$ to Larson

Figure 5.5 shows a considerable scatter, especially for low-Σ. In particular, it is clear that the scatter is reduced as Σ increases. We have interpreted this effect as a consequence of an increasing relative importance of self-gravity at increasing column density, except for those high-density objects that are being disrupted. Since we have argued that a Larson-like linewidth-size relation appears for objects near equipartition that are furthermore selected by near-constant column density, the scatter around equipartition should cause a scatter around the velocity dispersion-size relation as well. Indeed, a large scatter is also observed in the velocity dispersion-size plots for both runs (cf. Fig. 5.3)

To quantify this, we note that the scatter in the quantity $\mathcal{L} \equiv \sigma_{\rm v}/R^{1/2}$ is related to that in the velocity dispersion and in the radius by

$$d\ln\mathcal{L} = d\ln\sigma_{\rm v} - \frac{1}{2}d\ln R. \tag{5.9}$$

The scatter $d\mathcal{L}$ around the equipartition value $(2\pi G\Sigma/5)^{1/2}$ (cf. eq. [5.4]) represents the (physical) deviation from equipartition for a given clump. Because the scatter $d\mathcal{L}$ merges the scatter in $\sigma_{\rm v}$ and in R, it is not possible to determine how $d\ln\mathcal{L}$ is distributed among $d\ln\sigma_{\rm v}$ and $d\ln R$. However, we can obtain an upper limit in the expected scatter in $\sigma_{\rm v}$ if we assume that it "absorbs" all of the scatter in $\mathcal{L}$, with none of it going to R; that is, assuming $d\ln\sigma_{\rm v} = d\ln\mathcal{L}$. In Fig. 5.12 we have plotted the error bars for $\sigma_{\rm v}$ in the velocity dispersion-size relation corresponding to the scatter in the $\mathcal{L}$ ratio from Fig. 5.5, for the three different column density ranges (represented with the color of the error bars, which are the same as in the plots of Fig. 5.3). It is clear from Fig. 5.12 that the scatter in the Larson-like velocity dispersion-size relation at low densities (purple points and error bar) is clearly contained within the estimated upper limit originating from the scatter in the $\mathcal{L}-\Sigma$ diagram. Instead, for intermediate column densities (green points and error bar), for which there is still a large enough number of points to obtain good statistics and the scatter in the $\mathcal{L}-\Sigma$ diagram is not large, we see that the upper limit to the scatter expected for $\sigma_{\rm v}$ is relatively small, and the points define a clear Larson-like linewidth-size relation. We conclude that the suggestion that clumps describe Larson-like relations when they are restricted to narrow column density ranges and they are close to energy equipartition is supported by our numerical clump sample.

5.4 Discussion

5.4.1 Limitations

As mentioned in Sec. 5.1.3, our numerical simulations have a number of limitations. In particular, our SPH simulations neglect all forms of stellar feedback and magnetic fields. We plan to perform a similar analysis in a future contribution including these physical agents, but our present study allows a first approximation to the problem. Furthermore, our chosen setups only produce objects similar to observed low-mass star-forming clumps and cores.

The neglect of stellar feedback has allowed us to investigate the energy budget of clumps due exclusively to the interaction of initial background turbulence and self-

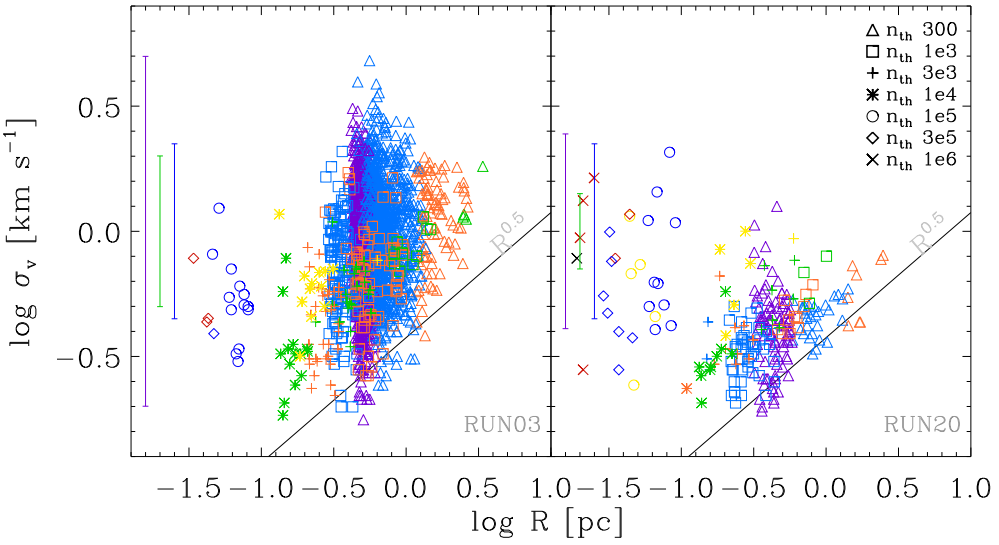

Figure 5.12: Larson velocity-size relation for clumps and cores in both simulations. Colors and symbols are the same as in Fig. 5.3. The error bars correspond to the scatter shown in Fig. 5.5, and their colors correspond to the Σ range.

gravity, without complicating the velocity field with additional contributions from the feedback. Our study has shown that in this context, our simulated clump sample reproduces observed trends in the $\mathcal{L} - \Sigma$ diagram. In our sample, gravity has an increasingly dominant role as the column density of the clumps increases. On the other hand, low-column density clumps are increasingly dominated by turbulence, although large-scale turbulent compressions are dominant in more than half of these objects, in which external turbulent compressions provide the initial "push" that triggers the assembly of the clumps. In these, gravitational contraction is expected to take over when the clump has grown sufficiently massive. The other half may actually correspond to clumps that will not grow to high densities and masses.

Magnetic fields, on the other hand, even if insufficiently strong to support the clouds, as they are presently believed to generally be (e.g., Crutcher, 2012), might possibly delay the collapses (Ostriker et al., 1999), or reduce the number or formation rate of collapsing objects (Vázquez-Semadeni et al., 2005; Nakamura & Li, 2007). This may affect the kinetic energies observed in the clumps, and we plan to repeat the present analysis in a future contribution including both feedback and magnetic fields. Nevertheless, the similarity of the distribution of clumps in our simulations in the $\mathcal{L} - \Sigma$ diagram to the observed one suggests that these agents may only play a secondary role during the assembly and early stages of collapse of clumps and cores.

5.4.2 Applicability to low- and high-mass regions

Strictly speaking, our results only apply to low-mass clumps and cores, since our sample does not include high-mass, high-column density (high-Σ) objects (see, e.g., the bottom panels of Fig. 5.4) similar to cluster- forming clumps, such as those studied by Fall et al. (2010). Nevertheless, because massive-star forming cores do appear to follow the same scaling in the $\mathcal{L}-\Sigma$ (e.g., Ballesteros-Paredes et al., 2011, 2018) diagram as MCs and the low-mass cores we have discussed in Sec. 5.3.2, we speculate that our results may apply to high-mass, high-Σ clumps. The clumps examined by Fall et al. (2010), which were selected for their star formation activity (not for their volume or surface density) have masses in the range $10^2 \lesssim M \lesssim 10^6 M_\odot$ and surface densities $\Sigma \sim 10^3 M_\odot \mathrm{pc}^{-2}$. They are currently experiencing strong stellar feedback that may counteract with their own self-gravity. The fact that these clumps have roughly constant column density may indicate that these values of Σ are physically selected by the requirement of exhibiting strong star formation and feedback. Column densities much higher than $\sim 10^3 M_\odot \mathrm{pc}^{-2}$ may not be observed because at that point gas removal from the clumps becomes important (Fall et al., 2010). On the other hand, at column densities lower than those values, the star formation activity may not be so strong (Zamora-Avilés et al., 2012; Zamora-Avilés & Vázquez-Semadeni, 2014), and the association between the gas and the stars may not be one-to-one because of the longer collapse timescales involved at lower densities (Burkert & Hartmann, 2013), and thus lower-column density objects will not be selected by a strong star formation activity criterion. Barnes et al. (2018) sample of high-mass clumps shows evidence of this result. It can be observed in their Fig. 14 that as the column density increases the accretion time decreases.

5.4.3 Comparison with previous work

Our results can be compared with those obtained in two recent papers that have performed numerical simulations of supernova (SN)-driven turbulence in the ISM, one in a (250 pc)^3 cubic box (Padoan et al., 2016, hereafter P+16), the other in a parallelepiped-shaped box of $1 \times 1 \times 40$ kpc^3, with a vertically stratified medium (Ibañez-Mejía , 2016, hereafter IM+16). In both cases, turbulence is driven for some time before turning on self-gravity. These two papers have arrived at opposite conclusions concerning the distribution of the simulated clouds in the $\mathcal{L}-\Sigma$ diagram: IM+16 find that the MC-like objects in their simulation develop near-equipartition after turning on self-gravity, while P+16 find that their clouds never approach equipartition, and instead have a roughly constant value of the ratio $\mathcal{L} \equiv \sigma_\mathrm{v}/R^{1/2}$,

independent of the column density Σ, suggesting that Larson's linewidth-size relation is valid after all, and equipartition is not. They also show that a sample of outer-Galaxy clouds (Heyer et al., 2001) appears to be consistent with this result.

The results from our initially random-driven, and subsequently decaying simulations support those of IM+16 but not those of P+16, since our clouds and clumps in general approach the equipartition state. Moreover, we find that equipartition is more tightly fulfilled at higher column densities, while low-column density objects exhibit larger kinetic energy excesses over equipartition, in agreement with observational data from various observational surveys (e.g., Barnes et al., 2011; Leroy et al., 2015). Nevertheless, the most massive of the low-column density objects are the ones closest to equipartition, suggesting that the motions are dominated by gravity.

The origin of the contrasting results between IM+16 and P+16, both from their respective simulations and from the observations each group considered, deserves further examination. Concerning the simulations, ample discussion has been given by IM+16, and here we just point out that the simulations of P+16 may suffer from significant over-driving of the turbulence. This is because they apply a standard value of the SN surface density rate (~ 100 Myr^{-1} kpc^{-2}) into their (250 pc)^3 numerical box. Although indeed most SN explosions are expected to occur within this vertical span around the Galactic midplane, the short height of the simulation box, which uses periodic boundaries, does not allow the energy injected by the SNe to escape to high altitudes, and to drive a galactic fountain, as it is known to do. Instead, this energy must remain within the small volume of the simulation, likely overdriving the turbulence in comparison with the actual observed levels in the ISM. For example, Figure 6 in P+16 shows that the mean whole-box velocity dispersion increases steadily from ~ 20 to $\sim 100\,\mathrm{km\,s^{-1}}$ during the last 10 Myr of evolution shown. However, Scannapieco et al. (2012, see also Gatto et al. 2015) have recently found that in simulations where the total velocity dispersion exceeds ~ 35 km s^{-1}, the medium goes into a thermal runaway regime where the gas is shocked into an unstable regime in which the cooling time increases strongly with temperature, causing a substantial fraction of the ISM to be unable to cool on a turbulence dissipation timescale. As a consequence, the medium goes into runaway heating, causing ejection of gas from any stratified medium. Since the simulation by P+16 lacks such stratification, the simulation is probably just heating up, explaining the continuous rise of the velocity dispersion, and justifying our interpretation that this simulation is overdriven and therefore not very realistic for the purpose of examining the energy budget of the clumps.

On the other hand, concerning the outer-Galaxy cloud data used by P+16, it is important to remark that these clouds have in general quite low column densities, in the range 10–100 $M_\odot$ pc^{-2}. Thus, they are indeed in the column density range where our simulations indicate that turbulence is still dominant (see Fig. 5.5), even if, as clouds grow, they may later transition to being dominated by self-gravity. In fact, the outer-Galaxy sample has been plotted by Leroy et al. (see Fig. 13 of 2015) together with data from several other surveys, and it can be seen that the outer-Galaxy clouds have the lowest-column densities and the largest scatter in the $\mathcal{L}$ parameter of the whole dataset, as with our results for the low-column density clouds in our simulations. Nevertheless, when one considers the whole dataset, including in particular objects of substantially larger column densities, the tendency towards equipartition is recovered, as shown in Figure 13 of Leroy et al. (2015) and our own Fig. 5.5. We therefore conclude that both the simulations and the data considered by P+16 are restricted to regimes where indeed turbulence is dominant (either by too strong turbulence driving or a low column density of the clouds), but that these do not represent the general trend in the Galactic ISM when a wide range of column densities is considered.

5.5 Summary and conclusions

In this work we have investigated the intrinsic (rather than derived from synthetic observations) physical conditions of clumps and cores in two SPH simulations of the formation and evolution of molecular clouds formed by converging motions in the warm neutral medium (WNM). The two simulations attempt to span a range of likely motions in this medium.

In both simulations, once the dense clouds form, they soon begin to contract gravitationally, and some time later (a few Myr) they begin to form stars, as in the general scenario described by Vázquez-Semadeni et al. (2007) and Heitsch et al. (2008). Neither of the simulations includes turbulence-driving stellar feedback nor magnetic fields, and so all of the kinetic energy is either driven by gravity or is a residual of the turbulent/compressive motions that initiated the formation of the clouds. Within this context of globally contracting molecular clouds (MCs), we have investigated whether the clumps within them follow the Larson scaling relations, or their generalization, as proposed by H09 and B11. We have also investigated the physical conditions in clumps that appear to have an excess of kinetic energy, in an attempt to understand the physical processes that cause this apparent over-virialization.

We created an ensemble of clumps in each simulation by defining clumps as connected sets of SPH particles above a certain density-threshold $n_{\rm th}$, so that a single clump at a lower threshold may contain several clumps at a higher value of $n_{\rm th}$. The objects defined at the highest thresholds ($n_{\rm th} \geq 10^5$ cm^{-3}) are refereed to as "cores".

Our results and conclusions may be summarized as follows:

- The full ensemble of clouds, clumps and cores does not follow either of the Larson scaling relations, but mostly follows their generalization, as proposed by H09 and B11. Nevertheless, low column density clumps in particular exhibit a large scatter, with a significant fraction of the clumps having values of the $\mathcal{L} \equiv \sigma_{\rm v}/R^{1/2}$ parameter of up to an order of magnitude larger than the virial value, similar to the situation in various observational studies.

- We noted that, as emphasized by B11, the kinetic energy implied by free-falling motions is only a factor of $\sqrt{2}$ larger than that for virial equilibrium. We therefore generically refer to this condition as "energy equipartition".

- In our simulations, the equipartition condition is due to gravitational contraction, by construction.

- The clumps defined at a single threshold $n_{\rm th}$ do not exhibit density-size or velocity dispersion-size relations. Instead, they exhibit nearly constant volume density, in agreement with previous studies (Ballesteros-Paredes & Mac Low, 2002). However, ensembles of clumps that exhibit near-equipartition and that are selected by column density ranges, do exhibit Larson-like relations, suggesting that these relations are special cases of the more general equipartition condition.

- We find examples of clouds, clumps and cores that exhibit excess kinetic energies over the equipartition level at both low- and high-column densities. Low-column density clumps that exhibit this excess are the least massive, while the more massive ones are closer to equipartition. Moreover, for more than 50% of the low-density clumps with an $\mathcal{L}$ excess in both simulations, the velocity field in the clouds appears to be convergent (i.e. have negative net divergence). This suggests an evolutionary process in which a turbulent compression initially dominates the kinetic energy and exceeds the gravitational energy of the forming cloud. However, as the cloud becomes denser and more massive, the gravitationally-driven velocity becomes dominant. Also, this suggests that

the observation of an excess kinetic energy does not necessarily imply that a clump will disperse or needs an external thermal confining pressure to avoid dispersal. The excess kinetic energy may simply reflect the initial compressive motions within the clump. In this case, instead of *confinement* of the cores by thermal pressure, we have *assembly* by ram pressure.

- Some of the high-column density cores that exhibit kinetic energy excesses contain stellar particles that increase the total gravitational potential in the volume of the clump. When this stellar mass is added to the gas mass in the energy budget of the core, the gas+stars system returns to near equipartition.

- Some high-column density clumps with kinetic energy excesses, however, do not contain stellar particles, so that the above correction cannot be applied. Investigation of the velocity field in these cases does show a rotating and/or expanding motion, so that these objects are in the process of being disrupted, and will not form stars. Because this process is occurring at high densities, the driver of these disrupting motions is likely to be the turbulence generated by the large-scale collapse.

- We also investigated the possibility that excess kinetic energies in high-column density cores might be due to the cores being located in filamentary clumps, with net accretion from the filament onto the core, so that the velocity dispersion in the cores might represent the gravitational potential of the mass in the filament. However, this mechanism does not seem to be operational. We find that the filaments and their embedded cores begin their evolution roughly simultaneously, accreting material from the cloud mostly perpendicularly to the filament. Accretion from the filament onto the core begins later, when the core has become more massive and has already started to form stars. Thus, cores that are actively accreting from their parent filaments are already in advanced star-forming stages, and do not correspond to pre- or early protostellar objects.

Chapter 6

Simultaneous evolution of the virial parameter and star formation rate in star forming molecular clumps.

In this chapter[1], we examine the evolution of the virial parameter, α, and the star formation activity of a star forming region in a numerical simulation without stellar feedback and two observational samples likely to be at different evolutionary stages, the Pipe and the G14.225 clouds. We start by recalling the recent results on the expected evolution of the so called *Larson ratio* $\mathcal{L} \equiv \sigma_{\rm v}/R^{1/2}$ and the virial parameter for cores that decouple from the global flow and begin to contract at a finite radius R_0, which imply that these parameters evolve during the core's contraction in a manner that depends on the initial ratio of the inertial (or *external*) to the gravitational components of the compressive motions that form the core, approaching the virial values as collapse proceeds and the inertial motions become subdominant. We search for a region in the simulation with physical properties similar to those of the filamentary structure in G14.225 and observe that early in its evolution, it may have physical properties similar to those of the substructure in the Pipe cloud. We follow the evolution from the "Pipe-like" to the "G14.225-like" stage. We find that the star formation rate and star formation efficiency increase monotonically as the region evolves during the time interval we study. Thus, we propose that the energy balance, the virial parameter and the star formation rate determine the evolutionary stage of a star forming region, and that a star forming region like the Pipe will evolve

[1]This chapter is a paper to be submitted, in collaboration with E. Vázquez-Semandeni, A. Palau, G. Busquet and Manuel Zamora-Avilés.

to a G14.225-like stage, in the course of a few megayears. The increase of $\mathcal{L}$, α and the star formation activity during the clump's evolution is consistent with the recently proposed scenario of hierarchical gravitational collapse and fragmentation for molecular clouds and their substructure.

6.1 Introduction

One of the most studied parameters of molecular cloud (MC) structure is the so-called *virial parameter* α, defined as the ratio of twice the kinetic energy to the gravitational energy for a uniform-density sphere (Bertoldi & McKee, 1992),

$$\alpha \equiv \frac{2\mathrm{E_k}}{|\mathrm{E_g}|} = \frac{5\sigma_\mathrm{v}^2 R}{GM}, \tag{6.1}$$

where σ_v is the average one-dimensional velocity dispersion along the line of sight, R is the characteristic radius of the cloud, and M is its mass.

The standard notion of MCs is that they are quasi-virialized structures, in which their self-gravitational energy is globally balanced by the turbulent energy (e.g., Larson, 1981; Mac Low & Klessen, 2004; McKee & Ostriker, 2007; Ballesteros-Paredes et al., 2007; Heyer et al., 2009)[2]. In this case, the virial parameter of MCs in general should be ~ 1. Observationally, however, the virial parameter of MCs and their substructures (parsec-scale clumps and 0.1-pc scale cores) appears to be significantly larger than unity for clumps of low column density or low mass, and to decrease systematically to values smaller than unity for objects of higher column density, or higher mass (e.g., Kauffmann et al., 2013; Leroy et al., 2015; Liu et al., 2015; Ohashi et al., 2016; Sanhueza et al., 2017; Contreras et al., 2018; Traficante et al., 2018; Louvet et al., 2018).

The large values of α (significantly larger than unity) observed in clouds of low column densities or masses are often interpreted in terms of the presence of a large external confining pressure ($\mathrm{P}/k_\mathrm{B} \sim 10^4$–$10^6$ K cm^{-3}; e.g., Keto & Myers, 1986; Field et al., 2011; Leroy et al., 2015; Traficante et al., 2018), although it is hard to imagine that such high pressures can be thermal in general, since the mean ambient thermal pressure in the ISM is rather low, $\sim 3 - 4 \times 10^3$ K cm^{-3}, and large deviations from it occur very infrequently (e.g., Boulares & Cox, 1990; Jenkins, 2004; Jenkins, & Tripp, 2011). Instead, it is most likely that these values correspond to ram pressure,

[2]Magnetic support has recently lost appeal because it now appears that MCs tend to be generally magnetically supercritical, and thus cannot be globally supported by magnetic fields (e.g., Crutcher, 2012)

in which case they imply mass, momentum and energy flux across Eulerian cloud boundaries, or a displacement of Lagrangian boundaries (Ballesteros-Paredes et al., 1999; Banerjee et al., 2009). Indeed, in a previous study (Camacho et al., 2016), we have found, through measurement of the mean velocity divergence within the clouds in numerical simulations of cloud formation and evolution, that roughly half the clouds with an excess of kinetic energy are undergoing compression. This can be interpreted as the clouds being subject to a *ram* pressure that is making them denser and smaller, so that they eventually will become gravitationally bound. The origin of this ram pressure can be large scale turbulence, a large scale potential well or other instabilities. Furthermore, one important possibility is that clouds may be falling into the potential well of the stars. Thus, this is not really a "confinement", since the clouds are not at rest. The same goes for the other half of the clouds, which are undergoing expansion. In this case, the excess kinetic energy corresponds to the expansion motions, and again the cloud is not confined, so there is no need for a high confining pressure. In Camacho et al. (2016) and Ballesteros-Paredes et al. (2018, hereafter BP+18) it has been suggested that, for clouds formed by turbulent (inertial) compressions originated by large scale turbulence, a larger scale potential well or other instabilities in the background medium (Ballesteros-Paredes et al., 1999), and which gradually become more strongly gravitationally bound, while the inertial compressive motions decay or dissipate, the kinetic energy transits from being dominated by the inertial motions to being dominated by the gravitationally-driven motions. In that case, an initial decay of the Larson ratio and the virial parameter may be expected.

On the other hand, values of α smaller than unity have been interpreted as either being in a state of collapse and/or support from strong magnetic fields (e.g., Kauffmann et al., 2013; Liu et al., 2015; Ohashi et al., 2016; Sanhueza et al., 2017; Contreras et al., 2018). However, BP+18 recently proposed that values of $\alpha < 1$ may be expected in cores that have just recently decoupled from the general cloud flow and begun to collapse locally if the initial inertial motions are also smaller than the virial value. This can be seen by assuming that the nonthermal contribution to the velocity dispersion, $\sigma_{\rm nth}$, consists itself of two contributions, one being a gravitationally-driven infall velocity $\sigma_{\rm g}$, and the other a truly turbulent (or inertial; i.e., not consisting of infall motions) component, $\sigma_{\rm t}$, so that

$$\sigma_{\rm nth}^2 = \sigma_{\rm g}^2 + \sigma_{\rm t}^2. \tag{6.2}$$

Next, BP+18 pointed out that, when a core of fixed mass M begins to contract

locally, it does so from a finite radius R_0. Thus, its gravitationally-driven speed at a later, smaller radius R is given by

$$\sigma_{\rm g} = \sqrt{2\eta GM\left(\frac{1}{R} - \frac{1}{R_0}\right)}, \tag{6.3}$$

where η is a factor of order unity that depends on the geometry and mass distribution of the core. As a consequence, the contribution of $\sigma_{\rm g}$ to the so-called *Larson ratio* $\mathcal{L} \equiv \sigma_{\rm v}/R^{1/2}$ in this fixed-mass core scales with column density as

$$\mathcal{L}_{\rm g} = \sqrt{\pi\eta G\Sigma\left[1 - \left(\frac{\Sigma_0}{\Sigma}\right)^{1/2}\right]}, \tag{6.4}$$

while its contribution to the virial parameter scales as

$$\alpha_{\rm g} = 2\left[1 - \left(\frac{\Sigma_0}{\Sigma}\right)^{1/2}\right], \tag{6.5}$$

where Σ_0 is the column density of the core when it began its contraction.

On the other hand, simultaneously with the variation of $\sigma_{\rm g}$ with column density as the core collapses, BP+18 assumed that the inertial contribution to the Larson ratio and the virial parameter decreases by dissipation during the compression at two different plausible rates. Thus, the total value of $\mathcal{L}$, obtained in quadrature from the gravitational and the inertial contributions, may adopt a variety of shapes depending on the initial ratio of the two contributions, as shown in Fig. 1 of BP+18.

Another representation of the total virial parameter can be inferred from eqs. (6.1) and (6.2). From this, it follows that $\alpha = R(\sigma_t^2 + \sigma_g^2)/2\eta GM$. Thus, according to Eq. (6.3), the virial parameter is

$$\alpha = 2\left[\frac{\sigma_{\rm t}^2 R}{\eta GM} + \left(1 - \frac{R}{R_0}\right)\right]. \tag{6.6}$$

In this equation the first term can be recognized as the common definition of the virial parameter, while the second term represents the gravitational contribution that depends on size.

It is important to note that, in the above treatment, a Lagrangian definition of the core was used, so that, by construction, the core has a constant mass, and thus this simple calculation cannot predict a dependence of the virial parameter with mass. However, if the core is instead defined in terms of a density or column-density

threshold, as is standard for cores defined in terms of molecular-line tracers and common in numerical simulations (e.g., Vázquez-Semadeni et al., 1997; Ballesteros-Paredes & Mac Low, 2002; Galván-Madrid et al., 2007; Naranjo-Romero et al., 2015; Camacho et al., 2016; Ibañez-Mejía , 2016), then the mass of a gravitationally contracting core increases with time together with its column density (Naranjo-Romero et al., 2015). Thus, we expect the virial parameter of populations of cores defined by molecular-line tracers to depend on mass as well.

At this point, it is important to point out that this kind of evolution occurs in the scenario of Global Hierarchical Collapse (GHC), in which cores begin to collapse locally within a larger cloud that is itself Jeans unstable as well, so that the evolution consists of a multi-scale, hierarchically nested, sequence of collapses. (Vázquez-Semadeni et al., 2009; Naranjo-Romero et al., 2015; Vázquez-Semadeni et al., 2017, 2019). This is important in order to allow accretion from the clump onto the core (Naranjo-Romero et al., 2015). In this scenario, the star formation rate (SFR) of the clouds and their substructure also increases as the cloud globally contracts, until the feedback from massive stars, which appear late (after ~ 5 Myr) in the evolution of the cloud, begins to destroy it, either by dispersing or evaporating the dense gas. At this point, the cloud's SFR begins to decrease again (Zamora-Avilés et al., 2012; Zamora-Avilés & Vázquez-Semadeni, 2014; Lee et al., 2016; Vázquez-Semadeni et al., 2017, 2018; Caldwell & Chang, 2018).

Ballesteros-Paredes et al. (2018) showed that, in isothermal numerical simulations of driven turbulence at the parsec scale, the Larson ratio of cores evolves in the $\mathcal{L}$ *vs.* Σ diagram. In the present chapter, we show this evolution, as well as that of the virial parameter, in a larger-scale, multi-phase simulation (of size 256 pc) of giant molecular cloud formation and subsequent collapse, and show that it occurs simultaneously with an evolution of the star formation activity of the cores. We also search for the signature of this simultaneous evolution of the virial parameter and the SFR in observational data by comparing the location of the simulated cores and those in star-forming regions of presumably different evolutionary stages, in $\mathcal{L}$ *vs.* Σ and α *vs.* M diagrams, and show that there is good qualitative agreement, thus supporting the evolutionary nature of the GHC scenario for molecular clouds.

The plan of the chapter is as follows. In section 6.2 we briefly describe the simulation and the data from the literature. Next, Section 6.3 shows the procedure to derive the physical parameters for both the numerical and the observational data. The results about the evolution and the energy budget for both samples are reported in section 6.4. Finally, we present some discussion in section 6.5 and a brief summary in section 6.6.

6.2 Data

6.2.1 Observational data

As described in Sec. 6.1, in order to search for evolutionary effects in clouds, we select two regions likely to be in different evolutionary stages. According to the model of Zamora-Avilés & Vázquez-Semadeni (2014, see also Vázquez-Semadeni et al. 2018), this evolution should manifest itself in different values of the cloud's star formation rate and efficiency. Thus, we consider the Pipe Nebula (Alves et al., 2007; Rathborne et al., 2008; Lada et al., 2008), a quiescent dark cloud, and G14.225-0.506 (Busquet et al., 2013; Lin et al., 2017), an infrared dark cloud (IRDC) showing active star formation (Povich et al., 2016).

The Pipe Nebula has been studied in both dust extinction (e.g., Lombardi et al., 2006; Alves et al., 2007; Román-Zúñiga et al., 2010; Ascenso et al., 2013) and molecular line emission ($C^{18}O$, NH_3, CCS, HC_5N; e.g., Muench et al., 2007; Rathborne et al., 2008; Frau et al., 2010). It is located at a distance of 130 pc (Lombardi et al., 2006; Frau et al., 2012), and has a mass $\sim 10^4 M_\odot$ and a size $\sim 3 \times 14$ pc. A large population of dense cores has been identified in this cloud with masses 0.2–$20 M_\odot$ (Rathborne et al., 2008). We select the sample of the cores with NH_3 emission .

IRDC G14.225-0.506 (hereafter G14 for short; Busquet et al., 2013), is part of a large molecular cloud which is actively forming stars (Povich & Whitney, 2010; Busquet et al., 2016; Chen et al., 2019; Shimoikura et al., 2019, and references therein). G14 has a mass $\sim 1.9 \times 10^4 M_\odot$ (Lin et al., 2017), size $\sim 4.7 \times 8.7$ pc Busquet et al. (2013), and is located at a distance ~ 1.98 kpc (Jaffe et al., 1981, 1982; Xu et al., 2011). In Busquet et al. (2013, hereafter B+13), a study of this cloud was presented in the NH_3 (1,1) and (2,2) lines, resulting from a combination of Very Large Array (VLA) and Effelsberg 100 m telescope observations. We refer the reader to B+13 for details on the observations and data reduction. In addition, for consistency with the available data from the Pipe Nebula, the FIR/submm-derived column density map towards the G14 cloud was also considered (Lin et al., 2017). The dust emission map is the result from a combination of ground-based and space telescope observations resulting in a synthesized beam of $\sim 10''$ angular resolution, which is comparable to the resulting synthesized beam of NH_3 in B+13, $\sim 8'' \times 7''$.

We assume that these two clouds represent different stages of molecular cloud evolution, due to their different levels of star formation activity, as proposed in Vázquez-Semadeni et al. (2018), so that they can be compared to different temporal snapshots of the simulation (Sec. 6.4.2).

6.2.2 Numerical simulation

We analyze a numerical simulation of decaying turbulence that represents the formation and evolution of molecular clouds in the warm neutral medium. This simulation, hereafter RUN03, has been studied in previous works (Heiner et al., 2015; Camacho et al., 2016) and was developed with the GADGET-2 code in a box of 256 pc per side containing $296^3 \approx 2.6 \times 10^7$ SPH particles. It was initialized with a turbulent driver during the first 0.65 Myr applied at scales from 1 to 1/4 of the numerical box size, reaching a velocity dispersion $\sim 18\,\mathrm{km\,s^{-1}}$ which was then left to decay. It also includes a prescription for the formation of sink particles (Heiner et al., 2015, for details). These initial conditions result in a clumpy medium where the dense fluctuations begin to accrete gravitationally from their surroundings, growing in mass and density. This simulation was evolved for a total of ≈ 34 Myr.

6.3 Sample definition and selection

In order to meaningfully compare the numerical and the observational data, we need to carefully select the region to be studied in the simulation and, for the observations, to ensure consistency between the two datasets. In the simulation, we choose to study a single star-forming region at various times in order to determine its energy budget evolution. The region was studied using various density thresholds to define its internal structure, in order to explore objects from the scale of molecular clouds to that of dense cores. For the observational data, we select for both samples those clumps with available ammonia-data (to obtain the velocity dispersion) and the extinction map data (to obtain the mass).

6.3.1 The Pipe sample

The Pipe Nebula has more than a hundred identified dense cores (Lada et al., 2008). Because line emission measurements provide the kinematic information, in this work we select, from the original sample, the cores that have been detected in NH_3 (Rathborne et al., 2008), from which the velocity dispersion is obtained. The mass of these cores is reported in Lada et al. (2008), and spans a range of $\sim 0.5 - 20\ M_\odot$.These masses have been determined from the extinction maps, as is the size, which has been computed assuming spherical geometry given the area in the plane of the sky, so that $R = (A/\pi)^{1/2}$ (Lada et al., 2008). The range in size for the selected cores is $\sim 0.06 - 0.3$ pc and the mean density of the cores is $\sim 7 \times 10^3\,\mathrm{cm^{-3}}$ (see Table 2 of

Pipe sample							
ID[a]	R[b] (pc)	M[a,b] ($M_\odot$)	$\sigma^{a,c}_{v,1D}$ (km s^{-1})	ID[a]	R[b] (pc)	M[a,b] ($M_\odot$)	$\sigma^{a,c}_{v,1D}$ (km s^{-1})
6	0.12	3.14	0.09	65	0.06	0.72	0.26
7	0.14	4.69	0.08	70	0.08	1.14	0.23
8	0.12	3.26	0.11	87	0.17	10.3	0.14
12	0.23	20.3	0.15	89	0.09	1.36	0.10
14	0.17	9.73	0.14	91	0.07	1.09	0.07
15	0.12	2.64	0.18	92	0.09	1.61	0.19
17	0.07	0.69	0.25	93	0.12	3.55	0.17
20	0.11	2.28	0.17	97	0.18	5.86	0.21
22	0.08	1.01	0.12	101	0.08	1.87	0.09
23	0.16	1.87	0.07	102	0.19	6.71	0.24
25	0.09	1.10	0.20	108	0.08	0.78	0.16
40	0.19	9.23	0.10	109	0.12	3.63	0.08
41	0.08	1.08	0.12	113	0.10	2.39	0.06
42	0.09	2.79	0.11	132	0.15	4.67	0.18
47	0.09	1.41	0.14				

Table 6.1: Physical properties for the selected sample of the Pipe cores. a) Rathborne et al. (2008), b) Lada et al. (2008) c) $\sigma_{v,1D}$ from the $NH_3(1,1)$ emission.

Rathborne et al., 2008). We use the data reported in these works for our analysis. The table 6.1 shows the data for the selected sample.

6.3.2 The G14 sample

In the case of G14 data, we create a clump ensemble directly from the NH_3 maps. For this task, we use the `dendrogram`[3] algorithm (Sec. 4.1.1), which allows following the hierarchy of embedded structures like we do in the simulation data (see description in Sec. 6.3.3). In B+13, two classes of objects: filaments and hubs, are recognized. The former were identified in the $NH_3(1,1)$ map, while the latter were identified in the $NH_3(2,2)$ map, and correspond to the sites where filaments converge. This indicates that the hubs have larger typical densities than the filaments. It is noteworthy however, that their "hubs" actually still exhibit elongated morphologies.

In this work, we aim to emulate the classification of B+13 but we define three classes of objects: filaments, clumps and dense cores[4]. Our filaments roughly coincide with those defined in B+13; our clumps include two classes of objects: the hubs from B+13 as well as some isolated roundish clumps away from the filaments;

[3]This research made use of astrodendro, a Python package to compute dendrograms of Astronomical data (`http://www.dendrograms.org/`)

[4]We refrain from using the name "hub" in order to avoid confusion.

finally, our dense cores correspond to the densest, roundish regions within B+13's hubs.

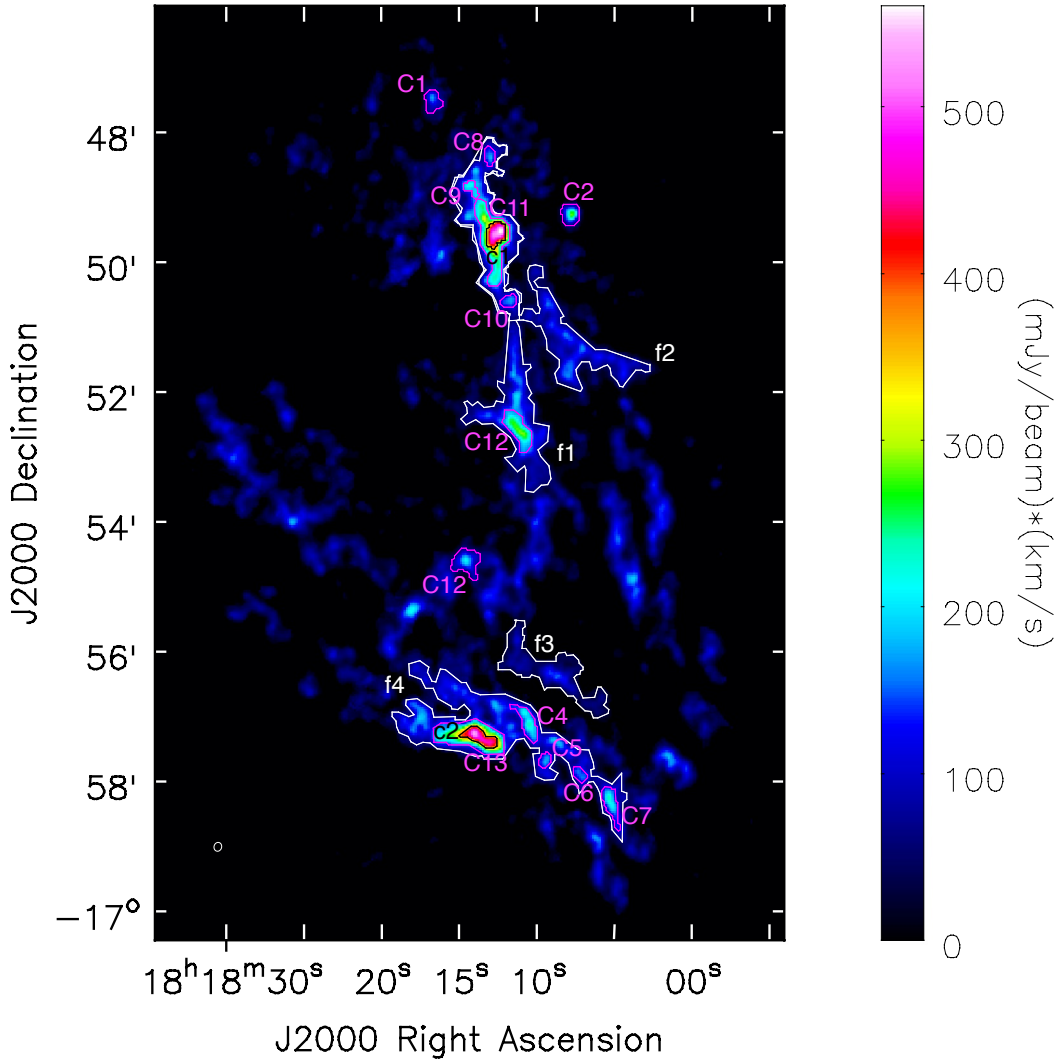

Figure 6.1: G14 moment-0 map of the $NH_3(1,1)$ inversion transition taken from Busquet et al. (2013). Contours show the objects of study in this work, the different colors denote the filaments-f (white), clumps-C (magenta) and dense cores-c (black). They have been obtained using the `dendrogram` package.

Our objects are identified in the ammonia data choosing different sets of values of the input parameters in the `dendrogram` algorithm. The rms noise of the NH_3 map in G14 is 8 mJy/beam/km s^{-1}. B+13 defined the lowest contour level at 3 times the rms noise; thus, we set the noise parameter in the dendrogram algorithm to $\sigma = 3\,\mathrm{rms}$. The equivalent area of the beam is ~ 12 pixels (~ 0.1 pc). Then, we consider a minimum number of pixels of `min_pix` $= 15$, in order to have structures

G14 sample							
ID[a]	R[b] (pc)	M[c] ($M_\odot$)	$\sigma^{d}_{v,1D}$ (km s^{-1})	ID[a]	R[b] (pc)	M[c] ($M_\odot$)	$\sigma^{d}_{v,1D}$ (km s^{-1})
C1	0.079	8.519	0.437	C11	0.191	214.234	0.955
C2	0.084	7.828	0.471	C12	0.124	47.156	0.556
C3	0.109	22.760	0.522	C13	0.213	204.163	0.972
C4	0.107	20.686	0.803	c1	0.092	80.153	0.892
C5	0.054	6.169	0.773	c2	0.099	66.107	0.981
C6	0.056	6.494	0.573	f1	0.511	636.414	1.096
C7	0.096	21.406	0.544	f2	0.488	648.723	0.811
C8	0.057	6.741	0.437	f3	0.274	98.919	0.582
C9	0.056	8.163	0.561	f4	0.509	574.053	1.333
C10	0.060	8.784	0.790				

Table 6.2: Physical properties for the G14 sample. `a)` The IDs in this table correspond to the labeled objects in Fig. (6.1). `b)` The size was computed from the area A defined with the `dendrogram` package, $R = (A/\pi)^{1/2}$. `c)` Mass is computed as $M = 2.8\ m_{\rm h}\ N(\rm H_2)\ A$, considering the $N(\rm H_2)$ map from Lin et al. (2017). `d)` $\sigma_{v,1D}$ was obtained from the $\rm NH_3(1,1)$ emission.

larger or equal to the beam. Finally, we vary the input parameters by means of `min_value` $= \mathtt{n_v}\sigma$ and `min_delta` $= \mathtt{n_d}\sigma$ (c.f. Sec. 4.1.1). Where $(\mathtt{n_v}, \mathtt{n_d}) = (1, 1)$ for the filaments, (5, 1) for the clumps, and (15, 3) for the dense cores.

Figure 6.1 shows the three main families that have been selected, the filaments (white) labeled with an "f", the clumps (magenta) labeled with a"C", and the dense cores (black) labeled with a "c".

We use the CASA[5] (McMullin et al., 2007) software to extract the spectra in the PPV cubes for the (1,1) and (2,2) $\rm NH_3$ transitions to the contours defined with the dendrograms. For these objects, the one-dimensional velocity dispersion was directly computed as $\sigma_{\rm v} = \sqrt{3}\ \mathrm{FWHM}/2\sqrt{2\ln 2}$, where FWHM is the full width at half maximum obtained from the fit to the hyperfine structure of $\rm NH_3(1,1)$, performed with the standard CLASS method within the GILDAS[6] software. Table 6.2 shows the properties derived for the sample in G14.

Note that, in principle, we could derive the mass of the clumps in G14 directly from the line data for the (1,1) and (2,2) $\rm NH_3$ transitions. However, for consistency with the core data from the Pipe Nebula, whose mass estimate was derived with the dust extinction map, we consider the column density map from Lin et al. (2017) to compute the masses within the contours defined in the ammonia maps with the `dendrogram` algorithm, as described above, assuming that the two sets of observa-

[5] https://casa.nrao.edu/
[6] http://www.iram.fr/IRAMFR/GILDAS

tions trace the same gas. In this way we have for both clouds the mass derived from dust emission and the velocity dispersion obtained from the NH_3 emission. Figure 6.2 shows the mass and size of the objects selected in both the Pipe and G14 clouds.

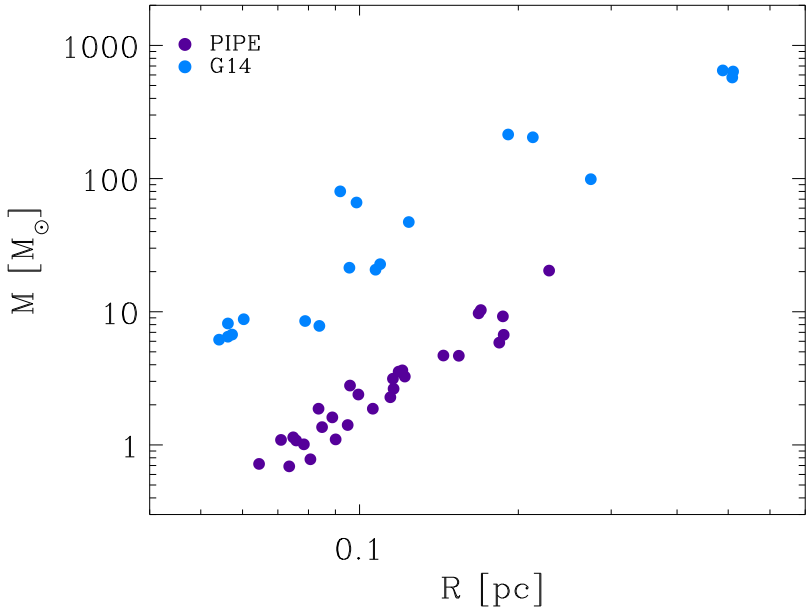

Figure 6.2: Size-mass relation for the selected sample of the Pipe cloud (purple) and the G14 cloud (blue).

6.3.3 The numerical sample

In the simulation, several star forming regions are formed from the collapse of the density fluctuations present in the clouds. As the parent cloud collapses, its mean Jeans mass decreases. Then, dense turbulent fluctuations collapse once they exceed their Jeans mass and quickly start forming stellar particles (Girichidis et al., 2014; Zamora-Avilés & Vázquez-Semadeni, 2014; Vázquez-Semadeni et al., 2019). Thus, most of them reach a high star formation activity in a short time. At these stages, feedback should have important effects, affecting the kinematics around the clumps and reducing the SFR if it were included. However, it is not considered in the simulation. Thus, to avoid objects that should already be affected by feedback, possibly in the process of dispersal, we search for a star forming region in an intermediate time interval in the simulation ($\approx 18 - 23$ Myr) such that the simulation has dissipated enough kinetic energy from the initial turbulent fluctuations in order to have realistic velocity dispersion values, and does not yet have too high a star formation activity at late stages, due to the absence of feedback.

Furthermore, for the object selection in the available period, we look for a clump that meets the following conditions: *a)* To be a single coherent object in the 3D space and not just a random superposition in projection and to remain so over a few million years. *b)* To show not too high star formation efficiency. For the entire cloud we tolerate an SFE $\sim 20\%$. *c)* Not to be located near the edges of the box to allow a straightforward identification of the objects without cross boundary complications. The requirements mentioned here restrict the number of objects that can be analyzed. Moreover, the cores evolve rapidly in comparison to the time interval between snapshots, $\Delta t = 0.133$ Myr. Therefore, the cores become larger, denser and more massive within a few snapshots.

We selected from the simulation a clump that fulfills the above criteria. We refer to it simply as "the numerical clump". This cloud was followed over a timespan ~ 1.6 Myr, from 20.58 to 22.18 Myr. The initial time was selected as the time when cores above a threshold $n_{\rm th} = 5 \times 10^3\,{\rm cm}^{-3}$ first appear in this region. During the above timespan, the clump evolves from having cores (defined at $n_{\rm th} = 5 \times 10^3\,{\rm cm}^{-3}$) that are similar to the dense cores in the Pipe, to containing substructures (filaments and dense cores) similar to those in G14, and changes in shape, size, mass, and mean and maximum density (Fig. 6.3 and 6.4).

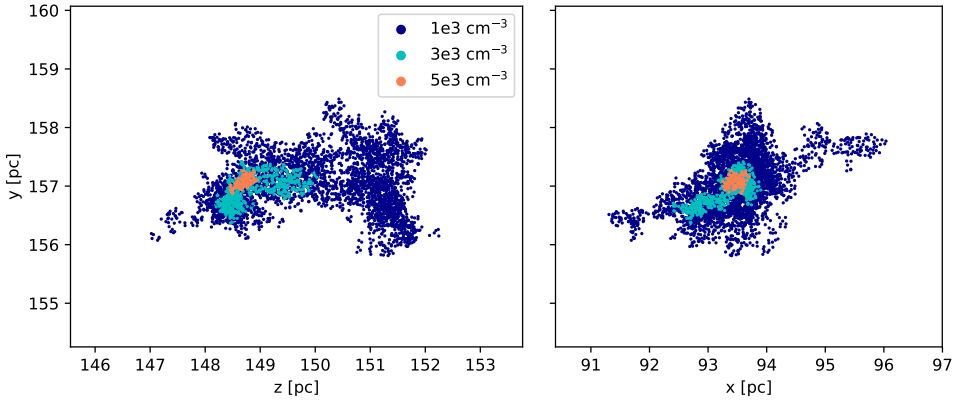

Figure 6.3: Pipe-like core (orange, $n_{th} = 5 \times 10^3\,{\rm cm}^{-3}$) and the numerical clump at lower densities at $t = 20.58$ Myr. At this stage the dense core is comparable to a Pipe core.

To define different categories of objects like filamentary clumps, hubs and dense cores, we consider density thresholds similar to the mean densities of the corresponding objects in the observed clouds. For the Pipe-like stage of the numerical clump, we recall that the more massive cores in the Pipe cloud have masses from $\sim 5 - 20 M_\odot$, sizes of ~ 0.2 pc, and densities of $\sim 7 \times 10^3\,{\rm cm}^{-3}$. We thus define the numerical clump by a threshold $n_{\rm th} = 10^3\,{\rm cm}^{-3}$ and a Pipe-like core at $n_{\rm th} = 5 \times 10^3\,{\rm cm}^{-3}$.

With these thresholds, the numerical clump has projected dimensions of $\sim 3 \times 5$ pc, and contains one roundish core of size ~ 0.2 pc, mass 6.3 $M_\odot$, and mean density $\sim 6500\,\mathrm{cm}^{-3}$, in good agreement with the typical Pipe core. At $n_{\rm th} = 10^3\,\mathrm{cm}^{-3}$ the numerical clump roughly corresponds to a clump ($M \sim 230\ M_\odot$) within the observed Pipe cloud.

For the G14-like stage, we define the filament at $n_{\rm th} = 10^3\,\mathrm{cm}^{-3}$, clumps at $n_{\rm th} = 10^4$, and dense cores at $n_{\rm th} = 10^5\,\mathrm{cm}^{-3}$, which is comparable to our data in ammonia.

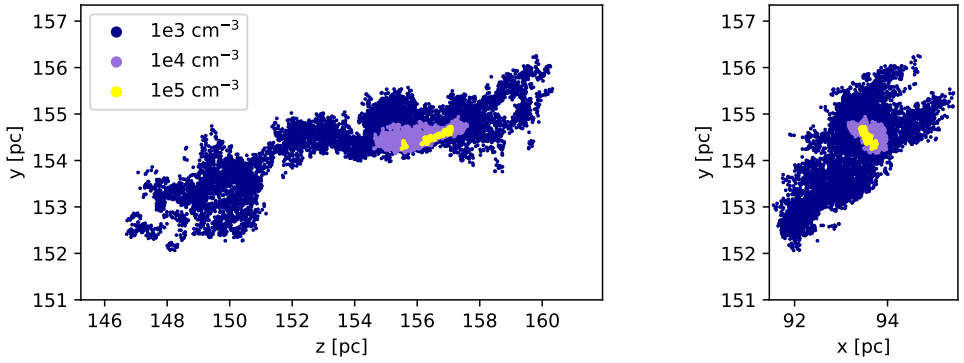

Figure 6.4: The numerical clump at an advanced stage, $t = 22.18$ Myr. At this time, it can be compared with the filamentary structure in G14.

For the structures thus identified, we compute the mass as $M = nm_{\rm sph}$, where n is the total number of particles belonging to the clump and $m_{\rm sph}$ is the mass of an SPH particle ($m_{\rm sph} = 0.06\,M_\odot$); the size as $R = (3V/4\pi)^{1/3}$, where V is the total volume of the particles;[7] the column density as $\Sigma = M/\pi R^2$; the Larson ratio $\mathcal{L} = \sigma_{v,1D}/R^{1/2}$; and the virial parameter. The latter is computed in the standard form eq. (6.1). We also estimate the star formation rate as SFR $\approx \Delta M_*/2\Delta t$, where ΔM_* is the mass that is transformed into sink particles during the time interval $2\Delta t$, and Δt is the time between snapshots. The mass of the sink particles is not constant, since they accrete material from the surroundings as the simulation evolves. Thus, ΔM_* includes the mass in new sinks as well as the mass accreted by existing sinks. Finally, the star formation efficiency at any instant in time t is computed as $\mathrm{SFE}(t) = M_*(t)/\left[M_{\rm gas}(t) + M_*(t)\right]$.

[7] The total volume is the sum of the specific volumes of all particles, see Camacho et al. (2016) for details.

6.4 Results

Observations from molecular clouds to dense cores in $\mathcal{L} - \Sigma$ diagrams have shown objects below or above the energy equipartition, where the deviations have been explained assuming unbound clouds, external pressure confinement or turbulence regulation (Heyer et al., 2009; Field et al., 2011; Traficante et al., 2018). In the present work we offer a different interpretation for the sub-virial cores through the study of the temporal evolution of the numerical clump.

6.4.1 The numerical clump sample

The energy balance in the numerical clump sample is studied in the $\mathcal{L} - \Sigma$ diagram (top panels of Figs. 6.5 and 6.6). The evolution of the virial parameter α is shown in the bottom panels. In addition, in these figures the symbols are colored according to the SFE (Fig. 6.5) and the SFR (Fig. 6.6). In the $\mathcal{L} - \Sigma$ diagram, we refer to the line $\mathcal{L} = \sqrt{G\Sigma}$ as the "virial line", and to the line $\mathcal{L} = \sqrt{2G\Sigma}$ as the "free-fall line" (Ballesteros-Paredes et al., 2011). Since these two lines are so close to each other, we collectively refer to both as "the equipartition condition". Note that they correspond to values of the virial parameter of $\alpha = 1$ and $\alpha = 2$, respectively. We refer to the region above energy equipartition "super-virial" and to the region below, as "sub-virial".

The various lines correspond to the density thresholds used to define the substructure in the numerical clump, joining objects defined by the same density threshold. These can be thought of as objects seen in tracers with different critical densities. Thus, the time evolution for an object at a certain density can be seen by following the connected symbols from left to right. We observe in the simulation that denser objects, and eventually stars, appear later in the evolution of the clump. Because of this, we label the beginning of each curve with the time $t_{i,n}$ when the objects first apear at $n_{\rm th}$. In fact, it is noteworthy that the first stars appear in the clump approximately one free-fall time of the clump at the time when we first observe it. Indeed, at that time ($t_0 = 20.58$ Myr), the clump's mean density is $\sim 2.35 \times 10^3$ cm^{-3}, for which the free-fall time $t_{\rm ff} = \sqrt{3\pi/(32G\rho)}$ is ≈ 0.95 Myr. On the other hand, the first sink appears 1.06 Myr after t_0, in very good agreement with the value of $t_{\rm ff}$, considering that the actual collapse is always slightly slower because thermal pressure is not totally negligible (Larson, 1969). This shows that the clump is evolving essentially under the action of its own self-gravity.

There are some important features to notice in the $\mathcal{L}-\Sigma$ diagrams: *i)* the earliest

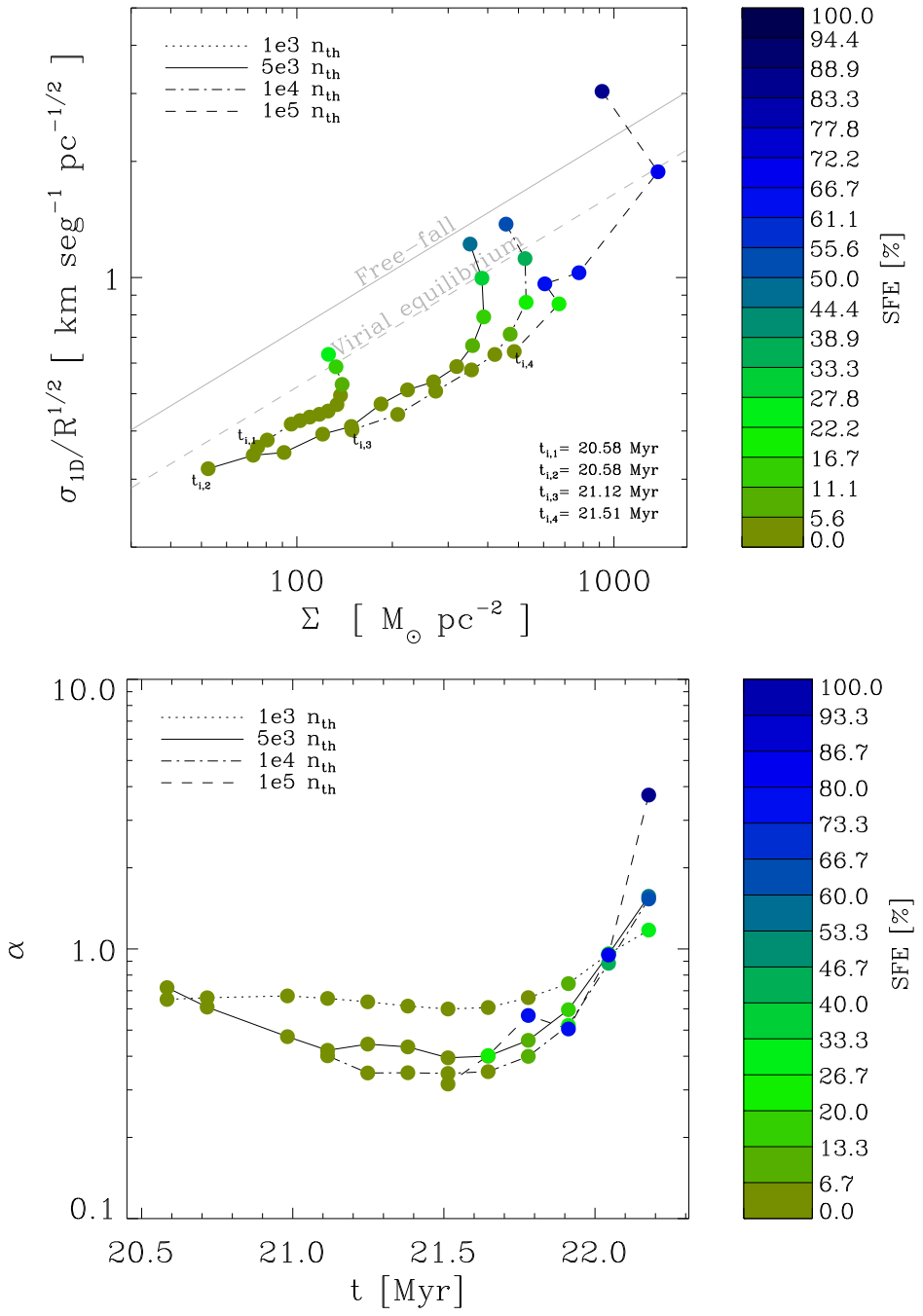

Figure 6.5: Evolution of the substructures in the numerical clump in the $\mathcal{L} - \Sigma$ diagram (top) and evolution of their virial parameter (bottom). Also shown is the evolution of the SFE, indicated by the colorbar. The final time is 22.18 Myr for structures defined at all density thresholds. The times when the structures appear for the first time at each threshold are indicated by $t_{i,n}$. The time interval between dots is ~ 0.13 Myr.

structures appear sub-virial for both low and high densities; *ii)* as the objects evolve in time (see also α *vs.* t plots), they approach equipartition and in one case the object even becomes super-virial. This can be seen for objects defined at all density

thresholds.

Additionally, a gradual increase is seen of both the star formation rate and the star formation efficiency, represented by the colors in figures 6.5 and 6.6. That is, an increase of the SFE and SFR occurs simultaneously with the increase of kinetic energy, manifested in the variation of the Larson ratio and the virial parameter. The increasing star formation activity is a natural consequence for a clump that becomes denser on average due to global gravitational contraction and thus contains a higher fraction of high-density gas (Zamora-Avilés & Vázquez-Semadeni, 2014; Vázquez-Semadeni et al., 2018) which is responsible for the 'instantaneous' star formation in the clump. Thus, *we suggest that SFR and SFE evolve simultaneously with the energy budget of the clumps.*

It is observed that, early in their evolution, the objects start with low values of α; in fact, the clump defined at $n_{\rm th} = 10^3\,{\rm cm}^{-3}$ remains with $\alpha \sim$ constant over ~ 1 Myr. For some other clumps, the virial parameter even decreases before star formation begins, to later increase again, approaching the free-fall value ($\alpha = 2$) at times when the SFR has reached values of a few $\times 100\,M_\odot$ Myr^{-1}. This shows that values of $1 \lesssim \alpha \lesssim 2$ are not necessarily a signature of unbound objects. Instead they may be indicative of the approach to the free-fall value.

This evolution might seem to be contradictory with the observed feature that most massive objects show lower virial parameters than the less massive ones. However, it is not. The upper panel in Fig. 6.7 shows a sample of clumps from the entire simulation taken from Camacho et al. (2016), at the same density thresholds here analyzed, showing that the clump ensemble exhibits the familiar trend of having larger values of α at lower masses (e.g., Kauffmann et al., 2013; Leroy et al., 2015). This trend is observed for the whole ensemble as well as for clumps defined at each density threshold.

In addition, the bottom panel of Fig. 6.7, shows the evolution of the clump substructure in the α-M diagram. As figures Figs. 6.5 and 6.6, the lines join clumps defined at the same density threshold at different times, indicated by the colorbar. Thus, the set of points shown with a particular color illustrates the hierarchy of nested structures at a given time, while points joined by each line represent the evolution of a clump defined at that threshold. It is noteworthy that the slope of the clump hierarchy at the last time exhibit a negative slope. This implies that the most massive objects in a coeval sample have lower values of α than the least massive ones, defined at high densities, in spite of the fact that each structure is seen to evolve from sub-virialization to equipartition, as predicted by eq. (6.5). This is because a clump defined by a volume density threshold evolves towards higher

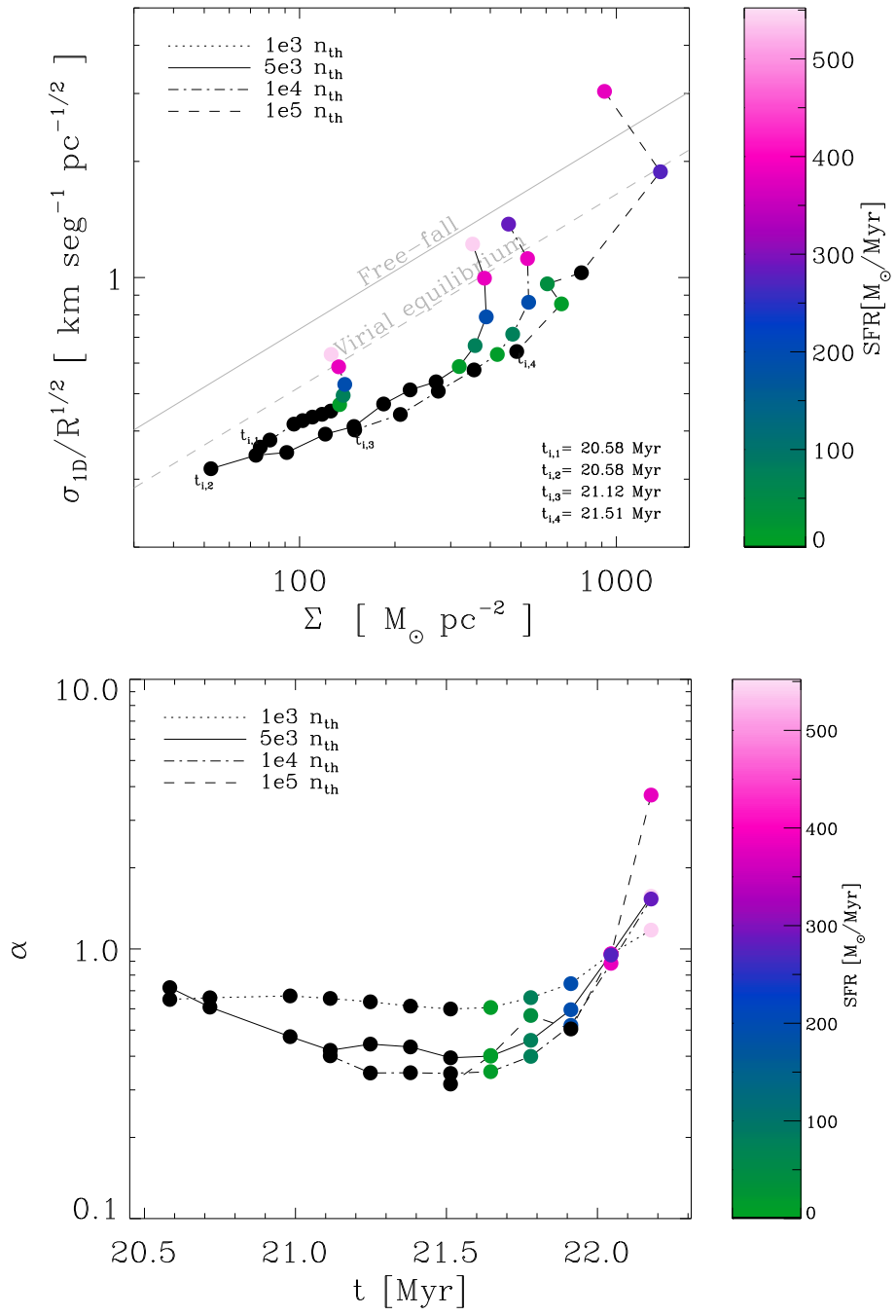

Figure 6.6: Same as figure 6.5 although in these plots the color scheme indicates the SFR.

column density and higher mass as it accretes material and becomes denser by gravitational contraction.

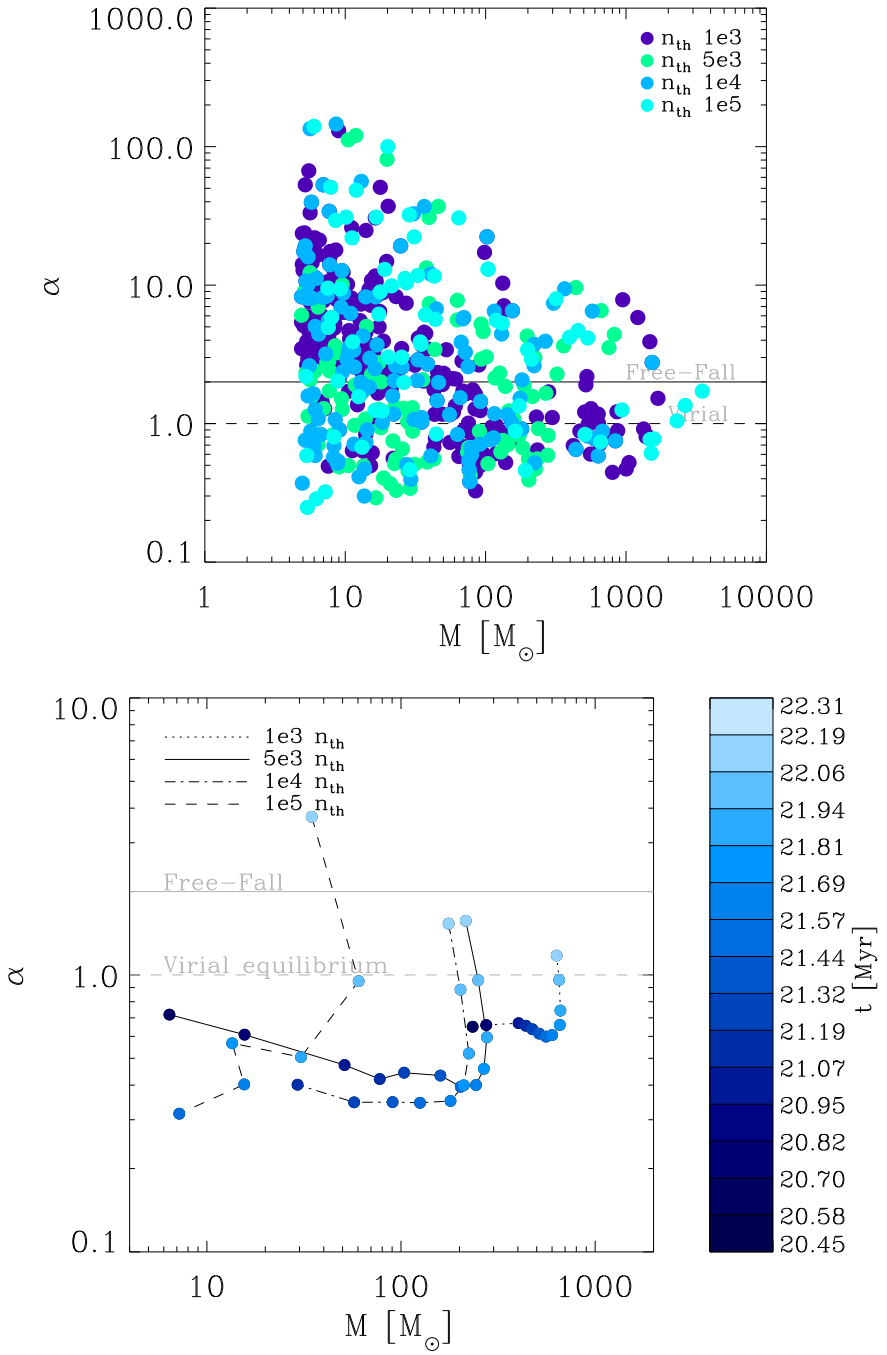

Figure 6.7: Top panel: virial parameter for a sample of clumps from the RUN03 simulation. We considered $t =$ 20.8, 21.2, 22.2, 24.8 and 26.5 Myr and the same density threshold for the numerical clump. Bottom panel: α temporal evolution. The time sequence is shown in colors, while the lines show the density thresholds.

6.4.2 Comparison with the observational sample

As mentioned in Sec 6.2, the two real clouds considered in this work are expected to be in different evolutionary stages. Indeed, the Pipe shows little signs of star forma-

tion (the component known as B59 or the Mouthpiece is known to have embedded a group of young stars, Brooke et al., 2007; Román-Zúñiga et al., 2010; Dzib et al., 2013) and a low fraction of its mass at high density, which has been interpreted as indication of an early evolutionary stage (e.g., Onishi et al., 1999; Rathborne et al., 2008; Lada et al., 2010; Frau et al., 2010, 2015; Vázquez-Semadeni et al., 2018). On the other hand, G14 exhibits active star formation and a duration of the star formation activity of a few Myr, suggestive of a somewhat more advanced evolutionary stage (Povich et al., 2016).

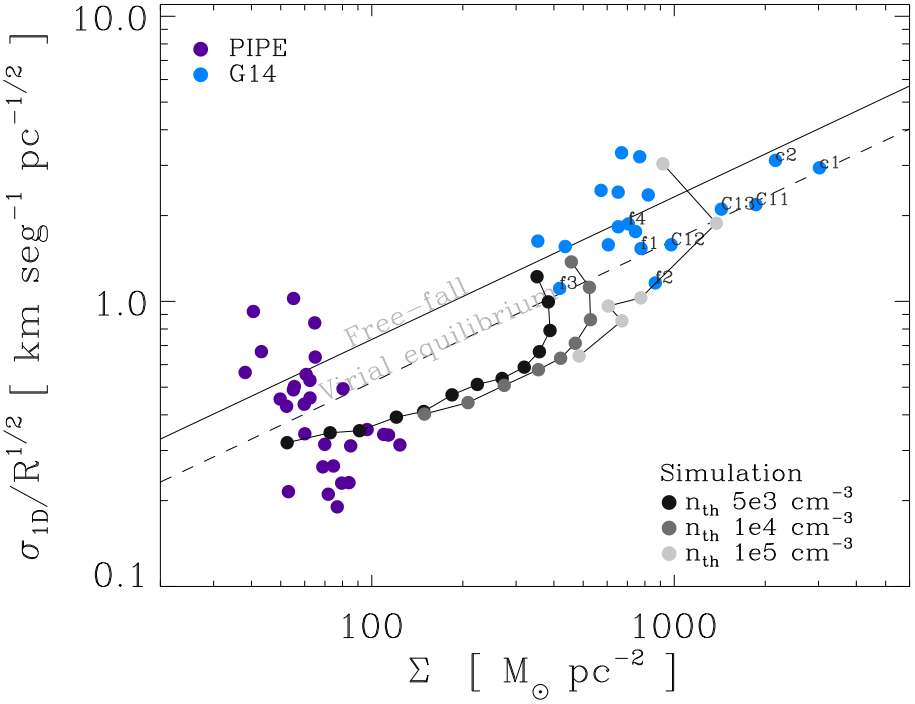

Figure 6.8: $\mathcal{L}-\Sigma$ diagram for the observational clump sample (purple and blue dots) and comparison with the temporal evolution for some of the clumps in the simulation. The simulated clumps evolve from the left to the right.

Similarly to what was done for the numerical sample, we plot the corresponding $\mathcal{L}-\Sigma$ diagram (Fig. 6.8) and α-mass plot (Fig. 6.9) for the substructures in the Pipe (purple dots) and G14 (blue dots) clouds. Additionally, we plot the evolution of the substructures of the numerical clump defined at $n_{\rm th} = 5 \times 10^3, 10^4$ and 10^5 cm^{-3} with the black, dark grey and light gray dots, respectively. The blue dots with alfanumeric labels in this figure are those with similar properties as the substructures in the numerical cloud (c.f. Sec. 6.3.3). In particular, the clump at 5×10^3 cm^{-3} (black dots) named the "Pipe-like core" (Sec. 6.3.3), evolves from a locus centered in that of the Pipe cores to one close to the filaments in the G14 sample. When the

Pipe-like core first appears (at 20.58 Myr), it shows a structure similar to the dense cores in the Pipe cloud with, $M \sim 6.4\ M_{\odot}$, $R \sim 0.2$ pc and $\sigma_{1D} \sim 0.14\ \mathrm{km\,s^{-1}}$, and exhibits a low virial parameter ~ 0.7. As the simulation evolves, the Pipe-like core grows in size, changing its morphology from roughly spherical to a more elongated structure (its largest axis has ~ 3 pc)[8]. Its mass grows in time even after the star formation begins. However, after ~ 0.3 Myr, its mass becomes roughly constant. At the latest time, the dense core has M $\sim 216\ M_{\odot}, R \sim\ 0.4,$ pc and $\sigma_{1\mathrm{D}} \sim 0.8\ \mathrm{km\,s^{-1}}$, comparable to the f2 and f3 filaments in G14 (see Tab.6.2).

On the other hand, the interior regions of the Pipe-like core within higher-n_{th} thresholds (gray dots in Fig. 6.8) evolve to positions comparable to those of denser G14 clumps and filaments. At time $t = 22.04$ Myr , the dark-gray dot on the virial equilibrium line has $M \sim 203\ M_{\odot}$, $R\ \sim 0.4$ pc, $\sigma_{1\mathrm{D}} \sim 0.6\ \mathrm{km\,s^{-1}}$, and a virial parameter ~ 0.9, between f1 and f3 of the G14 sample, while the light-gray dot on the same line has $M \sim 60\ M_{\odot}$, $R \sim 0.1\,\mathrm{pc}, \sigma_{1D} \sim 0.6\ \mathrm{km\,s^{-1}}$, and a virial parameter ~ 0.9, in the neighborhood of C11, C12, and C13.

We observe that roughy half of the cores in the Pipe sample (which we consider less evolved; see Sec. 6.2) appear in the sub-virial range in the $\mathcal{L} - \Sigma$ diagram. In contrast, the G14 sample (which we consider more evolved) occupies the equipartition and the strongly super-virial ($\alpha > 2$) region, which may be an effect produced by the stellar products in this region. This is consistent with the evolution of the numerical sample from sub-virial to super-virial states.

Concerning the star formation activity, Lada et al. (2010) report an SFR $\sim 5\ M_{\odot}$ $\mathrm{Myr^{-1}}$ for the Pipe, while Povich et al. (2016) report an SFR $\sim 7 \times 10^3\ M_{\odot}$ $\mathrm{Myr^{-1}}$ for G14, or roughly 3 orders of magnitude larger than that of the Pipe. Of course, a more meaningful comparison is in terms of the *specific* SFR, or *sfr*, since G14 is clearly a more massive region than the Pipe. Lada et al. (2010) report a total mass for the Pipe of $\sim 8 \times 10^3\ M_{\odot}$, while Povich et al. (2016) quote a mass $\sim 2 \times 10^5\ M_{\odot}$ for M17 S Wex, the parent cloud of the G14 IRDC. Thus, $sfr \sim 6.2 \times 10^{-4}$ $\mathrm{Myr^{-1}}$ for the Pipe, while $sfr \sim 3.5 \times 10^{-2}$ $\mathrm{Myr^{-1}}$ for G14. Then, the specific SFR of G14 is $\sim 50\times$ larger than that of the Pipe, implying indeed a much stronger star-forming activity even when normalized to the total cloud mass. Additionally, a recent study by Shimoikura et al. (2019) reported a SFE $9 - 17\%$ for the M17S Wex. This study, conducted on N_2H^+, concluded that, according to the density profile of the cores, more than 80% of their sample is consistent with the free-fall condition. This

[8]Recall that the size definition considered in this work assumes that all particles belonging to a clump are contained in a sphere whose volume is the sum of all the particles' volumes. Thus, the size, $R = (3V/4\pi)^{1/3}$, does not reflect the largest dimension of the clumps.

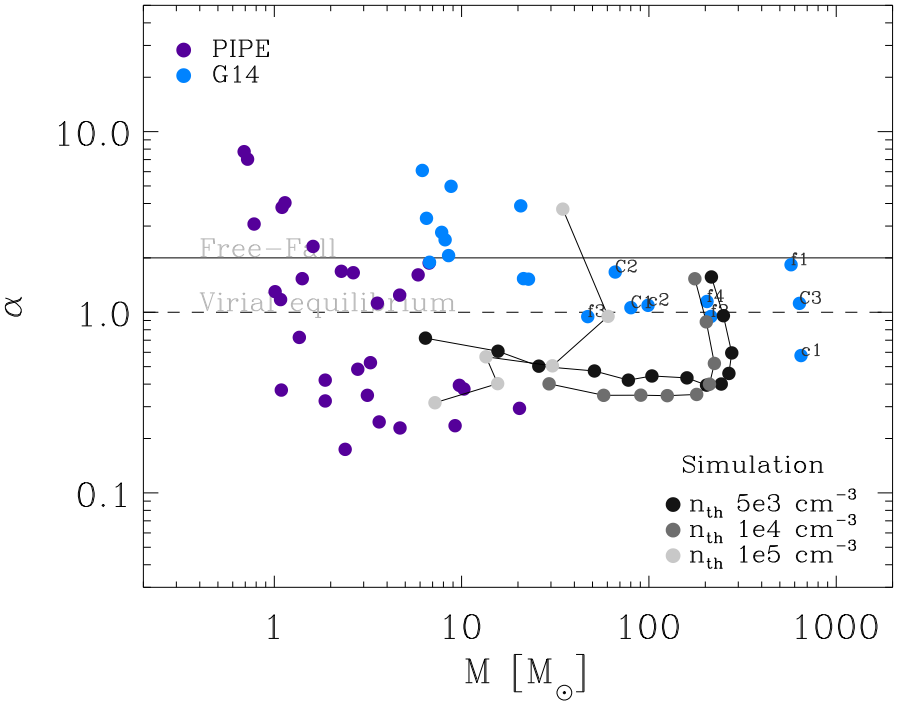

Figure 6.9: Virial parameter for the selected samples from the Pipe (purple), G14 (blue) and the simulation (black and gray). The clumps from the simulation start their evolution from the bottom-left points.

result reinforced our evolutionary scenario in terms of gravitational collapse. Thus, we suggest that a cloud like G14 might have evolved from a cloud with properties similar to those of the Pipe cloud.

6.5 Discussion

The evolution of the numerical clump sample studied in this work is consistent with the analytical calculations presented in BP+18, in the sense that the clumps evolve in the $\mathcal{L} - \Sigma$ diagram from the sub-virial region to the energy equipartition region, similarly to the evolution predicted by eq. (6.4). However, the clumps in the present study show a slightly different behavior. In our case, the clumps approach the equipartition lines almost perpendicularly to them, while the prediction is that they should approach these lines asymptotically (cf. eq. (6.4) and the left panel of Fig. 1 of BP+18). Moreover, the column density of our clumps does not increase monotonically over time, as in Fig. 1 of BP+18, but rather decreases again at late stages during the clumps' evolution. This difference is mainly due to the definition of the clumps employed in each case. In our numerical sample, clumps

are defined as connected implies that the clumps are free to vary in size and mass throughout their evolution. Additionally, the prescription of sink formation above a certain critical density precludes the formation of regions with density above the critical sink-formation value. Then, as the clumps evolve, they become denser until sink formation becomes significant. On the other hand, the analytical treatment in BP+18 simply follows spherical, constant-mass clumps as they collapse and increase their column density. Moreover, loss of gaseous mass to star formation is not considered in the analytical treatment of BP+18. Therefore, in this idealized setting, clumps can only decrease their volume and increase their column densities as they collapse. Instead, our numerical clumps can lose mass by forming sinks, and when they do, their density and column density decrease. Therefore, their evolutionary tracks in the $\mathcal{L} - \Sigma$ diagram differ from the analytical treatment, as also observed in the numerical core sample considered by BP+18, which describes paths in the $\mathcal{L} - \Sigma$ diagram similar to those of our own sample, characterized by a turnaround.

An important point to notice is that the ensemble of clumps in our simulation does contain a fraction of super-virial clumps at low column densities in the $\mathcal{L} - \Sigma$ diagram, or low masses in the α-M diagram, similarly to the case of observational surveys (e.g., Kauffmann et al., 2013; Leroy et al., 2015). This was interpreted in Camacho et al. (2016) and BP+18 as a consequence of those clumps being either in a dispersal state, or in an assembly stage by external (non-self-gravitating, or "inertial") compressions or by a large-scale potential well which drag them gravitationally. In neither case do the inertial motions (by "turbulence" or by a external gravitational field) provide support for the clumps to be in a near-equilibrium state, and so, for super-virial clumps, no need for an external confining thermal pressure exists. However, for clumps undergoing assembly (roughly half of the clump population; Camacho et al., 2016), the inflow may effectively be considered as a "confining" ram pressure for the densest material.

As discussed by Camacho et al. (2016) and BP+18, the starting location in the $\mathcal{L} - \Sigma$ diagram of clumps undergoing inertial assembly must appear as super-virial, since, by definition, the inertial assembly speed for these objects is larger than their self-gravitating speed, $\sigma_{\rm g}$, given by eq. (6.3). Later, as the clump becomes denser and more massive, and its self-gravitating speed increases, the latter eventually becomes larger than the assembly speed, and the clump may appear to be either in equipartition or sub-virial when it becomes dominated by self-gravity. In particular, it will appear sub-virial if $\sigma_{\rm g}$ is still smaller than the equipartition value $\sigma_{\rm eq} \equiv \sqrt{\eta GM/R}$, because R is still not sufficiently smaller than R_0 (upper solid lines in the left panel of Fig. 1 of BP+18).

The fact that the numerical clumps investigated in this work initiate their trajectories in the sub-virial region of the $\mathcal{L} - \Sigma$ and α-M diagrams indicates that they are already dominated by self-gravity, yet they have not had time to attain the equipartition speed, since equipartition is only attained at later times in their evolution, as shown by Figs. 6.8 and 6.9.

It is important to note also that, were we to follow the evolution of our numerical clumps to even more advanced stages, they would move into the super-virial region, since they would have lost a large amount of mass to sink formation, therefore losing gravitational energy from the gas mass, but the velocity dispersion would remain roughly the same. Therefore, they would appear to be super-virial. In Camacho et al. (2016) we showed that some apparently super-virial clumps could be made to appear in equipartition again when the mass in sinks was included in the computation of the kinetic to gravitational energy balance. Finally, this effect would also occur if feedback were included, because in this case mass would be lost from the clumps due to the feedback, also reducing their gravitational content. Thus, apparently super-virial clumps are likely to occur once a significant amount of their gas mass has been converted to stars and/or feedback has expelled a significant amount of mass from them. All of this, aside from geometrical effects such as those discussed by BP+18.

6.6 Summary

In this work we have presented a study of the energy budget of a star-forming clump in a numerical simulation and compared to the corresponding data from two real clouds. The clumps studied in this work, both from the simulation and from the observational data, lie close to the energy equipartition relation, shown in the $\mathcal{L} - \Sigma$ diagram. This trend has been approximately found in several previous observational and numerical studies (Keto & Myers, 1986; Heyer et al., 2009; Dobbs et al., 2011; Leroy et al., 2015; Traficante et al., 2015; Camacho et al., 2016; Ballesteros-Paredes et al., 2018). However, deviations from it are also systematically observed. In this study, we suggest that these deviations are characteristic of the clump evolutionary state, and that this evolution determines also the star formation activity of the clumps.

The main result from the present study is that our numerical clump evolves from a Pipe-like state to a G14 one in roughly 2 Myr. This implies that a massive and active star forming region like the IRDC G14 may have evolved from a cloud with properties similar to those of the Pipe cloud. The Pipe-like stage is characterized by a

lower mass, velocity dispersion, mean and peak densities, and star formation activity, while maintaining comparable dimensions. The increase in physical parameters is due to accretion of material external to the $n_{\rm th} = 10^3\,{\rm cm}^{-3}$ boundary we used to define this clump, as indicated by the fact that the time delay for the appearance of the first stars after the time at which we first observe the clump is within $\sim 10\%$ of the free-fall time for the cloud at the starting time.

This evolution of the clouds implies an evolution of the energy budget of their substructures, so that samples of cores of younger clouds appear displaced toward more sub-virial states in the $\mathcal{L}$–Σ and α-M diagrams, and, as the clouds age, their structures are displaced in these diagrams towards higher-column densities and closer to equipartition, due to the mechanism described in BP+18. Nevertheless, at late stages, coeval samples of clumps and cores exhibit the regularly-observed feature that more massive objects have lower values of α. This is because, as shown in Vázquez-Semadeni et al. (2019), for a coeval sample of cores selected in such a way that their mass scales as R^β, with $\beta < 3$, as is often the case, the more massive objects have lower densities, and therefore longer free-fall times. This implies that, at some age t, the more massive objects have traversed a smaller fraction of their free-fall time, and are therefore at earlier stages of their own evolution, therefore being more sub-virial.

Our results lead us to suggest that massive dense cores that appear sub-virial and quiescent (i.e., prestellar or very weakly-star-forming cores; e.g., Kauffmann et al., 2013; Liu et al., 2015; Ohashi et al., 2016; Sanhueza et al., 2017; Contreras et al., 2018) will evolve toward equipartition as they develop stronger star-formation activity. Also, since we found that, at early stages, the densest parts of the clumps appear more sub-virial than their envelopes, we predict that observations of the parent clumps of those sub-virial cores should reveal that the parent structures are closer to equipartition.

Chapter 7

Summary and conclusions

In the present thesis we have studied the intrinsic physical properties, the energy balance and the temporal evolution of the star formation activity of molecular clouds and their substructure in two SPH simulations of the formation and evolution of giant molecular clouds. Additionally, we have compared the results found from the simulations with data available in the literature for two real molecular clouds, likely to be at different evolutionary stages.

The simulations represent two different models of the formation of molecular clouds, one by converging motions in the warm neutral medium and the other by decaying generic turbulence in this medium. Neither one of the simulations includes magnetic fields or any kind of feedback; therefore, the motions and the kinetic energy are driven by gravity or by large-scale compressive motions. Once dense clouds form in both simulations, they begin to contract gravitationally and a few Myr later they begin to form stars. We select an ensemble of clumps in each simulation by defining clumps as connected sets of SPH particles above various density thresholds. Thus defined, the clouds and clumps vary in size and mass during their evolution. After star formation begins the clumps can lose mass by feeding mass to the stellar particles. At different times during the evolution, and at different densities, we derive mass, size, column density, velocity dispersion, the virial parameter, the star formation rate and the star formation efficiency for each dense structure.

On the other hand, published observational data from two molecular clouds likely to be at different evolutionary stages was compared to our numerical results to demonstrate the existence of a correlation between different levels of star formation activity and the energy budget of the clouds and clumps, attributable to evolutionary effects. The chosen clouds were the Pipe Nebula and the infrared dark cloud G14.225. We use data from the literature for the Pipe for all needed physical parameters, and, for G14.225, the physical parameters were derived from the existing observations.

For both clouds we consider the H_2 column density derived from extinction maps and the velocity dispersion derived from NH_3 line emission.

Using the numerical data, we searched for Larson velocity dispersion- and density-size relations and the generalized Larson scaling relation (GLSR), $\sigma_v/R^{1/2} \propto \Sigma^{1/2}$. We also investigated deviations around this relation to understand the physical processes that cause them. Finally, we studied the temporal evolution of the clumps star formation activity.The main results from this study are:

- Neither of the samples from the numerical simulations are consistent with the Larson scaling relations.
- Instead, the generalized Larson scaling relation is satisfied for both the numerical and the observational samples.
- Clump sub-samples in a narrow Σ range follow approximate Larson-like relations.
- Roughly half of the clumps with low Σ that exhibit a large scatter around the GLSR, particularly with an excess of kinetic energy, have negative mean velocity divergence, implying that they are undergoing compression.
- Some of the high-density clumps and cores exhibiting kinetic energy excesses, which we call super-virial, contain stellar particles. The excess, however, disappears when the mass of these particles is considered in the energy balance.
- Clumps with low kinetic energy are found additionally to the super-virial clumps. We refer to this condition as sub-virial.
- The star formation rate and star formation efficiency increase monotonically as a star-forming region evolves from the sub-virial to the equipartition regions.
- The virial parameter and the star formation activity of the substructures of the numerical cloud qualitatively agree with the two observed samples.
- The Pipe cores that tend to be sub-virial will evolve towards the super-virial region.
- G14 contains clumps that tend to be in the equipartition region, and even some cores that appear to be super-virial.
- As a consequence we conclude that a star forming region like G14 may have evolved from a region similar to the Pipe in a few megayears.

We interpret our results as a natural consequence of gravitational contraction at all scales, rather than virial equilibrium.

The absence of Larson scaling relations in our samples leads us to the conclusion that these relations are not universal, as has been thought since they were proposed. Furthermore, given that ensembles of clumps selected by column density ranges do exhibit Larson-like relations, we support the notion that these relations are consequence of observational effects, and are a special case of the generalized Larson scaling relation when considering constant column density. Additionally, we reinforced the notion of the energy equipartition condition, i.e., the relation $\sigma_v/R^{1/2} \propto \Sigma^{1/2}$, can be interpreted as both virial equilibrium or free-fall condition, given that observationally, it is not possible to discern between the two of them due to the small factor of $\sqrt{2}$ that separates these conditions. The clumps studied in this work, both from the simulation and from the observational data, lie close to this relation, even though they are not in equilibrium, but rather are contracting gravitationally.

The fact that the velocity field in some of the clouds and clumps with an excess of kinetic energy has negative mean divergence indicates convergent motions. Thus, we conclude that the excess of kinetic energy reflects the compressive motions not due to the self-gravity of the clumps, but rather to some external agent, either a larger-scale gravitational potential, or large-scale turbulent compressions in the medium that form the clumps. Then, the super-virial condition does not necessarily imply dispersion or a need for an external confining pressure, but can be indicative of assembly by ram pressure.

Within this context of globally contracting molecular clouds, we suggest an evolutionary process in which turbulent compressions generated by a large-scale potential well initially dominates the kinetic energy, exceeding the self-gravitational energy of the forming cloud. Then, as the cloud becomes denser and more massive, the self-gravitationally-driven velocity becomes dominant. On the other hand, the large-scale turbulence can in some cases cause disrupting motions, additionally to the natural disruption due to star formation (not included in this work). Based on the results and the suggested evolutionary model, we conclude that deviations from the energy equipartition relation are characteristic of the clump evolutionary state and, that this evolution determines also the star formation activity of the clumps.

The temporal evolution analysis of a star forming region and their substructure, shows that dense clumps evolve in the $\sigma_v/R^{1/2} - \Sigma$ diagram from the sub-virial region to the energy equipartition region, as well as in the α-M diagram. This is indicative that these clumps are already dominated by self-gravity, yet they have not had time to attain the equipartition speed, since equipartition is only attained

at later times in their evolution. It was observed that the virial parameter and the $\mathcal{L} \equiv \sigma_{\rm v}/R^{1/2}$ ratio evolve in their corresponding diagrams. Together with this evolution, both the SFR and the SFE of the clumps increase gradually. The increase of these parameters is consistent with the recently proposed scenario of hierarchical gravitational collapse.

The evolutionary scenario derived from the numerical simulations is qualitatively consistent with the energy balance and the star formation activity of the observational samples considered, the Pipe, which present a negligible star-formation activity and shows clumps that tend to be sub-virial, and G14, with significant star formation activity, showing clumps that tend to be in the equipartition region and even some cores that appear to be over-virial. With the results presented in this thesis we propose that massive dense cores that appear sub-virial and quiescent will evolve toward equipartition as they develop stronger star-formation activity. Thus, we conclude that the virial parameter and the star formation rate determine the evolutionary stage of a star forming region.

Bibliography

Abel, T. 2011, MNRAS, 413, 271

Alves, J., Lombardi, M., & Lada, C. J. 2007, A&A, 462, L17

Andre, P., Ward-Thompson, D., & Barsony, M. 2000, Protostars and Planets IV, 59

André, P., Men'shchikov, A., Bontemps, S., et al. 2010, A&A, 518, L102

André, P., Könyves, V., Arzoumanian, D., Palmeirim, P., & Peretto, N. 2013, New Trends in Radio Astronomy in the ALMA Era: The 30th Anniversary of Nobeyama Radio Observatory, 476, 95

André, P. 2017, Comptes Rendus Geoscience, 349, 187.

Arzoumanian, D., André, P., Didelon, P., et al. 2011, A&A, 529, L6.

Arzoumanian, D., André, P., Könyves, V., et al. 2019, A&A, 621, A42.

Ascenso, J., Lada, C. J., Alves, J., Román-Zúñiga, C. G., & Lombardi, M. 2013, A&A, 549, A135

Astropy Collaboration, Robitaille, T. P., Tollerud, E. J., et al. 2013, A&A, 558, A33

Audit, E., & Hennebelle, P. 2005, A&A, 433, 1

de Avillez, M. A., & Breitschwerdt, D. 2005, A&A, 436, 585

Bailey, N. D., Basu, S., & Caselli, P. 2017, A&A, 601, A18

Ballesteros-Paredes, J., Vázquez-Semadeni, E., & Scalo, J. 1999, ApJ, 515, 286

Ballesteros-Paredes, J., Hartmann, L., & Vázquez-Semadeni, E. 1999, ApJ, 527, 285

Ballesteros-Paredes, J., & Mac Low, M.-M. 2002, ApJ, 570, 734

Ballesteros-Paredes, J. 2006, MNRAS, 372, 443

Ballesteros-Paredes, J., Klessen, R. S., Mac Low, M.-M., & Vazquez-Semadeni, E. 2007,Protostars and Planets V, 63

Ballesteros-Paredes, J., Hartmann, L. W., Vázquez-Semadeni, E., Heitsch, F., & Zamora-Avilés, M. A. 2011, MNRAS, 411, 65

Ballesteros-Paredes, J., D'Alessio, P., & Hartmann, L. 2012, MNRAS, 427, 2562

Ballesteros-Paredes, J., Vázquez-Semadeni, E., Palau, A., & Klessen, R. S. 2018, MNRAS, 479, 2112

Banerjee, R., Vázquez-Semadeni, E., Hennebelle, P., & Klessen, R. S. 2009, MNRAS, 398, 1082

Basu, S., & Ciolek, G. E. 2004, ApJ, 607, L39

Bate, M. 1995, Ph.D. Thesis,

Bate, M. R., & Burkert, A. 1997, MNRAS, 288, 1060

Bate, M. R., Bonnell, I. A., & Bromm, V. 2003, MNRAS, 339, 577

Bate, M. R. 2012, MNRAS, 419, 3115

Barnes, P. J., Yonekura, Y., Fukui, Y., et al. 2011, ApJS, 196, 12

Barnes, P. J., Ryder, S. D., O'Dougherty, S. N., et al. 2013, MNRAS, 432, 2231

Barnes, P. J., Hernandez, A. K., O'Dougherty, S. N., et al. 2016, ApJ, 831, 67.

Barnes, P. J., Hernandez, A. K., Muller, E., et al. 2018, ApJ, 866, 19.

Barnes, A. T., Longmore, S. N., Avison, A., et al. 2019, MNRAS, 486, 283

Beaumont, C. N., Goodman, A. A., Alves, J. F., et al. 2012, MNRAS, 423, 2579

Bergin, E. A., Langer, W. D., & Goldsmith, P. F. 1995, ApJ, 441, 222

Bergin, E. A., & Tafalla, M. 2007, ARA&A, 45, 339

Bertoldi, F., & McKee, C. F. 1992, ApJ, 395, 140

Beuther, H., Ragan, S. E., Johnston, K., et al. 2015, A&A, 584, A67.

Beuther, H., Soler, J. D., Vlemmings, W., et al. 2018, A&A, 614, A64

Blitz, L., & Thaddeus, P. 1980, ApJ, 241, 676

Blitz, L. 1993, Protostars and Planets III, 125

Blitz, L., & Williams, J. P. 1999, NATO Advanced Science Institutes (ASI) Series C, 540, 3

Blitz, L., Fukui, Y., Kawamura, A., et al. 2007, Protostars and Planets V, 81

Bodenheimer, P. H. 2011, Principles of Star Formation: , Astronomy and Astrophysics Library. ISBN 978-3-642-15062-3. Springer-Verlag Berlin Heidelberg, 2011,

Bonnell, I. A., Bate, M. R., Clarke, C. J., & Pringle, J. E. 1997, MNRAS, 285, 201

Bonnell, I. 1997, The Third Pacific Rim Conference on Recent Development on Binary Star Research, 130, 1

Boulares, A., & Cox, D. P. 1990, ApJ, 365, 544

Brandenburg, A., Korpi, M. J., & Mee, A. J. 2007, ApJ, 654, 945

Brooke, T. Y., Huard, T. L., Bourke, T. L., et al. 2007, ApJ, 655, 364

Brunt, C. M., Heyer, M. H., Vázquez-Semadeni, E., & Pichardo, B. 2003, ApJ, 595, 824

Busquet, G., Palau, A., Estalella, R., et al. 2009, A&A, 506, 1183

Busquet, G., Zhang, Q., Palau, A., et al. 2013, ApJ, 764, L26

Busquet, G., Estalella, R., Palau, A., et al. 2016, ApJ, 819, 139

Burkert, A., & Hartmann, L. 2004, ApJ, 616, 288

Burkert, A., & Hartmann, L. 2013, ApJ, 773, 48

Caldwell, S., & Chang, P. 2018, MNRAS, 474, 4818

Camacho, V., Vázquez-Semadeni, E., Ballesteros-Paredes, J., et al. 2016, ApJ, 833, 113

Carroll-Nellenback, J. J., Frank, A., & Heitsch, F. 2014, ApJ, 790, 37

Caselli, P., & Myers, P. C. 1995, ApJ, 446, 665

Chen, H.-R. V., Zhang, Q., Wright, M. C. H., et al. 2019

Chomiuk, L., & Povich, M. S. 2011, AJ, 142, 197

Clark, P. C., & Bonnell, I. A. 2005, MNRAS, 361, 2

Clarke, S. D., Whitworth, A. P., & Hubber, D. A. 2016, MNRAS, 458, 319

Colín, P., Vázquez-Semadeni, E., & Gómez, G. C. 2013, MNRAS, 435, 1701

Colombo, D., Rosolowsky, E., Ginsburg, A., et al. 2015, MNRAS, 454, 2067

Commerçon, B., Hennebelle, P., & Henning, T. 2011, ApJ, 742, L9

Contreras, Y., Sanhueza, P., Jackson, J. M., et al. 2018, ApJ, 861, 14

Cox, D. P. 1983, ApJ, 265, L61

Cox, D. P. 1985, ApJ, 288, 465

Cox, D. P. 2005, ARA&A, 43, 337

Crutcher, R. M. 1999, ApJ, 520, 706

Crutcher, R. M. 2012, ARA&A, 50, 29

Dalgarno, A., & McCray, R. A. 1972, ARA&A, 10, 375

Dale, J. E., Ercolano, B., & Bonnell, I. A. 2012, MNRAS, 424, 377

Dale, J. E., Ngoumou, J., Ercolano, B., & Bonnell, I. A. 2014, MNRAS, 442, 694

Dame, T. M., Elmegreen, B. G., Cohen, R. S., & Thaddeus, P. 1986, ApJ, 305, 892

Dame, T. M., Hartmann, D., & Thaddeus, P. 2001, ApJ, 547, 792

Davis, L., Jr., & Greenstein, J. L. 1951, ApJ, 114, 206

Dickey, J. M., Salpeter, E. E., & Terzian, Y. 1977, ApJ, 211, L77

Dickman, R. L. 1978, ApJS, 37, 407

Dickman, R. L., Kutner, M. L., Pasachoff, J. M., et al. 1980, ApJ, 238, 853

Dobbs, C. L., Burkert, A., & Pringle, J. E. 2011, MNRAS, 413, 2935

Dobbs, C. L., Krumholz, M. R., Ballesteros-Paredes, J., et al. 2014, Protostars and Planets VI, 3

Draine, B. T. 2011, Physics of the Interstellar and Intergalactic Medium by Bruce T. Draine. Princeton University Press, 2011. ISBN: 978-0-691-12214-4,

Dzib, S. A., Rodríguez, L. F., Araudo, A. T., et al. 2013, Rev. Mexicana Astron. Astrofis., 49, 345

Elmegreen, B. G. 1983, MNRAS, 203, 1011

Elmegreen, B. G., & Scalo, J. 2004, ARA&A, 42, 211

Estalella, R. & Anglada, G., Introducción a la Física del Medio Interestelar, 1996

Evans, N. J., II 1999, ARA&A, 37, 311

Falgarone, E., Puget, J.-L., & Perault, M. 1992, A&A, 257, 715

Fall, S. M., Krumholz, M. R., & Matzner, C. D. 2010, ApJ, 710, L142

Federrath, C., Klessen, R. S., & Schmidt, W. 2008, ApJ, 688, L79

Federrath, C., Banerjee, R., Clark, P. C., & Klessen, R. S. 2010, ApJ, 713, 269

Federrath, C., & Klessen, R. S. 2012, ApJ, 761, 156

Federrath, C., & Klessen, R. S. 2013, ApJ, 763, 51

Federrath, C. 2015, MNRAS, 450, 4035

Ferrière, K. M. 2001, Reviews of Modern Physics, 73, 1031

Field, G. B. 1965, ApJ, 142, 531

Field, G. B., Goldsmith, D. W., & Habing, H. J. 1969, ApJ, 155, L149

Field, G. B., Blackman, E. G., & Keto, E. R. 2008, MNRAS, 385, 181

Field, G. B., Blackman, E. G., & Keto, E. R. 2011, MNRAS, 416, 710

Fogerty, E., Frank, A., Heitsch, F., et al. 2016, MNRAS, 460, 2110.

Franco, J., Shore, S. N., & Tenorio-Tagle, G. 1994, ApJ, 436, 795

Frau, P., Girart, J. M., Beltrán, M. T., et al. 2010, ApJ, 723, 1665

Frau, P., Girart, J. M., Beltrán, M. T., et al. 2012, ApJ, 759, 3

Frau, P., Girart, J. M., Alves, F. O., et al. 2015, A&A, 574, L6

Frerking, M. A., Langer, W. D., & Wilson, R. W. 1982, ApJ, 262, 590

Galván-Madrid, R., Vázquez-Semadeni, E., Kim, J., & Ballesteros-Paredes, J. 2007, ApJ, 670, 480

Galván-Madrid, R., Keto, E., Zhang, Q., et al. 2009, ApJ, 706, 1036

Galván-Madrid, R., Liu, H. B., Zhang, Z.-Y., et al. 2013, ApJ, 779, 121

Gatto, A., Walch, S., Low, M.-M. M., et al. 2015, MNRAS, 449, 1057

Gatto, A., Walch, S., Naab, T., et al. 2017, MNRAS, 466, 1903

Gazol, A., Vázquez-Semadeni, E., Sánchez-Salcedo, F. J., & Scalo, J. 2001, ApJ, 557, L121

Gazol, A., Vázquez-Semadeni, E., & Kim, J. 2005, ApJ, 630, 911

Gazol, A., & Kim, J. 2013, ApJ, 765, 49

Gibson, D., Plume, R., Bergin, E., Ragan, S., & Evans, N. 2009, ApJ, 705, 123

Ginsburg, A., Goss, W. M., Goddi, C., et al. 2016, A&A, 595, A27

Girichidis, P., Konstandin, L., Whitworth, A. P., et al. 2014, ApJ, 781, 91

Goldreich, P., & Kwan, J. 1974, ApJ, 189, 441

Goldsmith, P. F. 1987, Interstellar Processes, 134, 51

Goldsmith, P. F., Heyer, M., Narayanan, G., et al. 2008, ApJ, 680, 428

Gómez, G. C., & Vázquez-Semadeni, E. 2014, ApJ, 791, 124

Gong, M., & Ostriker, E. C. 2015, ApJ, 806, 31

González-Samaniego, A., Vázquez-Semadeni, E., González, R. F., & Kim, J. 2014, MNRAS, 440, 2357

Grisdale, K., Agertz, O., Renaud, F., et al. 2019

Habart, E., Walmsley, M., Verstraete, L., et al. 2005, Space Sci. Rev., 119, 71

Hacar, A., Alves, J., Tafalla, M., & Goicoechea, J. R. 2017, A&A, 602, L2

Haid, S., Walch, S., Seifried, D., et al. 2019, MNRAS, 482, 4062

Hartmann, L., Ballesteros-Paredes, J., & Bergin, E. A. 2001, ApJ, 562, 852

Hartmann, L., & Burkert, A. 2007, ApJ, 654, 988

Heiles, C. 2001, Tetons 4: Galactic Structure, Stars and the Interstellar Medium, 231, 294

Heiles, C., & Troland, T. H. 2003, ApJ, 586, 1067

Heiner, J. S., Vázquez-Semadeni, E., & Ballesteros-Paredes, J. 2015, MNRAS, 452, 1353

Heitsch, F., Mac Low, M.-M., & Klessen, R. 2000, Star Formation from the Small to the Large Scale, 445, 391

Heitsch, F., Mac Low, M.-M., & Klessen, R. S. 2001, ApJ, 547, 280

Heitsch, F., Zweibel, E. G., Slyz, A. D., & Devriendt, J. E. G. 2004, ApJ, 603, 165

Heitsch, F., Burkert, A., Hartmann, L. W., Slyz, A. D., & Devriendt, J. E. G. 2005, ApJ, 633, L113

Heitsch, F., Slyz, A. D., Devriendt, J. E. G., Hartmann, L. W., & Burkert, A. 2006, ApJ, 648, 1052

Heitsch, F., Hartmann, L. W., Slyz, A. D., Devriendt, J. E. G., & Burkert, A. 2008, ApJ, 674, 316

Heitsch, F. 2013, ApJ, 769, 115

Hennebelle, P., & Pérault, M. 1999, A&A, 351, 309

Hennebelle, P., & Pérault, M. 2000, A&A, 359, 1124

Hennebelle, P., & Inutsuka, S.-i. 2006, ApJ, 647, 404

Hennebelle, P., Banerjee, R., Vázquez-Semadeni, E., Klessen, R. S., & Audit, E. 2008, A&A, 486, L43

Hennebelle, P. 2013, A&A, 556, A153

Hennebelle, P., & André, P. 2013, A&A, 560, A68

Hennebelle, P., & Inutsuka, S.-i. 2019, arXiv:1902.00798

Heyer, M. H., Carpenter, J. M., & Snell, R. L. 2001, ApJ, 551, 852

Heyer, M. H., & Brunt, C. M. 2004, ApJ, 615, L45

Heyer, M., Krawczyk, C., Duval, J., & Jackson, J. M. 2009, ApJ, 699, 1092

Heyer, M., & Dame, T. M. 2015, ARA&A, 53, 583

Hiltner, W. A. 1949, Science, 109, 165

Hopkins, P. F., Quataert, E., & Murray, N. 2012, MNRAS, 421, 3522

Houlahan, P., & Scalo, J. 1992, ApJ, 393, 172

Hoyle, F. 1953, ApJ, 118, 513

Hunter, J. H., & Fleck, R. C. 1982, ApJ, 256, 505

10.11588/heidok.00021519

Inutsuka, S., & Koyama, H. 2004, Revista Mexicana de Astronomia y Astrofisica Conference Series, 22, 26

Jackson, J. M., Rathborne, J. M., Shah, R. Y., et al. 2006, ApJS, 163, 145

Jackson, J. M., Whitaker, J. S., Rathborne, J. M., et al. 2019, ApJ, 870, 5

Jaffe, D. T., Guesten, R., & Downes, D. 1981, ApJ, 250, 621

Jaffe, D. T., Stier, M. T., & Fazio, G. G. 1982, ApJ, 252, 601

Jappsen, A.-K., Klessen, R. S., Larson, R. B., Li, Y., & Mac Low, M.-M. 2005, A&A, 435, 611

Jeans, J. H. 1902, Philosophical Transactions of the Royal Society of London Series A, 199, 1

Jenkins, E. B. 2004, Ap&SS, 289, 215

Jenkins, E. B., & Tripp, T. M. 2011, ApJ, 734, 65

Joung, M. K. R., & Mac Low, M.-M. 2006, ApJ, 653, 1266

Kauffmann, J., Pillai, T., & Goldsmith, P. F. 2013, ApJ, 779, 185

Kegel, W. H. 1989, A&A, 225, 517

Kennicutt, R. C., Jr. 1998, ApJ, 498, 541

Keto, E. R., & Myers, P. C. 1986, ApJ, 304, 466

Kim, W.-T., Ostriker, E. C., & Stone, J. M. 2002, ApJ, 581, 1080.

Kirk, H., Myers, P. C., Bourke, T. L., et al. 2013, ApJ, 766, 115

Klessen, R. S., Burkert, A., & Bate, M. R. 1998, ApJ, 501, L205

Klessen, R. S., Heitsch, F., & Mac Low, M.-M. 2000, ApJ, 535, 887

Klessen, R. S., & Hennebelle, P. 2010, A&A, 520, A17

Klessen, R. S., & Glover, S. C. O. 2016, Star Formation in Galaxy Evolution: Connecting Numerical Models to Reality, Saas-Fee Advanced Course, Volume 43. ISBN 978-3-662-47889-9. Springer-Verlag Berlin Heidelberg, 2016, p. 85, 43, 85

Klein, R. I., & Woods, D. T. 1998, ApJ, 497, 777

Körtgen, B., Seifried, D., Banerjee, R., Vázquez-Semadeni, E., & Zamora-Avilés, M. 2016, MNRAS, 459, 3460

Koyama, H., & Inutsuka, S.-I. 2000, ApJ, 532, 980

Koyama, H., & Inutsuka, S.-i. 2002, ApJ, 564, L97

Kramer, C., Stutzki, J., Rohrig, R., & Corneliussen, U. 1998, A&A, 329, 249

Kritsuk, A. G., Norman, M. L., Padoan, P., & Wagner, R. 2007, ApJ, 665, 416

Kritsuk, A. G., Ustyugov, S. D., & Norman, M. L. 2017, New Journal of Physics, 19, 065003

Kruijssen, J. M. D., Schruba, A., Chevance, M., et al. 2019, Nature, 569, 519

Krumholz, M. R., & McKee, C. F. 2005, ApJ, 630, 250

Krumholz, M. R., Matzner, C. D., & McKee, C. F. 2006, ApJ, 653, 361

Krumholz, M. R., Klein, R. I., & McKee, C. F. 2012, ApJ, 754, 71

Kruegel, E. 2003, The physics of interstellar dust.

Lada, C. J. 1985, ARA&A, 23, 267

Lada, C. J., & Kylafis, N. D. 1991, NATO Advanced Science Institutes (ASI) Series C, 342,

Lada, C. J., & Lada, E. A. 2003, ARA&A, 41, 57

Lada, C. J., Muench, A. A., Rathborne, J., Alves, J. F., & Lombardi, M. 2008, ApJ, 672, 410

Lada, C. J., Lombardi, M., & Alves, J. F. 2009, ApJ, 703, 52

Lada, C. J., & Kylafis, N. D. 1991, NATO Advanced Science Institutes (ASI) Series C, 342,

Lada, C. J., Lombardi, M., & Alves, J. F. 2010, ApJ, 724, 687

Larson, R. B. 1969, MNRAS, 145, 271

Larson, R. B. 1977, Evolution of Galaxies and Stellar Populations, 97

Larson, R. B. 1977, Star Formation, 75, 249

Larson, R. B. 1979, MNRAS, 186, 479

Larson, R. B. 1981, MNRAS, 194, 809

Lee, E. J., Miville-Deschênes, M.-A., & Murray, N. W. 2016, ApJ, 833, 229

Leroy, A. K., Bolatto, A. D., Ostriker, E. C., et al. 2015, ApJ, 801, 25

Li, Z.-Y., & Nakamura, F. 2004, ApJ, 609, L83

Li, Z.-Y., & Nakamura, F. 2006, ApJ, 640, L187

Li, P. S., & Klein, R. I. 2019, MNRAS, 485, 4509

Lin, Y., Liu, H. B., Dale, J. E., et al. 2017, ApJ, 840, 22

Liszt, H. S., Wilson, R. W., Penzias, A. A., et al. 1974, ApJ, 190, 557

Liu, H. B., Galván-Madrid, R., Jiménez-Serra, I., et al. 2015, ApJ, 804, 37.

Lombardi, M., Alves, J., & Lada, C. J. 2006, A&A, 454, 781

Lombardi, M., Alves, J., & Lada, C. J. 2010, A&A, 519, L7

Lombardi, M., Alves, J., & Lada, C. J. 2015, A&A, 576, L1

Loren, R. B. 1989, ApJ, 338, 925

Louvet, F., Motte, F., Hennebelle, P., et al. 2014, A&A, 570, A15

Louvet, F., Neupane, S., Garay, G., et al. 2018, arXiv:1810.12928

Mac Low, M.-M., & Klessen, R. S. 2004, Reviews of Modern Physics, 76, 125.

Mac Low, M.-M. 2003, Turbulence and Magnetic Fields in Astrophysics, 614, 182

Maddalena, R. J., & Thaddeus, P. 1985, ApJ, 294, 231

Matzner, C. D., & McKee, C. F. 2000, ApJ, 545, 364

Matzner, C. D. 2002, ApJ, 566, 302

McMullin, J. P., Waters, B., Schiebel, D., Young, W., & Golap, K. 2007, Astronomical Data Analysis Software and Systems XVI, 376, 127

Monaghan, J. J. 1992, ARA&A, 30, 543

Mouschovias, T. C. 1991, NATO Advanced Science Institutes (ASI) Series C, Vol. 342, edited by Charles J. Lada and Nikolaos D. Kylafis., p.449

Muench, A. A., Lada, C. J., Rathborne, J. M., Alves, J. F., & Lombardi, M. 2007, ApJ, 671, 1820

Myers, P. C., Dame, T. M., Thaddeus, P., et al. 1986, ApJ, 301, 398

Myers, P. C., & Goodman, A. A. 1988, ApJ, 329, 392

Myers, P. C. 1991, Fragmentation of Molecular Clouds and Star Formation, 147, 221

Myers, A. T., Klein, R. I., Krumholz, M. R., & McKee, C. F. 2014, MNRAS, 439, 3420

Naranjo-Romero, R., Vázquez-Semadeni, E., & Loughnane, R. M. 2015, ApJ, 814, 48

Nakamura, F., & Li, Z.-Y. 2008, ApJ, 687, 354

McKee, C. F., & Ostriker, J. P. 1977, ApJ, 218, 148

McKee, C. F., & Ostriker, E. C. 2007, ARA&A, 45, 565

Mac Low, M.-M., Klessen, R. S., Burkert, A., & Smith, M. D. 1998, Physical Review Letters, 80, 2754

Molinari, S., Swinyard, B., Bally, J., et al. 2010, A&A, 518, L100

Murray, N. 2011, ApJ, 729, 133

Myers, P. C. 1987, Interstellar Processes, 134, 71

Myers, A. T., McKee, C. F., Cunningham, A. J., Klein, R. I., & Krumholz, M. R. 2013, ApJ, 766, 97

Nakamura, F., & Li, Z.-Y. 2005, ApJ, 631, 411

Nakamura, F., & Li, Z.-Y. 2007, ApJ, 662, 395

Ohashi, S., Sanhueza, P., Chen, H.-R. V., et al. 2016, ApJ, 833, 209

Onishi, T., Kawamura, A., Abe, R., et al. 1999, PASJ, 51, 871

Ossenkopf, V., Klessen, R. S., & Heitsch, F. 2001, A&A, 379, 1005

Ostriker, E. C., Gammie, C. F., & Stone, J. M. 1999, ApJ, 513, 259

Ostriker, E. C., Stone, J. M., & Gammie, C. F. 2001, ApJ, 546, 980

Ostriker, E. C., McKee, C. F., & Leroy, A. K. 2010, ApJ, 721, 975

Padoan, P. 1995, MNRAS, 277, 377

Padoan, P., & Nordlund, Å. 1999, ApJ, 526, 279

Padoan, P., Juvela, M., Goodman, A. A., & Nordlund, Å. 2001, ApJ, 553, 227

Padoan, P., & Nordlund, Å. 2002, ApJ, 576, 870

Padoan, P., Nordlund, Å., Kritsuk, A. G., Norman, M. L., & Li, P. S. 2007, ApJ, 661, 972

Padoan, P., & Nordlund, Å. 2011, ApJ, 730, 40

Padoan, P., Haugbølle, T., & Nordlund, Å. 2012, ApJ, 759, L27

Padoan, P., Pan, L., Haugbølle, T., & Nordlund, Å. 2016, ApJ, 822, 11

Palau, A., Fuente, A., Girart, J. M., et al. 2013, ApJ, 762, 120

Palau, A., Ballesteros-Paredes, J., Vázquez-Semadeni, E., et al. 2015, MNRAS, 453, 3785

Pan, L., Padoan, P., Haugbolle, T., & Nordlund, A. 2015, arXiv:1510.04742

Passot, T., & Pouquet, A. 1987, Journal of Fluid Mechanics, 181, 441

Passot, T., Vazquez-Semadeni, E., & Pouquet, A. 1995, ApJ, 455, 536

Peretto, N., Hennebelle, P., & André, P. 2007, A&A, 464, 983

Peretto, N., & Fuller, G. A. 2009, A&A, 505, 405

Peretto, N., André, P., Könyves, V., et al. 2012, A&A, 541, A63

Peretto, N., Fuller, G. A., Duarte-Cabral, A., et al. 2013, A&A, 555, A112

Peretto, N., Fuller, G. A., André, P., et al. 2014, A&A, 561, A83

Peters, T., Banerjee, R., Klessen, R. S., et al. 2010, ApJ, 711, 1017.

Pineda, J. L., Goldsmith, P. F., Chapman, N., et al. 2010, ApJ, 721, 686.

Piontek, R. A., & Ostriker, E. C. 2005, ApJ, 629, 849

Piontek, R. A., & Ostriker, E. C. 2004, ApJ, 601, 905

Pitts, R. L., Barnes, P. J., & Varosi, F. 2019, MNRAS, 484, 305.

Plume, R., Jaffe, D. T., Evans, N. J., II, Martín-Pintado, J., & Gómez-González, J. 1997, ApJ, 476, 730

Pon, A., Toalá, J. A., Johnstone, D., et al. 2012, ApJ, 756, 145

Povich, M. S., & Whitney, B. A. 2010, ApJ, 714, L285

Povich, M. S., Townsley, L. K., Robitaille, T. P., et al. 2016, ApJ, 825, 125

Rathborne, J. M., Jackson, J. M., & Simon, R. 2006, ApJ, 641, 389

Rathborne, J. M., Lada, C. J., Muench, A. A., Alves, J. F., & Lombardi, M. 2008, ApJS, 174, 396

Roberts, W. W. 1969, ApJ, 158, 123

Rogers, H., & Pittard, J. M. 2013, MNRAS, 431, 1337

Rohlfs, K., & Wilson, T. L. 1996, Tools of Radio Astronomy.

Román-Zúñiga, C. G., Alves, J. F., Lada, C. J., & Lombardi, M. 2010, ApJ, 725, 2232

Rosolowsky, E., & Leroy, A. 2006, PASP, 118, 590

Rosolowsky, E. W., Pineda, J. E., Kauffmann, J., & Goodman, A. A. 2008, ApJ, 679, 1338-1351

Saajasto, M., Juvela, M., Dobashi, K., et al. 2017, A&A, 608, A21.

Sánchez-Monge, Á., Palau, A., Fontani, F., et al. 2013, MNRAS, 432, 3288

Sanhueza, P., Jackson, J. M., Zhang, Q., et al. 2017, ApJ, 841, 97

Seifried, D., & Walch, S. 2015, MNRAS, 452, 2410

Scalo, J. 1990, Physical Processes in Fragmentation and Star Formation, 162, 151

Scannapieco, E., Gray, W. J., & Pan, L. 2012, ApJ, 746, 57

Shimoikura, T., Dobashi, K., Hirose, A., et al. 2019, PASJ, 82

Schmidt, M. 1959, ApJ, 129, 243

Schneider, S., & Elmegreen, B. G. 1979, ApJS, 41, 87

Schneider, N., Csengeri, T., Bontemps, S., et al. 2010, A&A, 520, A49

Schneider, N., Csengeri, T., Klessen, R. S., et al. 2015, A&A, 578, A29.

Shirley, Y. L., Evans, N. J., II, Young, K. E., Knez, C., & Jaffe, D. T. 2003, ApJS, 149, 375

Shu, F. H. 1977, ApJ, 214, 488

Shu, F. H., Adams, F. C., & Lizano, S. 1987, ARA&A, 25, 23

Shu, F. H., Lizano, S., & Adams, F. C. 1987, Star Forming Regions, 115, 417

Shu, F. H. 1992, Journal of the British Astronomical Association, 102, 230.

Shu, F. H., Li, Z.-Y., & Allen, A. 2004, ApJ, 601, 930

Solomon, P. M., Rivolo, A. R., Barrett, J., & Yahil, A. 1987, ApJ, 319, 730

Spitzer, L. 1978, Physical processes in the interstellar medium, by Lyman Spitzer. New York Wiley-Interscience, 1978. 333 p.,

Springel, V., Yoshida, N., & White, S. D. M. 2001, New A, 6, 79

Springel, V. 2005, MNRAS, 364, 1105

Stone, J. M., Ostriker, E. C., & Gammie, C. F. 1998, ApJ, 508, L99

Stutzki, J., & Guesten, R. 1990, ApJ, 356, 513

Takakubo, K. 1967, Bulletin of the Astronomical Institutes of the Netherlands, 19, 125

Thaddeus, P. 1977, Star Formation, 75, 37

Tielens, A. G. G. M. 2005, The Physics and Chemistry of the Interstellar Medium

Toalá, J. A., Vázquez-Semadeni, E., & Gómez, G. C. 2012, ApJ, 744, 190

Traficante, A., Fuller, G. A., Smith, R., et al. 2015, EAS Publications Series, 75, 185

Traficante, A., Fuller, G. A., Smith, R. J., et al. 2018, MNRAS, 473, 4975

Vázquez-Semadeni, E., Passot, T., & Pouquet, A. 1995, ApJ, 441, 702

Vázquez-Semadeni, E., Ballesteros-Paredes, J., & Rodríguez, L. F. 1997, ApJ, 474, 292

Vázquez-Semadeni, E., Ostriker, E. C., Passot, T., Gammie, C. F., & Stone, J. M. 2000, Protostars and Planets IV, 3

Vázquez-Semadeni, E., Gazol, A., & Scalo, J. 2000, ApJ, 540, 271

Vázquez-Semadeni, E., Gazol, A., Passot, T., & et al. 2003, Turbulence and Magnetic Fields in Astrophysics, 614, 213

Vázquez-Semadeni, E., Kim, J., Shadmehri, M., & Ballesteros-Paredes, J. 2005, ApJ, 618, 344

Vázquez-Semadeni, E., Kim, J., & Ballesteros-Paredes, J. 2005, ApJ, 630, L49

Vázquez-Semadeni E., Gómez G. C., Jappsen A.-K., Ballesteros-Paredes J., González R. F., Klessen R. S., 2007, ApJ, 657, 870

Vázquez-Semadeni, E., Ryu, D., Passot, T., González, R. F., & Gazol, A. 2006, ApJ, 643, 245

Vázquez-Semadeni, E., González, R. F., Ballesteros-Paredes, J., Gazol, A., & Kim, J. 2008, MNRAS, 390, 769

Vázquez-Semadeni E., Gómez G. C., Jappsen A.-K., Ballesteros-Paredes J., Klessen R. S., 2009, ApJ, 707, 1023

Vázquez-Semadeni, E. 2010, The Dynamic Interstellar Medium: A Celebration of the Canadian Galactic Plane Survey, 438, 83

Vázquez-Semadeni, E., Colín, P., Gómez, G. C., Ballesteros-Paredes, J., & Watson, A. W. 2010, ApJ, 715, 1302

Vázquez-Semadeni, E., Banerjee, R., Gómez, G. C., et al. 2011, MNRAS, 414, 2511

Vázquez-Semadeni, E. 2015, Magnetic Fields in Diffuse Media, 401.

Vázquez-Semadeni, E., González-Samaniego, A., & Colín, P. 2017, MNRAS, 467, 1313

Vázquez-Semadeni, E., Zamora-Avilés, M., Galván-Madrid, R., & Forbrich, J. 2018, MNRAS, 479, 3254

Vázquez-Semadeni, E., Palau, A., Ballesteros-Paredes, J., et al. 2019, arXiv e-prints , arXiv:1903.11247.

Vishniac, E. T. 1994, ApJ, 428, 186

Walch, S., & Naab, T. 2015, MNRAS, 451, 2757

Wang, P., Li, Z.-Y., Abel, T., & Nakamura, F. 2010, ApJ, 709, 27

Whitworth, A. 1979, MNRAS, 186, 59

Williams, J. P., de Geus, E. J., & Blitz, L. 1994, ApJ, 428, 693

Williams, J. P., Blitz, L., & McKee, C. F. 2000, Protostars and Planets IV, 97

Wilson, . W., Jefferts, K. B., & Penzias, A. A. 1970, ApJ, 161, L43

Wilson, C. D., & Scoville, N. 1990, ApJ, 363, 435

Wolfire, M. G., Hollenbach, D., McKee, C. F., Tielens, A. G. G. M., & Bakes, E. L. O. 1995, ApJ, 443, 152

Wolfire, M. G., McKee, C. F., Hollenbach, D., et al. 2003, ApJ, 587, 278.

Wu, J., Evans, N. J., II, Shirley, Y. L., & Knez, C. 2010, ApJS, 188, 313

Xu, Y., Moscadelli, L., Reid, M. J., et al. 2011, ApJ, 733, 25

Zamora-Avilés, M., Vázquez-Semadeni, E., & Colín, P. 2012, ApJ, 751, 77

Zamora-Avilés, M., & Vázquez-Semadeni, E. 2014, ApJ, 793, 84

Zamora-Avilés, M., Ballesteros-Paredes, J., & Hartmann, L. W. 2017, MNRAS, 472, 647

Zamora-Avilés, M., Vázquez-Semadeni, E., Körtgen, B., et al. 2018, MNRAS, 474, 4824

Zuckerman, B., & Evans, N. J., II 1974, ApJ, 192, L149

Zuckerman, B., & Palmer, P. 1974, ARA&A, 12, 279